UNIVERSITY OF AGDER

MAS 500 - Master's Thesis

A Self-Contained Electro-Hydraulic Cylinder: Modeling, Control Design, Simulation and Experimental Validation

by

Sølve Eggebø
Jan Størbu

May 25, 2018

Supervisor:

Dr. Damiano Padovani

Co-supervisor:

PhD Research Fellow Daniel Hagen

Department of Engineering Science

Faculty of Engineering and Science

Abstract

In the constant effort to improve the efficiency of hydraulic systems, the pressure drop over hydraulic valves has been one of the major obstacles. In the Self-Contained Electro-Hydraulic Cylinder, the directional valve and the hydraulic power unit have been replaced by a bi-directional axial piston pump and a Permanent Magnet Synchronous Motor. Actuation of the cylinder is performed by controlling the direction of rotation and the velocity of the motor.

Originally the purpose of this project was to: "Design a proper control algorithm for an existing novel self-contained electro-hydraulic cylinder, implement it on the main boom of a loader crane, and troubleshoot it". Due to a time delay in having the test bed ready for experiments, more effort was put into modelling and control design. The system is divided into three major parts: The hydraulic system, the electric drive and the external load in the form of a vertical boom with a payload. The main parts of the hydraulic system are the asymmetric cylinder, the fixed displacement axial pump and the load holding system. The load holding part consists of two pilot operated check valves, and a system for controlling the pilot pressure. The electric drive is divided into the inverter and the PMSM. The kinematics of the vertical boom was derived using classical static mechanics. In addition, a dynamic model is available, that was derived from a previous PhD research program, which was tested and compared to the static model. When all three models were combined into one, the overall simulation time was beyond what was considered useful, and it was decided to simplify the electric drive and use the static mechanic model.

Then the control design phase started, a linearised model of the system is derived and compared with the the high-fidelity Simulink model. A frequency response test is performed, both model based and on the test bed. Different control architectures are tested; such as P and PI controllers. A feedforward term is also implemented in the structure. The overall performance is then tested on several motion profiles.

Search words: Self-Contained Electro Hydraulic Cylinder, Fluid Power, Asymmetric Actuator, Axial Piston Pump, Passive Load Holding, Electric Drives, Permanent Magnet Synchronous Machine, Modelling, Control Design, Experiments.

Preface

This master's thesis in Mechatronics is carried out as the final project of the education at the University of Agder, the faculty of engineering and science. The novelty of this thesis lies in the research of passive load-holding using pilot operated check valves. This solution ensures no energy consumption during the load holding sequence.

This project originates from the SFI Offshore Mechatronics https://sfi.mechatronics.no, and the ongoing research in work package 1, Drives. The topic of the Self-Contained Electro Hydraulic cylinder is part of a research programme at UiA involving bachelor students, a Ph.D research programme and this master's thesis.

Our work started in the winter of 2018, and our supervisor Dr. Damiano Padovani encourage us to build a model of the hydraulic system using Simulink. As the work proceeded, the modelling expanded to include the electric drive. By coincident, the University of Agder was giving a Ph.D course for the modelling of electric drives that we were allowed to participate in, which provided valuable insights for this work.

At the end of 2017, the system design was performed by Søren Ketelsen at Aalborg University and parts were ordered by the University of Agder. The assembly was scheduled in February and March 2018. When the parts arrived, it turned out that the pump was defected, and the replacement pump did not arrive until the beginning of May. This incident did cost us valuable time for testing, as the deadline for handing in the thesis was closing in.

We would like to thank the bachelor students, Zygimantas Osinskas, Jørgen Olsen and Georgis Michael for spending a lot of time preparing the test bed for experimental work, by wiring the hardware and assembling the hydraulic equipment. They have also converted a SimulationX model of the crane into a SIMULINK model for us. A huge thank you must be addressed Ph.D research fellow Daniel Hagen for consulting our work, and spending a lot of time figuring out how to make the Bosch-Rexroth PLC cooperate with SIMULINK. Finally, we would like to thank our supervisor Dr. Daminao Padovani for guiding us through this project, and always keeping his door open for us.

Contents

Chapter 1

Introduction

The self-contained hydraulic cylinder (SCHC), is a concept merging hydraulics and electric drives and which has for instance replaced the conventional hydraulic actuator in the Airbus A380 [1, p.272]. The development of the technology is largely driven forward by the aeronautics; since the late 1970's, engineers have focused on solutions to replace the conventional centralized hydraulic power with Power-by-Wire-actuators (PBW) for flight control [2]. A PBW is powered and controlled by electrical wires instead of hydraulic power through pipelines.

Hydraulic equipment is widely used for actuation of heavy loads. It is found in a variety of different applications due to its high power to mass ratio, and its ability to control direction and speed with good accuracy [3, p. 297]. However, there are disadvantages, for instance the need of a centralized hydraulic power unit (HPU) to provide pressure and flow, pollution due to oil leakages, noise and reduced efficiency due to energy loss in orifices and valves.

One of the main disadvantages for hydraulic systems is the poor efficiency, most noticeably in systems with several actuators of substantial power demands. The poor efficiency can be improved by implementing a load sensing system, described in [4, p. 5:22]. However, even load sensing systems with several actuators working at different pressure levels will experience energy losses. The most efficient solution, according to [4], is adding more pumps and ideally one pump per actuator. This is the case for self-contained hydraulic cylinders.

The SCHC-concept includes advantages like high power to mass ratio and robustness. At the same time, it deals with disadvantages like low efficiency and pollution in a better way compared to conventional hydraulic power systems. Up until today, SCHC-systems have been most common in installations involving small loads, for instance actuation of control flaps on an aircraft. To expand the working field for the concept, for instance to installations including heavy loads in the oil and gas industry, especially the load holding function needs to be investigated more thoroughly. Unfortunately, research work on load holding-functions are more seldom to find. Due to that, this thesis focuses on a passive load holding function on a SCHC-model carried out by pilot operated check valves. The research questions for the thesis will be listed in section 1.2.

The majority of sources used in the following literature review concerns electro hydrostatic actuation-systems (EHA). The reason for this is the lack of literature studies specifically on SCHC. One should be aware that an EHA-system may differ from SCHC-architecture on at least two important points, the tank architecture and the load holding system. First, the EHA may have an open tank while the fluid systems are always sealed on the SCHC. Secondly, the passive load holding function is not common on EHA, while it is an important part of the SCHC-design. It can be mentioned that the SCHC comes in a variety of architectures, for instance depending on the use of symmetric or asymmetric actuators and the different load-holding solutions. Two

different architectures are presented in [5] and [6] with two pumps and with three pumps respectively.

1.1 The Self-Contained Hydraulic Cylinder

This section concerns the working principles and different combinations of pump and motor in a SCHC. The motor is discussed more thoroughly due to it's importance as the core of the SCHC. Then, there are few sentences about advantages and limitations of the concept and finally some examples of commercial providers of SCHC products.

1.1.1 The Design and Functioning of a Self-Contained Hydraulic Cylinder

A SCHC is, as the name says, completely self-contained; it has an electric servo motor with controller, an accumulator if an oil reservoir is needed, control elements such as flow control valves, a hydraulic actuator and one or several hydraulic pumps. Positioning of the actuator is controlled by a bidirectional electric driven pump, and the usual block chart for a self-contained cylinder is shown in figure 1.1. According to the command, the controller sends an electrical signal to the servo motor, which is the control element. The motor and the pump are rigidly tied together. The actuator piston moves as a response to the pressure difference, and a position sensor on the actuator provides feedback to the control system. Other components such as relief valves, check valves and pilot operated check valves in combination with a low pressure accumulator takes care of system pressure, avoidance of cavitation, load-holding system and flow balance in the case of asymmetric actuator [7, p. 126].

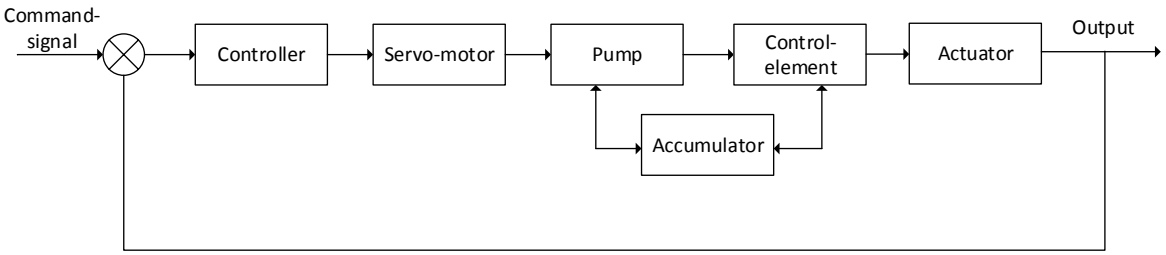

Figure 1.1: Block chart EHA.

Different combinations of pump and motor are used; variable displacement pump and fixed motor speed (VPFM), discussed in [7, p. 127], fixed displacement pump and variable motor speed (FPVM) and a combination of these concepts, a variable displacement pump and variable motor speed (VPVM). FPVM, which is analysed in [8], are simpler in structure than VPFM and have a better efficiency. The advantage of VPFM compared to FPWM is a faster response. The VPVM-system provides an opportunity to combine the advantages of the two simpler models; a dual-variable controller results in enhanced dynamic response and increased stiffness. A VPVM-concept with a swash-plate pump is further discussed in [9].

1.1.2 The Advantages and Limitations

SCHC have important competitive advantages compared with conventional hydraulics [7, p.127]. Electrical power are the only input to the SCHC-units. This way, weight is reduced and potential leakage problems are avoided when large quantities of hydraulic piping are replaced by electric wiring. Due to this, the SCHC is considered more reliable compared to systems with centralized HPU [10, p.3]. The systems are easier to replace when fault occurs, and therefore the downtime due to maintenance is reduced. While a conventional centralized HPU constantly consumes power for maintaining a certain pressure, the power usage for a SCHC is reduced since the motor stops and the passive load holding function activates when there is no cylinder motion.

All this said, the SCHC systems suffers from disadvantages such as reduced bandwidth and stiffness [3, p.127]. When a conventional hydraulic system is replaced with a SCHC, the response is determined by the characteristics of the motor and pump, which may not satisfy the system requirements. However, it is concluded in [7, p. 140] that the SCHC systems are reliable, efficient and maintainable hydraulic systems, seen from a power-by-wire view. The reduced need for maintenance in SCHC systems is described in [11, p.5]

1.1.3 The Electric Motor

The electric motor which drives the pump can be considered one of the most critical components regarding accuracy control of the actuator [7, p. 130]. Development within the electric motor industry accommodates requirements in the SCHC systems such as high power density motors and a compact design. Replacing the electromagnetic poles and mechanical commutators with permanent magnets and electronic commutation have resulted in high performance brush less machines. The absence of brushes has led to reduced length of the motor and higher stiffness of the rotor. The conduction of motor heat through the surface is increased as the windings are located in the stator and hence a higher electric loading is possible. These motors are classified on basis of the induced wave shape of their electro motive force, either trapezoidal or sinusoidal, and stator winding difference. Permanent Magnet Synchronous Motor (PMSM) or Permanent Magnet AC Motor have sinusoidal distributed stator windings and the induced wave shape is sinusoidal. Permanent Magnet Brushless DC Motors (BLDC) have concentrated windings and the induced wave shape is trapezoidal. The motors are controlled by a pulse width modulation (PWM) signal. In the literature, it is noted that there is an overwhelming use of BLDC in electro hydrostatic actuation systems [7, p. 130]. This is due to the fact that SCHC systems are most commonly used for low power installations.

1.1.4 The Load Holding Function

Literature and studies concerning load holding solutions for self-contained hydraulic cylinders are more seldom to find and appears to be an uncharted topic so far. A model using counter balance valves for the purpose of load holding is described in [12]. This solution guarantees load holding without energy consumption. Another method is to simply use the torque produced by the electro motor to hold the load, as described in [13, p.60].

1.1.5 Commercial Providers of SCHC Products

By searching the web for EHA products, several manufacturers claim to be able to deliver such products. Bosch-Rexroth, one of the major suppliers of fluid power equipment do has information on their web-site regarding EHA, but they do not currently have any products commercially available.

The Servi Group is a Norwegian based company that has launched a product called "Servi Hybrid Linear Drive", and according their customer support they currently have products ready off the shelf. The power rating is up to 60 kW and the maximum force is 3082 kN at 250 bar. They do not offer any products in the lower power rating area.

Koso M-Mac International is an US based company, claiming industrial deliveries to for instance the mining industry of EHA products. Ratings are up to 140 kN at 206 bar.

Parker Hannifin, a US based company, is claiming to be able to deliver what they call: the new compact electro-hydraulic actuator, but do not share any technical specification on their web site.

Advanced Actuators Ltd, a UK based company, seems to be one of the companies that have the longest experience with EHA's, as their history goes back to 1999 with these products. Their product ratings are: 25 - 800000 kgf, Stroke of 0 - 5000 mm, velocity of 2 - 500 mm/s and power up till 30 kW.
None of the above mentioned companies tell anything about load holding capabilities for their products. It is difficult to obtain technical information without purchasing a product because the competition is tough among suppliers. For this reason, they seem unwilling to share any information freely.

From the lack of scientific literature concerning high-power SCHC with passive load-holding, it is safe to assume that commercialized solutions with similar characteristics have a low market share. Countless applications, such as gripper arms for offshore pipe handling, hydraulic presses and scissor tables will benefit from high-power SCHC [14]. For that reason, this thesis is an in-depth study of a high-power full scale SCHC with passive load-holding.

1.2 The Research Topics

The novelty of this thesis lays in the research and experimental testing of the passive load holding functionality. An important aspect of the load holding function is to validate and investigate the performance of the pilot operated check valves. Aside from this, the other main topics include controlling the permanent magnet synchronous machine, design and experimental testing of control systems for high accuracy position control of the overall system. The test bed is designed to have a very flexible arm, for investigation of how to reduce oscillation in hydraulic systems. Due to this, oscillations and vibrations are amplified and thus give the "worst" working conditions for the SCHC. This gives an opportunity to design and test a robust control system.

1.2.1 The Implementation Plan

The first part of this research is to build a mathematical model of the test bed for the purpose of simulation. This work will be a preparation for the experimental work on the real test bed; different control algorithms should be investigated in addition to the general performance of the system. The next step will be to validate the mathematical model; the motor performance, flow characteristics of valves and system pressures should be compared with simulation results. The last part will concern the overall functioning of the test bed with the self-contained hydraulic cylinder concept implemented.

Chapter 2

System Description

This chapter concerns the different parts of the test bed including both the hydraulic and the mechanical system, as well as the electric drive and the control unit. First, the control system concerning digital and analogue signals and software/hardware are briefly described. Secondly, the hydraulic architecture is described by the different functions of the system, such as load holding and low pressure system. Then, the mechanical system are shown and described before several important parameters concerning the full system are listed. The control structures which will be tested during the project are then described and, finally, measurement of efficiency is done in the end of the chapter.

2.1 The Software and Hardware

This section contains two parts, one for the simulation and the modelling and one for the real test bed. Each part describes which tasks have used the software.

2.1.1 The Mathematical Model

Building a mathematical system-model for simulating the system has been one of the main tasks of the project. For this, MATLAB and Simulink version R2017b was used. The Simulink model implemented the mechanical system, hydraulics, PMSM, several control systems and functions for data logging. When building the model, it has been desired to avoid complex Simulink blocks and rather build up the PMSM, hydraulic- and mechanical system by use of equations and simple mathematical operators as much as possible. This is done to get a better understanding of the different components.

2.1.2 The Test Bed

The test bed is a hydraulic actuated mechanical system controlled by a PLC and Simulink. The system is shown in figure 2.1. The communication between PC and PLC is via Ethernet, and between PLC and IndraDrive via Sercos. Simulink is used for overall system control and data logging. For control, functions from MATLAB and Simulink are converted to structured text, IEC 61131-3, which is then converted to function blocks for programming of the PLC. MATLAB and Simulink are a good tool for data logging and plotting. IndraWorks is used for programming and compiling to the PLC. Both the PLC and the motor drive IndraDrive is powered with 24V of supply voltage to operate. The motor drive needs a 3-phase grid connection for the power electronic part.

Table 2.1: List of Software used by the test bed.

Task	Program	Version
Control system	MATLAB and Simulink	R2017b
Logging PLC data	MATLAB and Simulink	R2017b
Programming PLC	IndraWorks	ML 14V18 P2

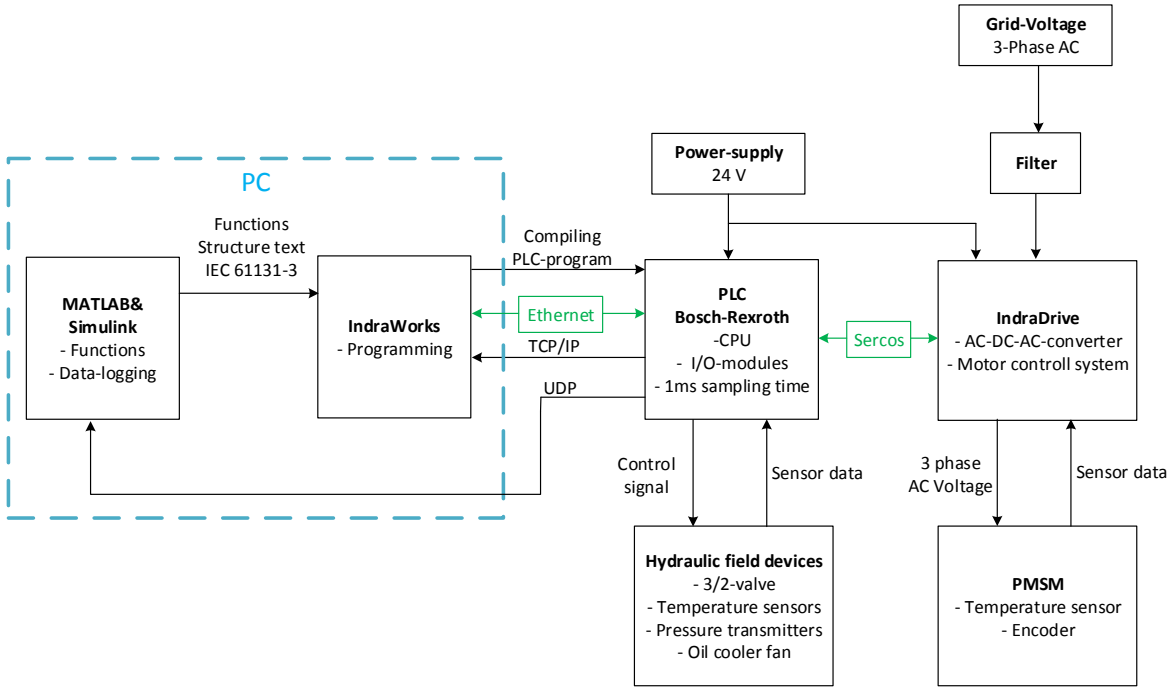

Figure 2.1: Signal flow in software and hardware.

The content of the CPU are shown in table 2.2 and specifications concerning the motor and the drive are shown in table 2.3

Table 2.2: Bosch-Rexroth PLC

Function	Item	Number
CPU	IndraControl XM22	1
AI-module	S20-AI-8,	3
AI/AO-module	S20-AI6-AO2-SSI2	1
DI-module	S20-DI-16/4	1
DO-module	S20-DO-16/3	1

Discretization

A PLC is a digital unit. Due to this, the control system must be a discretized; the continuous integrator should be replaced by a discrete and Zero Order Hold-blocks should be used for converting the reference- and feedback signals from continuous to discrete signals. When simulating the control system, Simulink provides three choices of discrete integration; Trapezoidal-, Forward Euler- and Backward Euler method. Testing the different methods showed that Forward and Backward Euler provided approximately equal results. The results from the Trapezoidal method showed more instability, hence, it was decided to use Forward Euler.

Sampling Time

The PLC cycle time has a lower limit at one millisecond. Even though Simulink can run at a higher frequency, this will not provide any extra information or higher resolution when logging data. The sampling time for Simulink is therefore chosen to be equal to the PLC cycle time of 1 ms.

2.2 Hydraulic system

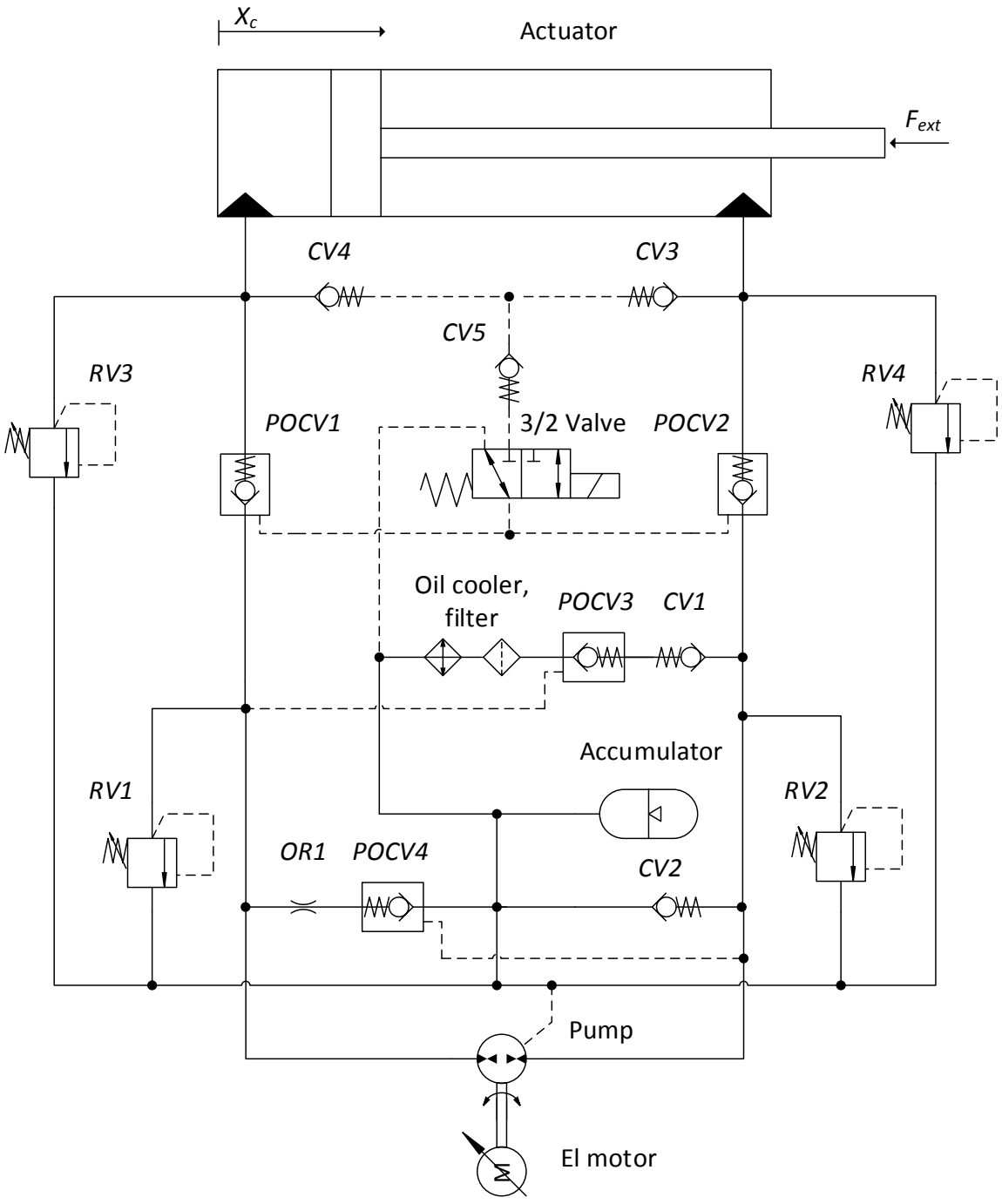

Figure 2.2: Hydraulic circuit diagram.

2.2.1 List of Hydraulic and Electric Components

Table 2.3: Hydraulic system components

Component	**Definition**	**Value**
Hydraulic cylinder	Bore diameter [mm]	65
	Rod diameter [mm]	35
	Bore side area [cm^2]	33.18
	Rod side area [cm^2]	23.56
	Cylinder ratio	0.71
	Length fully retracted [mm]	772
	Cylinder Stroke [mm]	500
	Maximum positive cylinder force [kN]	64
	Maximum negative cylinder force [kN]	-43.8
Pump	**Bosch Rexroth A10FZG010/10W**	
	Displacement [cm^3]	10.6
	Minimum pressure at low pressure side [Bar], abs	0.8
	Moment of inertia [kg/m^2]	0.0006
	Static pump speed for extension [RPM]	2817
	Static pump speed for retraction [RPM]	2001 (Pumping)
		2817 (Motoring)
	Maximum pump torque on shaft [Nm]	33.74
	Maximum angular acceleration [rad/s]	14000
Accumulator	**Bosch Rexroth HAB10-330-60/0G09G-2N111-CE**	
	Design	Diaphragm
	Nominal volume [l]	10
	Effective gas volume [l]	9.2
	Permissible max. flow [l/min]	60
	Permissible max operating pressure [Bar]	330
	Gas precharge pressure [Bar]<2	
	Ambient temperature range [^{o}C]	-15-65
	Hydraulic fluid temperature range [^{o}C]	-15-80(NBR)
	Charge gas	Nitrogen
Pilot operated check valves		
Load-holding system	**SunHydraulics CVEVXFN**	
(POCV1, POCV2)	Max operating pressure [Bar]	345
	Max Flow [L/min]	113
	Pilot ratio	1:3
	Cracking Pressure [Bar]	7
Low-pressure system	**SunHydraulics CKEBXCN**	
(POCV3, POCV4)	Max. operating pressure [Bar]	350
	Max. flow [l/min]	120
	Pilot ratio	3:1
	Cracking Pressure [Bar]	2

Continuous on next page

Component	Definition	Value
Check valves		
Low pressure system	**Hawe Hydraulic RK4**	
(CV1, CV2)	Cracking pressure [Bar]	0.1
	Nominal flow [l/min]	120
	Pressure drop nominal flow [Bar]	4
Pilot pressure load holding	**Hawe Hydraulics RB2**	
(CV3, CV4, CV5)	Cracking pressure [Bar]	0.1
	Nominal flow [l/min]	30
	Pressure drop nominal flow [Bar]	4
Temperature Transmitter	**Danfoss**	
	MBT 3560-0000-0050-10-110	
	084Z4030	
	Output signal [mA]	4-20
	Temperature range [^{o}C]	-50-200
Pressure Transmitters	**Bosch Rexroth HM20-21/10-C-K35**	
	Operating voltage [VDC]	16 . . . 36
	Output current [mA]	4-20
	Measuring range [Bar]	0-10
	Accuracy [%]	0. 5
	Rexroth HM20-21/250-C-K35	
	Operating voltage [VDC]	16 . . . 36
	Output current [mA]	4-20
	Measuring range [Bar]	0-250
	Accuracy [%]	0.5
Position Sensor	**Regal PS6310**	
	Input voltage, recommended [VDC]	10
	Operating speed [m/s]	2
	Output signal [%]	0..100
	Repeatability [mm]	$> \pm 0.013$
Pressure relief valve	**SunHydraulics**	
(RV1, RV2, RV3, RV4)	Pressure setting range [Bar]	35-210
	Crack Pressuer [Bar]	200
3/2 directional valve	**Argo Hytos**	
	SD1E-A3/H2S8M9	
	Max flow [l/min]	30
	Max operating pressure [Bar]	350
	Supply Voltage tolerance [%]	AC,DC:$\pm$15
	Max switching frequency [1/h]	15000
Oil filter	**Bosch Rexroth**	50LEN0100-H10XLA00-V2.2-M-R3
Cooler	**Bosch Rexroth**	KOL3N-30/R-F100-10-0/M
Continuous on next page		

Component	Definition	Value
Motor	**Bosch Rexroth**	
	MSK071E-0300-NN-S1-UG0-NNNN	
	Maximum speed [RPM]	4200
	Standstill torque [Nm]	23.0
	Standstill continuous current [A]RMS	12.5
	Maximum torque [Nm]	84
	Maximum current RMS [A]	56.3
	Torque constant at 20^{o}C [Nm/A]	2.05
	Voltage constant	1.207
	Number of pole pairs	4
	Winding inductance measured	
	between two winding ends [mH]	6.2
	Winding resistance measured	
	between two winding ends [Ω]	0.79
	Moment of inertia [kgm^2]	0.0029
	Optical encoder	128 increments
	Without holding brake	
Motor drive	**IndraDrive C HCS02**	
	DC bus continuous power [kW]	2.1 to 14
	Continuous mechanical power [kW]	1.5 to 11
	Overload capacity	2.5x
	Switching frequency [kHz]	4/8/12/16
	Output voltage [V](at DC-bus)	590

2.2.2 High Pressure System

The actuator transforms energy from hydraulic power to mechanical power. The fixed displacement pump, driven by the PMSM, transforms electrical power to hydraulic pressure and flow. The relief valves ensure that the pressure does not exceed the pressure-limits of the system and the orifice is included to prevent cavitation when the cylinder is retracting with negative load.

Consisting of:

- Actuator: Differential cylinder (DC)
- Pump: Fixed displacement pump
- Relief valves: RV(1, 2, 3 and 4)
- Orifice: OR1
- Electric motor: Permanent Magnet Synchronous Machine (PMSM)

2.2.3 Low-pressure system

Because of the asymmetric actuator, a fluid storage system is required. The accumulator implemented in the low pressure system functions as a sealed tank and the POCV3, POCV4, CV1 and CV2 ensure that the flow is directed appropriately and cavitation is prevented for all four quadrants of load and motion. The oil filter and cooler are necessary parts for maintaining this hydraulic system.

Consisting of:

- Accumulator
- Oil cooler and oil filter
- Pilot operated check valves: POCV(3 and 4)
- Check valves: CV(1 and 2)

2.2.4 Load Holding

To increase system efficiency when holding the load, it is suggested to use a system capable of holding the load with the PMSM shut off, called passive load holding. This is achieved by including two pilot operated check valves (POCV) and one electrically actuated 3/2 valve for controlling the pilot pressure. Bosch Rexroth has already announced a similar solution. However, such an approach has not been found in the literature. The components are shown in figure 2.3, the PMSM is excluded for visibility reasons.

Consisting of:

- Pilot operated check valves: POCV(1 and 2)
- Check valves: CV(3, 4 and 5)
- 3/2-way directional valve

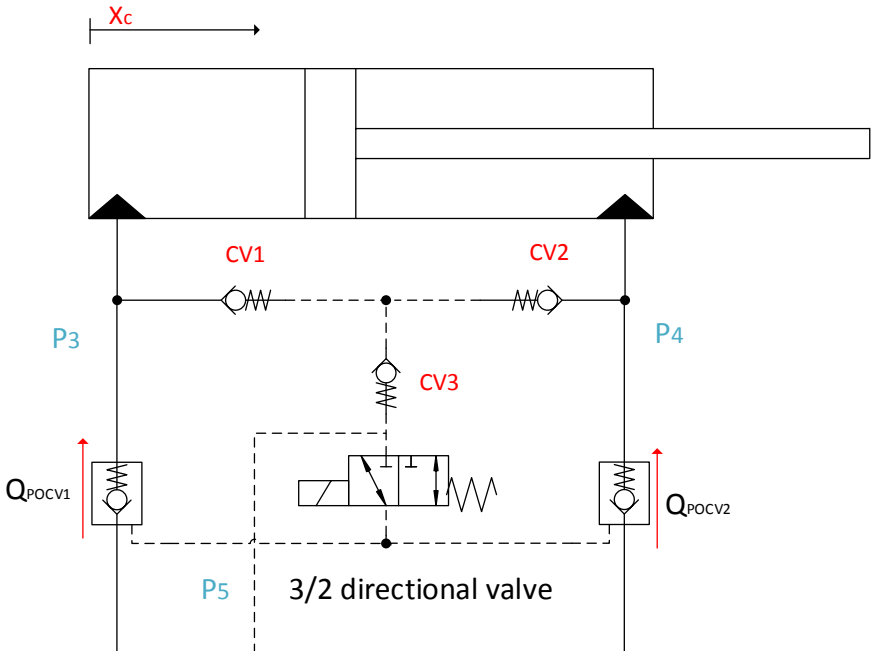

Figure 2.3: Load Holding Function

The command signal to the electrically actuated 3/2 directional valve (Enabler) is the same as the cylinder velocity command signal, used in the feed forward in the cylinder position controller. In addition, it is suggested to implement logic to ensure that cylinder position error is within a given hysteresis before the PMSM is shut off and the POCV's are closed.

When the enabler is not activated, the pilot pressure is equal to P5 which represent the low pressure of the system, and it is in the range of 0.8 to one bar. This ensures that the POCV's are closed in the reverse direction, but still acts as ordinary check valves in the normal direction. When the enabler is activated, the

pilot pressure is selected by the check valves, CV1-CV3 seen in figure 2.3, to be the highest pressure of P3 and P4. During the lowering sequence POCV1 must be opened by the pilot pressure. In this case P3 is the pilot pressure, and this pressure is not capable to fully open the POCV1 according to simulation results, but sufficient to lower the load. Figure 2.4 and 2.5 shows POCV 1 and 2 poppet displacement, for cylinder extraction and retraction, and shows whether or not the pilot pressure contributes to open the POCV's. There will be an undesired pressure drop over the POCV1, this seems unavoidable for this configuration, as no part of the system generates higher pressure than P3 when lowering the load.

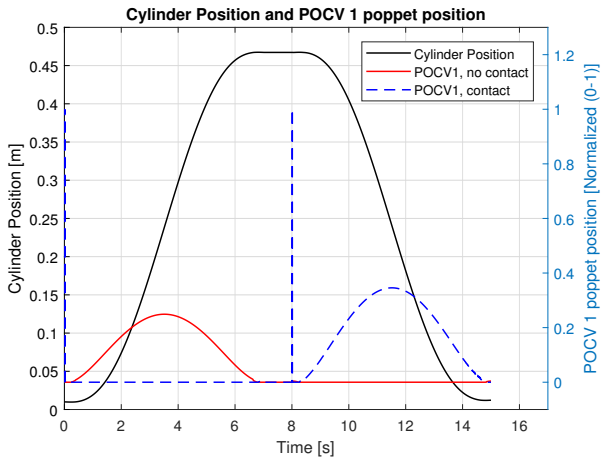

Figure 2.4: POCV1 Poppet Position

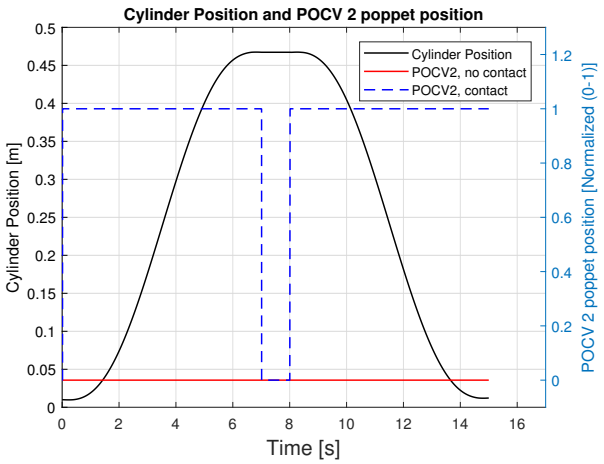

Figure 2.5: POCV2 Poppet Position

2.2.5 The System Design for Four Quadrant Working Function

The hydraulic system is designed for controlled motion in all four quadrants shown in figure 2.6; the pay load could either be aiding or resisting for both motion directions. It is designed such that flow is directed properly out of and into the low pressure system according to the motion direction of the cylinder. When designing such a system, any possibility for negative pressure, resulting in cavitation, must be considered carefully. For this specific reason, orifice OR1 in figure 2.7 is implemented.

For this study, experimental work is carried out for quadrant one and four, which mean that the force from the pay load always points in gravitational direction.

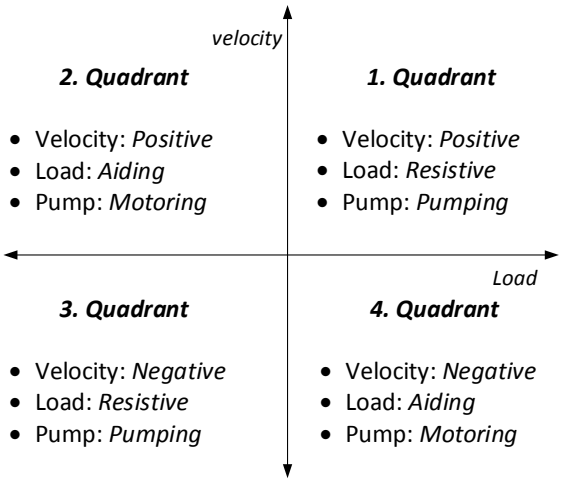

Figure 2.6: All four working quadrants

Working Principles for Quadrant One and Four

For quadrant one and four, the direction of the flow is shown in figure 2.7 and 2.8 respectively. Regarding quadrant one, the pay load is hoisted, the pump is working as a pump and the cylinder is extracting. The sum of cylinder volume on piston side and rod side are then increasing and fluid flows from the low pressure

into the high pressure system through CV2. Regarding quadrant four, the pay load is lowered, the pump is working as a motor and the cylinder is retracting. The sum of cylinder volume on piston side and rod side are decreasing and fluid flows from the high pressure system and into the low pressure system through CV1, POCV3, oil cooler and filter.

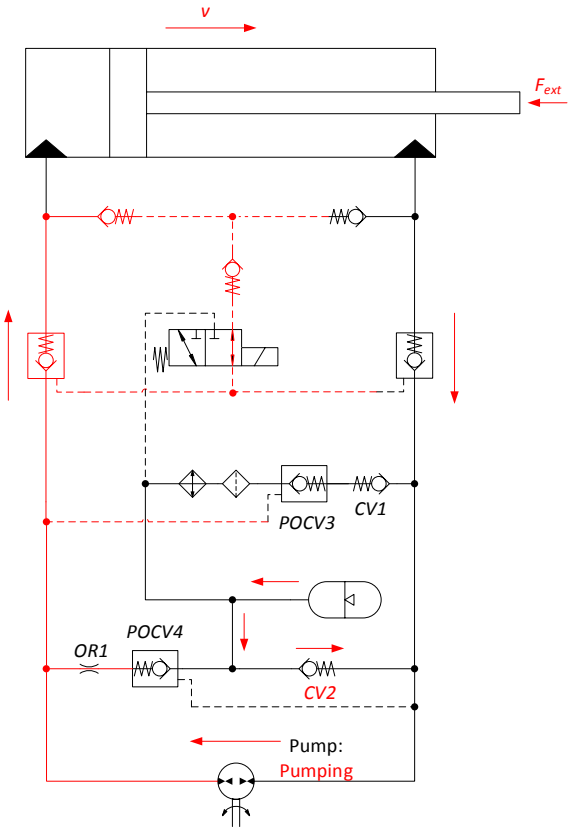

Figure 2.7: Quadrant 1: Flow and high pressure.

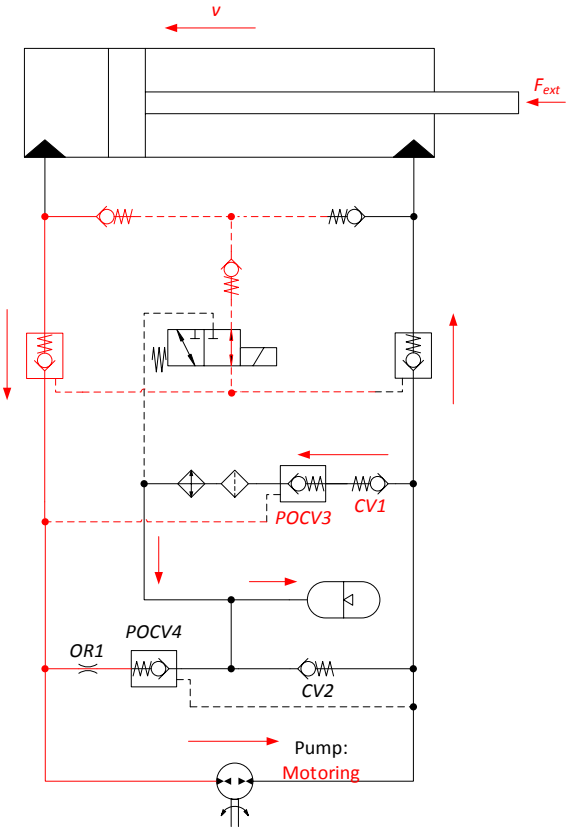

Figure 2.8: Quadrant 4: Flow and high pressure.

The high pressure side is marked with red in figure 2.7 and 2.8, and will always be the piston side of cylinder for quadrant one and four. There will be no flow through POCV 4 and OR 1 for these working modes. When modelling the hydraulic system, all four quadrants were tested and it was validated that for quadrant two and three there was flow through POCV 4 and OR1.

2.2.6 Low Pressure System and Pump House Pressure

The pump drain is directly connected to the low pressure system, figure 2.2, which means that the pump house will be exposed of the pressure in this system. The sealing between the chambers in the pump house could be damaged if the pressure exceeds an upper limit of 2 bar. The pressure builds up depending on the gas volume variations and the effective gas volume of the accumulator. This section shows that the actual accumulator satisfy the requirement regarding a low pressure build up.

The accumulator is the oil reservoir in the low pressure system and the fluid pressure is considered equal for the accumulator and the low pressure system; pressure drop between the accumulator and the rest of the low pressure system is neglected. Because it is a sealed system, pressure will build up when the accumulator is filled, shown in figure 2.1. The liquid and gas pressure are equal inside the accumulator.

The volume of fluid flowing in and out of the accumulator corresponds to the volume of the cylinder rod.

The pressure variations in the accumulator and low pressure system can be calculated given that the pre-loading pressure of the accumulator, effective gas volume of the accumulator, the poly-tropic coefficient and the variation of fluid volume is known. All these values are related as shown in equation 2.1. The volume variations are given by equation 2.2.

According to [4, p.4:24] pre load pressure, $p_{g,0}$, should be 90 % of minimum working pressure, p_{min}.

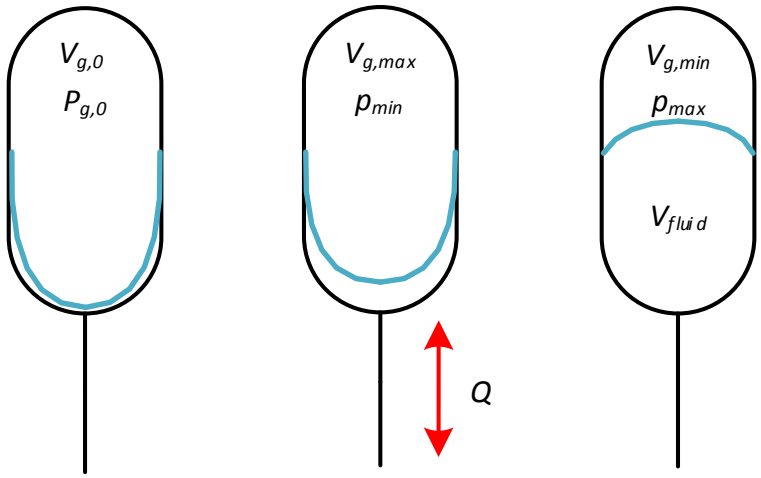

Figure 2.9: Three different accumulator modes, pre loaded, maximum and minimum gas volume.

$$p_{max} = \sqrt[\frac{1}{N_g}]{1 + \frac{\Delta V_g}{V_{g,min}}} \cdot p_{min} \tag{2.1}$$

$$\Delta V_g = V_{g,max} - V_{g,min} \tag{2.2}$$

The fluid volume variations in the accumulator, ΔV_{fluid}, which corresponds to the gas volume variation, ΔV_g, is given by equation 2.3.

$$\Delta V_{fluid} = \Delta V_g = \text{Volume of cylinder rod} \tag{2.3}$$

The length of the cylinder rod, l_{rod}, is equal to the cylinder stroke length given in table 2.3.

$$= l_{rod} \cdot \pi \cdot r_{rod}^2 \tag{2.4}$$

$$= 0.5\,\text{m} \cdot \pi \cdot \left(\frac{0.035\,\text{m}}{2}\right)^2 \tag{2.5}$$

$$= 0.000481\,\text{m}^3 = 0.481\,\text{l} \tag{2.6}$$

Minimum gas volume, $V_{g,min}$ is given by equation 2.7, $V_{g,max}$ from table 2.3.

$$V_{g,min} = V_{g,max} - \Delta V_g \tag{2.7}$$

$$= 9.2\,\text{l} - 0.481\,\text{l} \tag{2.8}$$

$$= 8.719\,\text{l} = 8.719 \cdot 10^{-3}\,\text{m}^3 \tag{2.9}$$

Maximum pressure in the accumulator is given by equation 2.10, p_{min} and N_g is given in table 2.5.

$$p_{max} = \sqrt[\frac{1}{N_g}]{1 + \frac{\Delta V_g}{V_{g,min}}} \cdot p_{min} \tag{2.10}$$

$$= \sqrt[\frac{1}{1.4}]{1 + \frac{0.481 \cdot 10^{-3}\ \mathrm{m}^3}{8.719 \cdot 10^{-3}\ \mathrm{m}^3}} \cdot 0.22 \cdot 10^5\ \mathrm{Pa} \tag{2.11}$$

$$= 23718\mathrm{Pa} \approx 0.24\,\mathrm{Bar} \tag{2.12}$$

The calculation shows that the maximum pressure of the accumulator is within the pressure limit by a satisfying margin, given a pre-loading pressure of 0.2 Bar. The pressure variations are small, shown in equation 2.15, which is beneficial when deriving a state space model of the plant; the pressure can then be considered a constant.

$$\Delta p_g = p_{max} - p_{min} \tag{2.13}$$

$$= 0.24\,\mathrm{Bar} - 0.22\,\mathrm{Bar} \tag{2.14}$$

$$= 0.02\,\mathrm{Bar} \tag{2.15}$$

Where:	p_{max}	Maximum accumulator pressure
	N_g	Poly-tropic coefficient
	V_g	Gas volume in accumulator
	V_{fluid}	Fluid volume in accumulator
	$V_{g,min}$	Minimum gas volume in accumulator when working
	$V_{g,max}$	Maximum gas volume
	p_{min}	Minimum pressure in accumulator
	p_g	Gas pressure in accumulator
	l_{rod}	Length of cylinder rod
	r_{rod}	Radius of cylinder rod

2.2.7 Pressure Relief Valve

To validate that the pressure relief valve performs as expected, and protects the system from pressures above 200 bar, the following simulation test was conducted: The motion profile for the cylinder was set up so the piston reaches end stop at 500 mm during extraction. The expected result is that pressure p1 should increase rapidly, and when reaching 200 bar, the pressure relief valve should open and allow flow, as shown in figure 2.10.

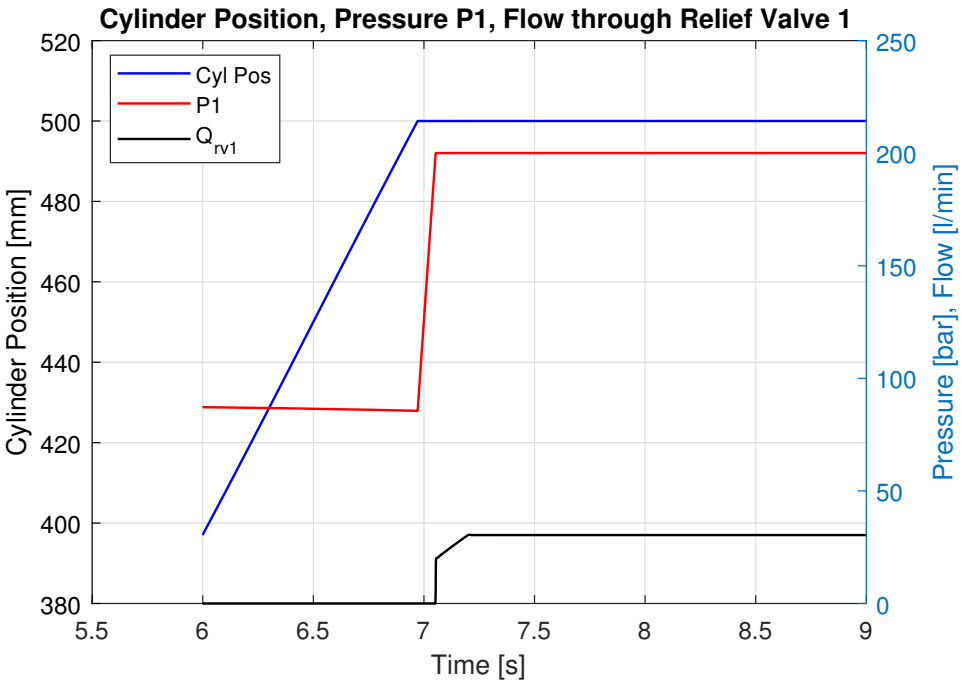

Figure 2.10: Flow through pressure relief valve 1.

2.3 Mechanical System

The mechanical system is located in the machine lab at UiA, Grimstad. It is designed to be very flexible for the purpose of emphasizing oscillating behaviour on hydraulic equipment. Due to this, the SCHC will be exposed to highly demanding working conditions.

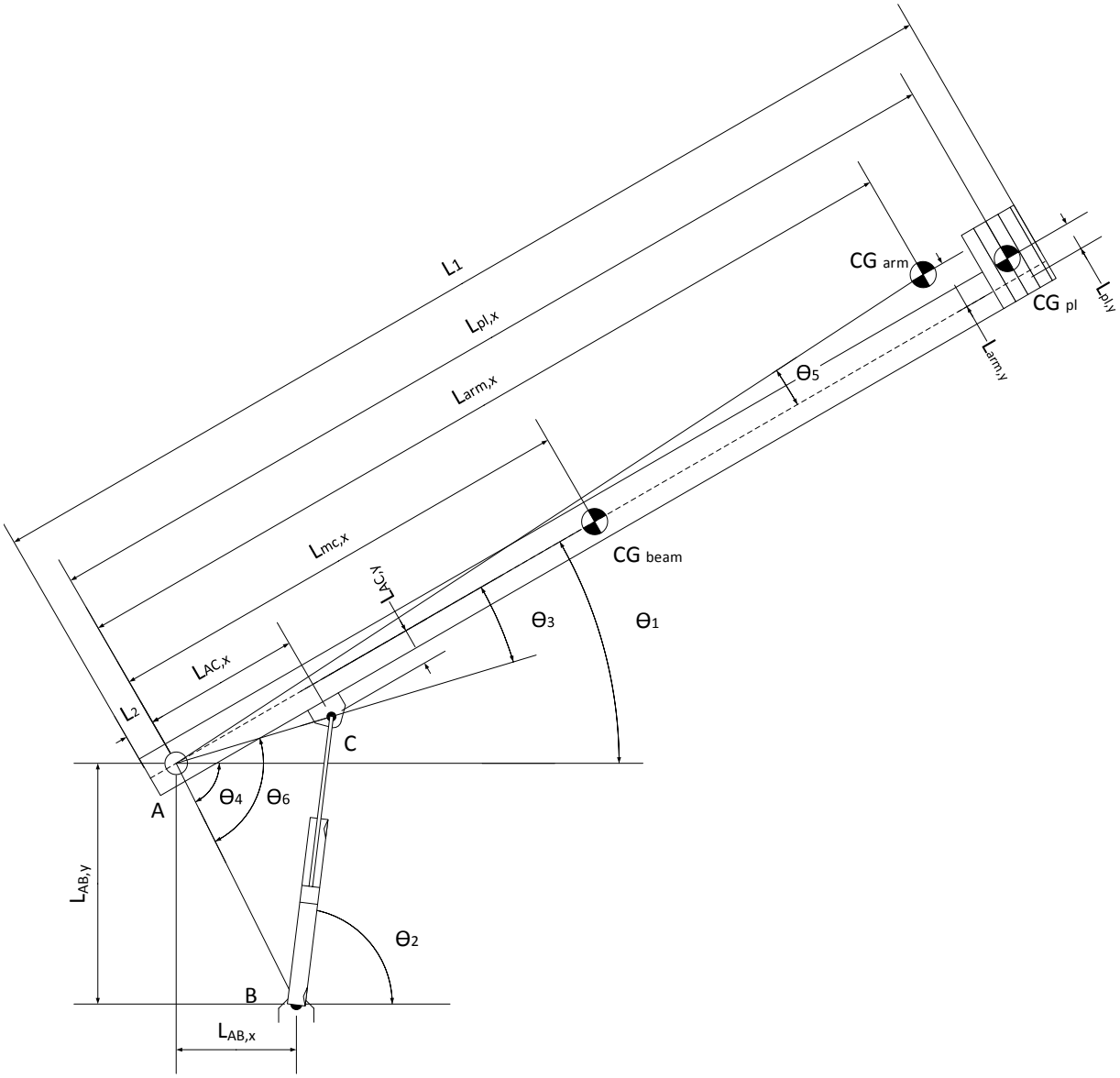

Figure 2.11: Figure of test bed

Table 2.4: Test bed specifications

Parameter	**Value**	**[Unit]**
Distance, bearing to right end of beam	$L_1 = 3680$	[mm]
Distance, bearing to left end of beam	$L_2 = 80$	[mm]
Distance x-direction, bearing to mass centre of payload	$L_{pl,x} = 3492.5$	[mm]
Distance y-direction, bearing to mass centre of payload	$L_{pl,y} = 80.8$	[mm]
Distance x-direction, bearing to mass centre of payload+beam	$L_{arm,x} = 3139$	[mm]
Distance y-direction, bearing to mass centre of payload+beam	$L_{arm,y} = 64$	[mm]
Distance x-direction, bearing to mass centre of beam	$L_{mc,x} = 1760$	[mm]
Distance x-direction, bearing to upper cylinder bracket	$L_{AC,x} = 550$	[mm]
Distance y-direction, bearing to upper cylinder bracket	$L_{AC,y} = 130$	[mm]
Distance x-direction, bearing to lower cylinder bracket	$L_{AB,x} = 420$	[mm]
Distance y-direction, bearing to lower cylinder bracket	$L_{AB,y} = 1055$	[mm]
Mass of pay load	m_{pl}= 320	[kg]
Mass of beam	m_{beam}= 82	[kg]

2.4 Parameter list

Table 2.5: Parameter list

Parameter	Definition [SI-unit]	Value	Hydr. unit
Flow through actuator			
p_s	Maximum system pressure [Pa]	200	Bar
$k_{l,i}$	Internal leakage [m^3/(sPa)]	0	l/(min· Bar)
$\dot{x}_{c,max}$	Maximum cylinder speed [m/s]	150	mm/s
Q_{max}	Maximum flow bore side actuator [m^3/s]	29.86	l/min
Low-pressure system			
p_{min}	Minimum working pressure accumulator [Pa]	0.22	Bar
N_g	Poly-tropic coefficient [-]	1.4	-
Transfer function, motor			
η	Damping factor [-]	0.45	-
ω_0	Natural frequency [rad/s]	31	Hz
Friction in cylinder			
τ_s	Time constant Stribeck friction [s/m]	0.02	s/m
f_c	Coulomb friction [N]	120	N
f_v	Viscous friction [Ns/m]	5000	Ns/m
Chamber volumes			
$Ch_{1...2}$	Volume of chamber 1 and 2 [m^3]	0.51	l
Ch_3	Volume of chamber 3 [m^3]	1.4	l
Ch_4	Volume of chamber 4 [m^3]	1.2	l
Ch_5	Volume of chamber 5 [m^3]	0.61	l
$Ch_{6...7}$	Volume of chamber 6 and 7 [m^3]	0.01	l
Initial pressures			
$p_{0,\text{ch1...2}}$	Initial pressure chamber 1...2 [Pa]	0.9	Bar
$p_{0,3}$	Initial pressure chamber 3 [Pa]	max 70	Bar
$p_{0,4...7}$	Initial pressure chamber 4...7 [Pa]	0.9	Bar
$p_{g,0}$	Pre-charge of accumulator [Pa]	0.2	Bar
Fluid parameters			
ρ_{oil}	Density of oil [kg/m^3]	870	kg/m^3
ν_{oil}	Kinematic viscosity [m^2/s]	$5.1 \cdot 10^{-5}$	m^2/s
μ_{oil}	Dynamic viscosity [kg/(ms)]$\rho_{oil} \cdot \nu_{oil}$	0.0444	kg/(ms)
β	Bulk Modulus [Pa]	15000	Bar
Control system			
$t_{r,c}$	Rise time current inner loop [s]	1	ms
$t_{r,s}$	Rise time velocity loop [s]	12	ms
Parameter IndraDrive			
$k_{p,cc}$	P-gain current loop [V/A]	2.5	V/A
$T_{i,cc}$	I-gain current loop [s]	4	ms
$k_{p,sc}$	P-gain speed loop [As/rad]	$\frac{10 \cdot 2\pi}{60}$	A·$(RPM)^{-1}$
$T_{i,sc}$	I-gain speed loop [s]	25	ms

2.5 Control Structures

Closed loop control systems compensate for disturbances by feeding back the measured output of the system, comparing it with the desired input, and generating an actuating signal that drives the plant [15, ch. 1]. An example of this is shown in figure 2.12,

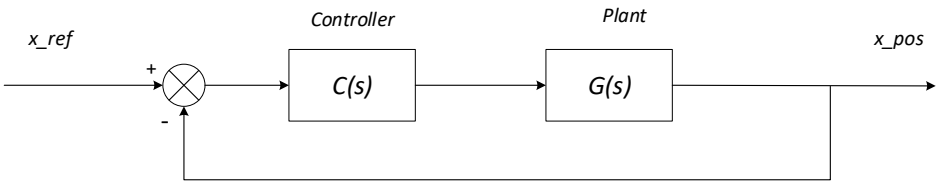

Figure 2.12: Block Diagram for Over all System

2.5.1 Different Control Algorithms

There are several control structures and a few will be described in this section.

PID-Controller

A popular controller in industry is the PID-controller, the structure is shown in figure 2.13,

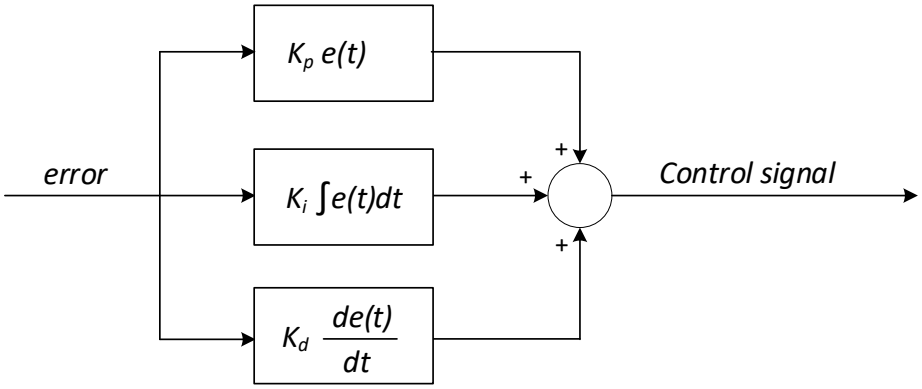

Figure 2.13: PID Controller

Depending on the plant to be controlled and what the compensated demands are, e.g. steady state accuracy, transient response or overshoot, then it is possible to select which part of the controller will be used, since it is possible to turn one or two parts off.

The simplest approach is to only use the Proportional gain, k_p. Then the control signal is proportional to the instantaneous value of the error. If the integral term is used in addition to the proportional gain, the controller is called a PI-controller. The controller sums up the error and multiplies it with the integral gain, k_i, generating the control signal. For large error the integral term may result in a control signal that is out of range of the actuator, then it is possible to implement an anti-windup function. The derivative part is seldom used in practice because when differentiating the error it can produce signal spikes due to noise in the signal. This effect can be reduced by filtering the signal, or limitation of the derivative gain. This is called a PD-controller.

Lead - Lag Compensator

Lead and Lag compensators have similarities with PD and PI controllers respectively [16]. A PD controller with limitation of derivative gain is almost the same as a Lead compensator. A PI controller with anti-windup is almost the same as a Lag controller. The combined Lead-Lag compensator is similar to the PID controller, the structure is shown in equation 2.16.

$$G_c(s) = K_{ess} \underbrace{\frac{1}{\alpha}\left(\frac{s+\frac{1}{T_2}}{s+\frac{1}{\alpha T_2}}\right)}_{G_{Lag}(\mathrm{s})} \underbrace{\frac{1}{\beta_l}\left(\frac{s+\frac{1}{T_1}}{s+\frac{1}{\beta T_1}}\right)}_{G_{Lead}(\mathrm{s})} \tag{2.16}$$

Where:	$K_{e_{ss}}$	Gain to meet steady state requirement
	T_1	Time constant
	T_2	Time constant
	$\alpha > 1$	
	$\beta_l < 1$	

Feed Forward

The system shown in figure 2.12 is possible to expand by including a feed forward term, as shown in figure 2.14. The reason for including this term is that known or measured disturbances can be accounted for before the feedback controller detect any error. Typically when a motion profile is to be followed, the velocity profile can be gained appropriate and feed forward into the controller structure.

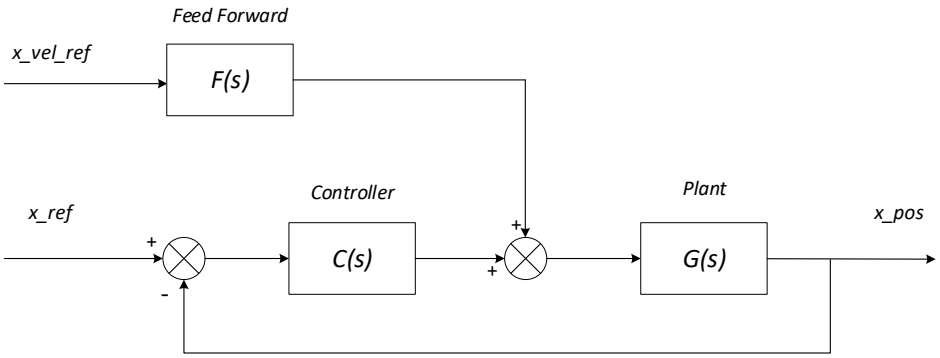

Figure 2.14: System Block Diagram with Feed Forward

The feed forward term can be constructed in several ways, and the best choice would have been to implement the inverse of the plant. However, this requires an exact model of the plant which is seldom achievable in practice. Nevertheless, a simplified solution will often improve performance over the use of a stand alone feedback controller.

2.6 Efficiency of the SCHC-System

Poor efficiency is a well-known problem for conventional hydraulics and one of the causes for this problem is the pressure loss in directional valves. One of the main reasons for developing the self-contained hydraulic cylinder is to remove this specific energy loss by controlling the direction and amount of flow with the pump velocity and rotational direction. For efficiency estimation, input- and output power is used. Power, P, is defined by equation 2.17 and 2.18 for translational and angular motion respectively.

$$P_{po} = F_{po} \cdot v_{po} \tag{2.17}$$

For rotational motion,

$$P_{po} = T_{po} \cdot \omega_{po} \tag{2.18}$$

The efficiency of the system, η_{sys}, is given by the output power divided by the input power shown in equation 2.19,

$$\eta_{sys} = \frac{P_{out}}{P_{in}} \tag{2.19}$$

Where:

P_{po}	Power
F_{po}	Force
v_{po}	Velocity
T_{po}	Torque
ω_{po}	Angular velocity
η_{sys}	System efficiency
P_{in}	Input power
P_{out}	Output power

The input and output power of the test bed hydraulic system depends on if it is hoisting or lowering the load. So, by use of the definition of power in equation 2.17 and 2.18, when the hydraulic system in hoisting, the product of the pump torque and angular speed is the input power and the product of the cylinder velocity and force is the output, and when lowering it is opposite. This is shown in equation 2.20 and 2.21.

The input power,

$$P_{in} = \begin{cases} T_p \cdot \omega_p, & \dot{x}_c > 0 \\ F_c \cdot \dot{x}_c, & \dot{x}_c < 0 \end{cases} \tag{2.20}$$

The output power,

$$P_{out} = \begin{cases} F_c \cdot \dot{x}_c, & \dot{x}_c > 0 \\ T_p \cdot \omega_p, & \dot{x}_c < 0 \end{cases} \tag{2.21}$$

Figure 2.15 shows the efficiency of the hydraulic system simulated when the cylinder is extracting. Maximum velocity of the motion profile is 0.11 m/s. The input and output power used for the test is given by equation 2.22 and 2.23 respectively. Unfortunately, when running the test for cylinder retraction, the results made no sense due to an efficiency above one. The result from test shows an efficiency value which could make sense, but one should be careful by interpreting the result as the retraction test failed.

$$P_{in} = \Delta p_{pump} \cdot D_p \cdot \omega_p \tag{2.22}$$
$$P_{out} = P_p \cdot A_p - P_r \cdot A_r - F_f \tag{2.23}$$

Where:	P_{in}	Input power
	P_{out}	Output power
	T_p	Torque of pump
	ω_p	Angular velocity of pump
	$\dot{x}_c$	Cylinder velocity
	F_c	Force from cylinder to load
	Δp_{pump}	Pressure drop over pump
	D_p	Displacement of the pump
	P_p	Pressure on piston side
	P_r	Pressure on rod side
	A_p	Area of piston side
	A_r	Area of rod side
	F_f	Friction forces

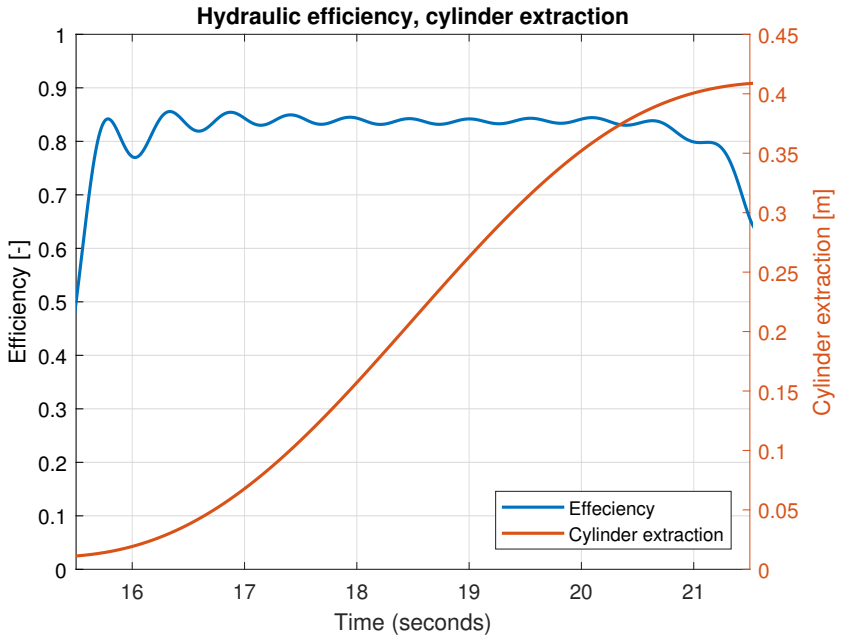

Figure 2.15: Efficiency retraction

The figure 2.15 shows an efficiency of 0.85 when the cylinder is extracting.

The power losses are due to friction forces in the cylinder and pressure drop over the valves. Pressure drops in hoses and lines are neglected in the model.

Chapter 3

Modelling the Hydraulics

The modelling approach described in this chapter has been successfully used in the past by several researchers, i.e. Hansen and Andersen in [4] and Zimmermann in [17].

The main purpose when analysing a hydraulic system is to investigate its functionality and performance [4, pp. 6:1-6]. More specifically, this concerns controllability of the system and investigation of parameters like flow, pressure and effect needed to meet the functionality-requirements. In general, the different suppliers of hydraulic equipment face tough competition where certain parameters are important such as price, weight, efficiency, controllability and safety. The use of modelling and simulation in the early design process gives several potential advantages: reducing time for development, reducing costs related to experimenting, better documentation and an opportunity to optimize existing systems.

3.1 Dynamic modelling the hydraulic system

The dynamic modelling of a hydraulic system is characterized by acceleration of mechanical parts and compression of fluid [4, p.6:6]. The model requires more accurate values of system damping and stiffness of oil compared to steady state evaluations, which is described in [4, p.6:2]. The differential equations in a dynamic model are time dependent. Due to this, initial values for pressures in the pressure nodes, volumes of accumulators, velocities and positions of mechanical degrees of freedom must be known at the start of the simulation. The dynamic modelling of a hydraulic system is described more in detail in [4, pp.6:6-6:15].

The next sections concern the differential equations for the components and pressure nodes in the hydraulic model.

3.1.1 Pilot Operated Check Valve

In general, check valves (CV) are flow control valves which allow almost free flow in one direction and prevent flow in the opposite directions. Hence, they operate as rectifiers and can be used for the purpose of load holding. A check valve can also be pilot operated (POCV), resulting in controlled flow in the opposite direction, governed by the pilot pressure contribution to the static equilibrium of the valve poppet. This type of valve is described in [4, pp. 3:11-12].

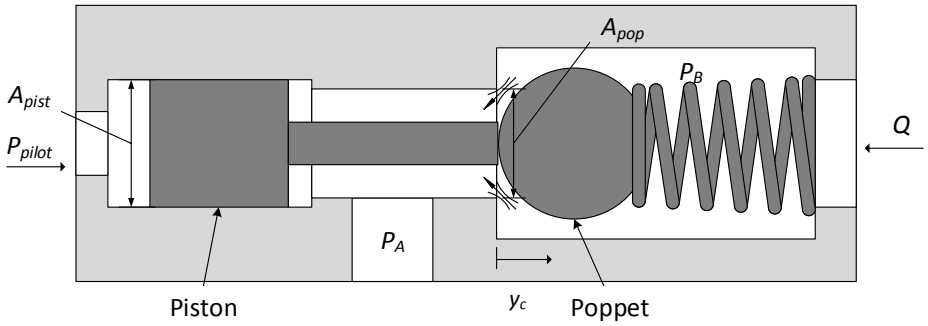

Figure 3.1: The pilot operated check valve.

Figure 3.1 describes the the pilot operated check valve where the inlet pressure, P_A, acts on both the piston and the poppet, the outlet pressure, P_B, acts on the poppet, and the pilot pressure P_{pilot} acts on the piston. P_A and P_B act on an equal area of the poppet, A_{pop}, and P_A and P_{pilot} act on an equal area of the piston, A_{pist}. When modelling the POCV, as figure 3.2 shows, logic must be used to select the appropriate equation for the static equilibrium of the poppet.

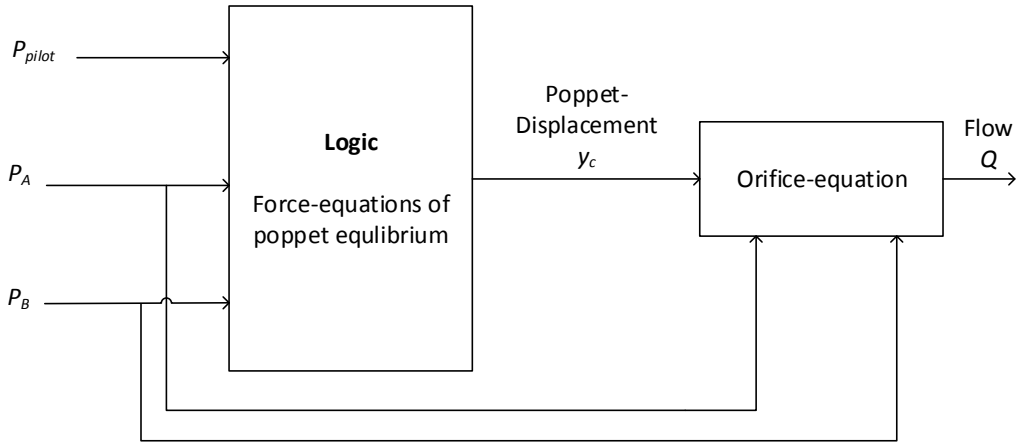

Figure 3.2: The different pressures contributing to poppet displacement which result in a flow when combined with pressure drop over the valve.

Force Equations for the Poppet Equilibrium

Two different force-equations, according to [17, p. 58], are applicable for the static equilibrium; either P_{pilot} greater than P_A resulting in the piston coming into contact with the poppet and applying a force on it, or P_A greater than P_{pilot} resulting in no contact between the poppet and piston and no contribution from P_{pilot}. The force-equations then follows:

$P_{pilot} > P_A \longrightarrow$ contact between piston and poppet, y_c is given from equation 3.2.

$$0 = (P_{pilot} - P_A)A_{pist} + (P_A - P_B)A_{pop} - F_{k,0} - ky_c \tag{3.1}$$

$$y_c = \frac{1}{k}\left[(P_{pilot} - P_A)A_{pist} + (P_A - P_B)A_{pop} - F_{k,0}\right] \tag{3.2}$$

$P_{pilot} < P_A \longrightarrow$ no contact between piston and poppet, y_c is given from equation 3.4

$$0 = (P_A - P_B)\, A_{pop} - F_{k,0} - k y_c \tag{3.3}$$

$$y_c = \frac{1}{k}\left[(P_A - P_B) A_{pop} - F_{k,0}\right] \tag{3.4}$$

Where:	P_{pilot}	Pilot pressure
	P_A	Inlet pressure
	P_B	Outlet pressure
	A_{pist}	Pressure area of piston
	A_{pop}	Pressure area of poppet
	$F_{k,0}$	Force from pre-tensioning of spring
	k	Spring stiffness
	y_c	Poppet displacement

Orifice Equation

The direction and amount of the flow is governed by the orifice-equation [18, p.328], shown in equation 3.5. The tangent hyperbolic prevents numerical problems when the flow shifts direction. The lift of the poppet, y_c, has a maximum lift at value one and a minimum lift at value zero.

$$Q_{or} = C_d A(y_c) \tanh(P_A - P_B)\sqrt{\frac{2}{\rho_{oil}}|P_A - P_B|}, \quad y_c = \begin{cases} 1, & y_c > 1 \\ y_c, & 0 \le y_c \le 1 \\ 0, & y_c < 0 \end{cases} \tag{3.5}$$

Where:	Q_{or}	Flow through orifice
	C_d	Discharge coefficient
	$A(y_c)$	Check valve discharge area as function of poppet displacement
	y_c	Poppet displacement
	P_A	Inlet pressure
	P_B	Outlet pressure
	ρ_{oil}	Density of fluid

3.1.2 Check Valve

For a check valve, described in [4, pp. 3:9-10] the equilibrium is governed by equation 3.3 and 3.4 and the flow is governed by the orifice-equation 3.5. The valve only permits flow in one direction. A flow occurs if the inlet pressure exceeds the sum of the crack pressure and the outlet pressure. Using a simplified approach for modelling the check valve, a linear flow coefficient, k_{cv}, is used, shown in equation 3.7. The force equilibrium is shown in equation 3.6.

$$(P_A - P_B)A_p - F_{k,0} = F_{CV} \tag{3.6}$$

then the flow through the orifice, Q_{CV}, becomes,

$$Q_{CV} = \begin{cases} k_{CV} F_{CV} & \text{if } F_{CV} => 0, \\ 0 & \text{if } F_{CV} < 0 \end{cases} \tag{3.7}$$

Where:	P_A	Inlet pressure
	P_B	Outlet pressure
	$F_{k,0}$	Force from pre-tensioning of the spring
	A_p	Pressure area of poppet
	F_{CV}	The sum of forces on the valve poppet
	Q_{CV}	Flow through the check valve
	k_{CV}	Linear flow coefficient

3.1.3 Pressure Relief Valve

The purpose of a pressure relief valve is to protect the system from excessive pressure [4, pp. 3:13-14]. The pretension of the spring, $F_{k,0RV}$, determines the crack pressure and flow occurs when the inlet pressure, P_A, exceeds the crack pressure. P_B commonly represents the tank pressure and thus it can be neglected. Besides this, the modelling is similar to the check valve. The force equilibrium is shown in equation 3.8 and flow through the valve is given by equation 3.7.

$$P_A A_p - F_{k,0RV} = F_{RV} \tag{3.8}$$

Equation 3.9 governs the flow through the orifice.

$$Q_{RV} = \begin{cases} k_{RV} F_{RV} & \text{if } F_{RV} => 0, \\ 0 & \text{if } F_{RV} < 0 \end{cases} \tag{3.9}$$

Where:	P_A	Inlet pressure
	$F_{k,0RV}$	Force from pre-tensioning of the spring relief valve
	A_p	Pressure area of poppet
	F_{RV}	The sum of forces on the valve poppet
	Q_{RV}	Flow through the relief valve
	k_{RV}	Linear flow coefficient

3.1.4 Accumulator

The accumulator is described in [4, pp.4:21-24].

When loading and unloading an accumulator, the gas becomes compressed or decompressed and undergoes a poly tropic process. Explained in short terms; when the gas is compressed and decompressed, the gas temperature changes with the pressure. If duration time is low, the temperature change happens very fast and the heat is not transferred to the surroundings. Then it is called an adiabatic process and the poly tropic constant is high. If the duration time is long, energy is transferred to the surroundings. Then it is called an isotherm process and the poly tropic value is lower. The relation between pressure, volume and the poly tropic constant is given by equation 3.10.

$$p_g \cdot V_g^{N_g} = \text{cst}, \;\; N_g = \begin{cases} 1.4 & t_p < 10 \text{ s} \\ 1.0 & t_p > 300 \text{ s} \end{cases} \tag{3.10}$$

Where:	p_g	Gas pressure
	V_g	Volume of gas
	N_g	Poly-tropic coefficient of work cycle
	t_p	Duration of working cycle for accumulator

The poly tropic constant can be given from the supplier, or chosen by a conservative design, using rough approximation from equation 3.10. Some systems are very sensitive to this value and it should be considered carefully. Nitrogen is the most common gas used in accumulators and its poly tropic constant is strongly dependent on temperature, pressure and duration of process. In addition, the value differs highly from loading-mode to unloading-mode.

When modelling the accumulator, the capacitance in the pressure build up equation are complex compared to the fixed volume pressure nodes. It is given in equation 3.11.

$$C_{H,accu} = \frac{V_{g,eff}}{N_g} \cdot \frac{p_{g,0}^{\left(\frac{1}{N_g}\right)}}{p_{lp}^{\left(\frac{N_g+1}{N_g}\right)}}, \tag{3.11}$$

Where:	$C_{H,accu}$	Capacitance of the accumulator low pressure system
	$V_{g,eff}$	Effective volume of accumulator
	N_g	Poly-tropic coefficient
	p_{min}	Pre-charge gas pressure of the accumulator
	p_{lp}	Pressure of the low pressure node

3.1.5 Cylinder

The cylinder converts hydraulic power to mechanical power governed by Newton's second law. This section concerns the friction, the force equation and the leakage.

Friction

The friction force is challenging to model due to the discontinuity around zero velocity and estimation of parameters. The discontinuity is solved by use of the tangent hyperbolic function and the parameters should be validated through experimental results. The governing equation for the friction force, F_f, is given by equation 3.12 from [17, p. 54].

$$F_f = \left(f_s e^{-\tau_s |\dot{x}_c|} + f_c\right) \tanh(\gamma \dot{x}_c) + f_v \dot{x}_c \tag{3.12}$$

Where:	F_f	Friction force
	f_s	Stribeck friction
	τ_s	Time-constant Stribeck friction
	$\dot{x}_c$	Velocity of cylinder
	f_c	Coulomb friction
	γ	Linear scaling factor
	f_v	Viscous friction

Cylinder force balance

The forces acting on the piston, which include the hydraulic pressure, friction forces and the external load, are shown in figure 3.3.

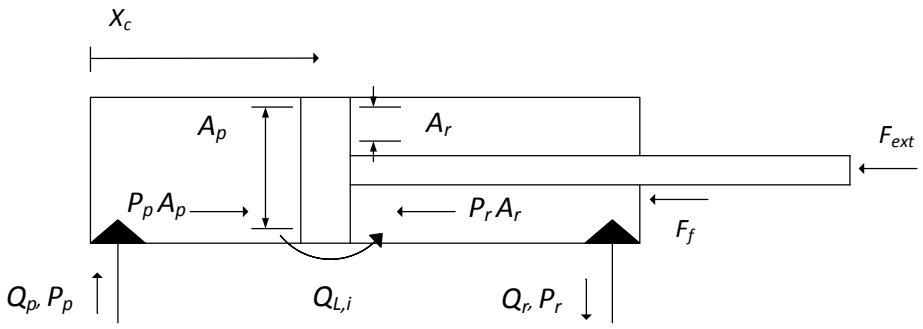

Figure 3.3: Cylinder model from [17].

Equation 3.13 from [17, p.53] governs the cylinder force balance. The equivalent mass, m_{eq}, is derived later in chapter 5.

$$m_{eq}\,\ddot{x}_c = p_p A_p - p_r A_r - F_f - F_{ext} \tag{3.13}$$

Where:	m_{eq}	Equivalent mass
	$\ddot{x}_c$	Acceleration of piston
	P_p	Pressure on piston side
	A_p	Pressure area on piston side
	P_r	Pressure on rod side
	A_r	Pressure area on rod side
	F_f	Friction force
	F_{ext}	External forces

Leakage

The internal leakage in the cylinder is modelled by the equation 3.14, [17, p. 56].

$$Q_{L,i} = k_{L,i}(P_p - P_r) \tag{3.14}$$

Where:	$Q_{L,i}$	Internal leakage
	$k_{L,i}$	Internal leakage coefficient
	P_p	Pressure on piston side
	P_r	Pressure on rod side

The external leakage are not taken into account in this study.

3.1.6 Pump

The pump converts mechanical power to hydraulic power in terms of flow and pressure. When implemented in a SCHC-architecture, two working modes, acting either as a pump or as a motor. When the load is resistive to the motion, it works as a pump governed by equation 3.15. When the load is aiding the motion, the pump is converted to a motor governed by equation 3.16.

$$Q_{p,p} = Q_{th} - Q_s, \quad \text{where } Q_{th} = V_p n_p \tag{3.15}$$

$$Q_{p,m} = Q_{th} + Q_s \tag{3.16}$$

Where:

$Q_{p,p}$	Pump flow in pump mode
$Q_{p,m}$	Pump flow in motor mode
Q_{th}	Theoretical pump flow
Q_s	Flow losses in pump
V_p	Fixed pump displacement
n_p	Rotational speed of pump

Volumetric and Mechanical Losses

Modelling the volumetric and mechanical losses in the pump are done by use of the method according to [17, pp. 49-51]. The method is valid because the working principles of the test pump are equal to the test bed pump used in this project; in both cases a piston pump is used. Briefly explained, the method takes basis in a set of real measurements on a specific pump size, then, a linear scaling factor, λ_{loss}, given in equation 3.17, is used to calculate equivalent losses for pumps where the displacement differs from the test pump.

$$\lambda_{loss} = \sqrt[3]{\frac{D_{scaled}}{D_{ref}}} \tag{3.17}$$

Mechanical and volumetric losses are given by equation 3.19 and 3.18

$$Q_{s,scaled} = \lambda_{loss}^2 Q_{s,ref} \tag{3.18}$$

$$M_{s,scaled} = \lambda_{loss}^3 M_{s,ref} \tag{3.19}$$

Where:

λ_{loss}	Linear scaling factor
D_{scaled}	Displacement of the scaled and modelled pump
D_{ref}	Displacement of the reference pump used for measurement of losses
n_{ref}	Reference rotational speed, pump
n_{scaled}	Scaled rotational speed, for the modelled pump
$M_{s,scaled}$	Scaled mechanical losses for the modelled pump
$M_{s,ref}$	Reference mechanical losses, pump
$Q_{s,scaled}$	Scaled flow losses for the modelled pump
$Q_{s,ref}$	Reference flow losses,pump

The Reference Pump Measurement

An experimental test was previously carried out for a 18 ccm/rev pump according to the ISO 4409 standard, which specifies methods for estimation of performance and efficiency of positive displacement pumps. The three variables measured are the speed of the pump, n_p, the pump pressure differential, Δp, and a swash plate angle, β. The measurements are obtained when the pump operates at a range of 1000-4500 RPM, the pressure differential ranges from 0-350 bar, and the swash plate angle varies from 0 to 100 %. It is assumed that the data are symmetric for negative displacements and pressure differentials. The data are then fitted to a polynomial surface using a least-square interpolation. A third order polynomial with three variables shown in equation 3.20 is used for describing the volumetric and torque losses. The flow and torque losses are given by equations 3.21 and 3.22 respectively. No measurements are done in this study; all data are acquired from [17]

$$f(x_1, x_2, x_3) = a_{111}x_1^3 + a_{112}x_1^2x_2 + a_{113}x_1^2x_3 + a_{11}x_1^2 + a_{122}x_1x_2^2 + a_{123}x_1x_2x_3 + a_{12}x_1x_2 + a_{133}x_1x_3^2 + a_{13}x_1x_3 + a_1x_1 + a_{222}x_2^3 + a_{223}x_2^2x_3 + a_{22}x_2^2 + a_{233}x_2x_3^2 + a_{23}x_2x_3a_2x_2 + a_{333}x_3^3 + a_{33}x_3^2 + a_3x_3 + a_0 \tag{3.20}$$

$$Q_s = f_Q(n_p, \Delta p_{pump}, \beta_s) \text{ (Flow losses).} \tag{3.21}$$

$$M_s = f_M(n_p, \Delta p_{pump}, \beta_s) \text{ (Torque losses).} \tag{3.22}$$

Where:	f	Curve fitting function of variable $x_1,\ x_2,$ and x_3
	$a_i\ (1 \leq i \leq 333)$	Coefficients of curve fitting polynomial
	$x_i\ (1 \leq i \leq 3)$	Curve fitting variables
	Q_s	Flow losses in pump
	f_Q	Function of flow losses in pump
	M_S	Mechanical losses in pump
	f_M	Function of mechanical losses in pump
	n_p	Rotational speed of pump
	Δp_{pump}	Pressure drop over pump
	β_s	Swash plate angle, normalised

The pump used in this project is a fixed displacement pump. Due to this, the swash plate is constantly set to 100 % in the simulation model. With only two variables, the mechanical and volumetric losses, the losses could have been described by a two-dimensional curve instead of the three-dimensional plane according to [17, p.50]. However, it is safe to assume that using the same method as [17], but replacing the variable swash plate angle with a constant value, will result in a good approximation of the pump losses.

3.1.7 Pressure Nodes of the System

When modelling a hydraulic system, the pressure nodes are fundamental. They represent demarcated volumes bounded by valves, pumps or actuators. The pressure rise of a pressure node is dependent on density, compressibility and stiffness of the hydraulic fluid. First, a brief explanation of these concepts is done before expressing the pressure build up equation.

Density

The density is a function of temperature, t, and pressure, p, [4, p.A:2] and is derived by taylor-expansion, shown in equation 3.23.

$$\rho_{oil} = \rho_{oil,0} + \frac{\partial \rho_{oil}}{\partial p}|_{p_0,t_0}(p - p_0) + \frac{\partial \rho_{oil}}{\partial t}|_{p_0,t_0}(t - t_0) \tag{3.23}$$

The last part of the expression represents a small value compared to the second part, hence, it can be neglected, resulting in the expression in equation 3.24.

$$\rho_{oil} = \rho_{oil,0}\left(1 + \frac{1}{\rho_{oil,0}}\frac{\partial \rho_{oil}}{\partial p}|_{p_0,t_0}(p - p_0)\right) \tag{3.24}$$

Where:	ρ_{oil}	Fluid density
	$\rho_{oil,0}$	Initial fluid density
	p	Fluid pressure
	p_0	Initial fluid pressure
	t	Fluid temperature
	t_0	Initial fluid temperature

Stiffness

Pressurizing a hydraulic fluid results in an increasing density due to compression of the fluid. The term "compressibility", K_f, is given by equation 3.25 from [4, p.A:8].

$$K_f = \frac{1}{\rho_{oil}}\frac{\partial \rho_{oil}}{\partial p} \tag{3.25}$$

The stiffness or the bulk modulus, β, is the reciprocal of the compressibility [4, p.A:8], expressed by equation 3.26.

$$\beta = \frac{1}{K_f} \tag{3.26}$$

Where:	K_f	Compressibility of fluid
	ρ_{oil}	Fluid density
	p	Fluid pressure
	β	Stiffness off fluid

Pressure Build Up Caused by Compression of Fluid

From the expression of density, equation 3.27, it can be shown that for fixed temperature there exist a relation between the pressure build, the stiffness of the fluid and the compression of fluid [4, p.A:8].

$$\rho_{oil} = \frac{m}{V} \tag{3.27}$$

Starting by differentiate the density with respect to volume, resulting in the partial derivative of density, equation 3.31.

$$\frac{\partial \rho_{oil}}{\partial V} = \frac{\partial}{\partial V}\left(\frac{m}{V}\right) \tag{3.28}$$

$$= m\frac{\partial}{\partial V}\left(\frac{1}{V}\right) \tag{3.29}$$

$$= -\frac{m}{V^2} \tag{3.30}$$

$$\partial \rho_{oil} = -\frac{m}{V^2}\partial V \tag{3.31}$$

Then substituting the expression for compressibility, equation 3.25, and partial derivative of density, equation 3.31, into the expression of stiffness 3.26 resulting in a stiffness expressed by change in in pressure and volume shown in equation 3.36.

$$\beta = \frac{1}{K_f} \tag{3.32}$$

$$= \frac{1}{\frac{1}{\rho_{oil}}\frac{\partial \rho_{oil}}{\partial p}} \tag{3.33}$$

$$= \frac{\rho_{oil}\,\partial p}{-\frac{m}{V^2}\partial V} \tag{3.34}$$

$$= -\frac{\frac{m}{V}\partial p}{\frac{m}{V \cdot V}\partial V} \tag{3.35}$$

$$\beta = -\frac{\partial p}{\frac{\partial V}{V}} \tag{3.36}$$

Rearranging equation 3.36 it is shown that for for fixed temperature, i.e. density is only depending on pressure, equation 3.23, there exists a relation between pressure build up, stiffness, the time derivative of expansion and the initial volume. From this relation, the pressure build up equation is defined in the next section.

$$\partial p = -\frac{\beta}{V}\partial V \tag{3.37}$$

Where:

	ρ_{oil}	Fluid density
	m	Mass of fluid
	V	Volume of fluid
	K_f	Compressibility of fluid
	p	Fluid pressure
	β	Stiffness off fluid

The Pressure Build Up Equation

According to [4, p: 6:6] for a pressure node containing compressible fluid, the pressure gradient is given by equation 3.38. This expression shows the pressure is dependent on the time derivative of expansion from equation 3.37 and the net-flow, Q, into the volume.

$$\dot{p} = \frac{\beta}{V_0}\left(Q - \dot{V}\right) \tag{3.38}$$

Where:	$\dot{p}$	Pressure gradient
	β	Stiffness of the hydraulic fluid
	Q	Net flow into the volume
	$\dot{V}$	Time derivative of expansion
	V_0	Initial volume of pressure node

The flow balance into the volume is positive if flow enters the volume and the time derivative of expansion is positive if the volume is expanding. The effective stiffness in reality, is highly dependent on dissolved air in the system, flexibility in hosings and tubings in addition to the fluid stiffness, β. To be solved, this first order differential equation requires initial values for the pressure and volume. The seven different pressure nodes of the actual system are shown in figure 3.4 which are defined by boundaries and expressed mathematically in table 3.1.

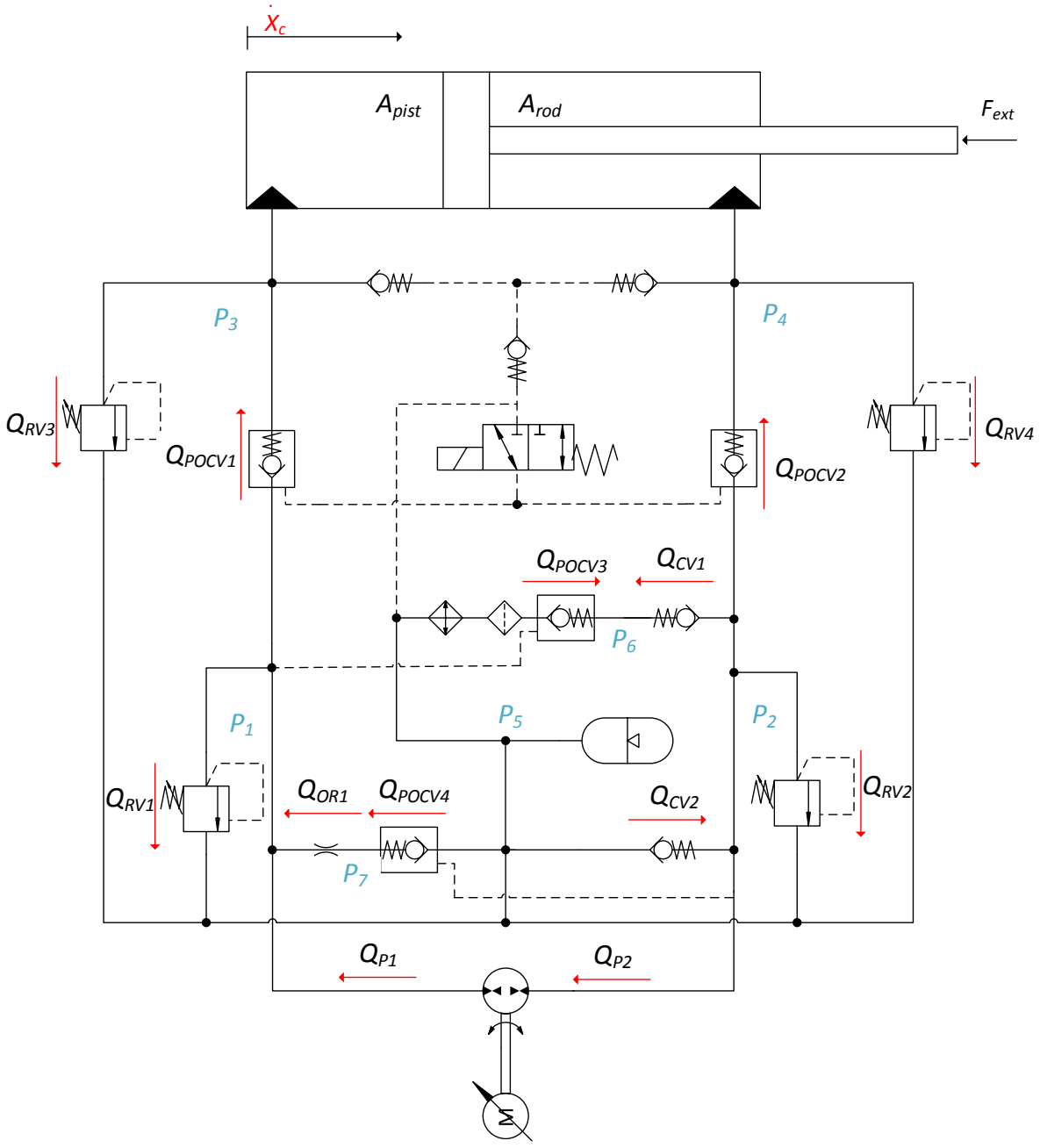

Figure 3.4: P1-P7, typed in blue, represent the pressure nodes.

The Pressure Nodes

Table 3.1: Pressure nodes according to figure 3.4

No.	Bound.	Pressure build-up equation
1	Pump RV1 POCV1 OR1	$\dot{P}_1 = \frac{\beta}{V_1}\left(Q_{P1} + Q_{OR1} - Q_{RV1} - Q_{POCV1}\right)$
2	Pump CV1 CV2 POCV2 RV2	$\dot{P}_2 = \frac{\beta}{V_2}\left(-Q_{P2} + Q_{CV2} - Q_{CV1} - Q_{POCV2} - Q_{RV2}\right)$
3	POCV1 RV3 Piston	$\dot{P}_3 = \frac{\beta}{V_3(x_c)}\left(Q_{POCV1} - Q_{RV3} - \dot{x}_c A_{pist}\right)$
4	Piston POCV2 RV4	$\dot{P}_4 = \frac{\beta}{V_4(L_{stroke}-x_c)}\left(Q_{POCV2} - Q_{RV4} + \dot{x}_c A_{rod}\right)$
5	CV2 POCV(3,4) RV(1,2,3,4)	$\dot{P}_5 = \left(\frac{V_5}{\beta} + \frac{V_{g,eff}}{N_g} \cdot \frac{\left(\frac{1}{N_g}\right)}{\left(\frac{N_g+1}{N_g}\right)} \frac{p_{g,0}}{p_5}\right)^{-1} \left(Q_{RV(1,2,3,4)} - Q_{POCV4} - Q_{POCV3} - Q_{CV2}\right)$
6	CV1 POCV3	$\dot{P}_6 = \frac{\beta}{V_6}\left(Q_{POCV3} + Q_{CV1}\right)$
7	POCV4 OR1	$\dot{P}_7 = \frac{\beta}{V_7}\left(Q_{POCV4} - Q_{OR1}\right)$

Where:	P_i $(1 \leq i \leq 7)$	Pressures in pressure node 1-7
	V_i $(1 \leq i \leq 2$ and $5 \leq i \leq 7)$	Volumes of pressure node 1, 2, 5, 6 and 7
	β	Bulk modulus
	$V_{g,eff}$	Effective accumulator gas volume
	$p_{g,0}$	Pre load pressure in accumulator
	l_{stroke}	Stroke length of cylinder x_c for pressure node 3 and 4
	$\dot{x}_c$	Velocity of cylinder
	N_g	Poly-tropic coefficient accumulator
	Q_i $(1 \leq i \leq 2)$	Pump flow into pressure node 1 and 2
	Q_{RVi} $(1 \leq i \leq 4)$	Flow through relief valves 1,2,3 and 4
	Q_{POCVi} $(1 \leq i \leq 4)$	Flow through pilot operated check valve 1,2,3 and 4
	Q_{CVi} $(1 \leq i \leq 2)$	Flow through check valve 1 and 2

3.1.8 Pressure Drops in Lines and Hoses

The lines and hoses are of short in length and have a large dimension. Due to this, the pressure drop is neglected.

Chapter 4

Modelling the Electric Drive

For the purpose of future study of permanent magnet synchronous motors used in self-contained hydraulic cylinders, this chapter creates a foundation of the basic terms and working principle of an electric motor as well as the principles of field oriented control of PMSM.

Electric machines have been used for over a century to drive mechanical loads by converting electric energy [19, Ch.1]. Up until now the easiest machines to control have been Direct Current (DC) machines, both position and velocity are easily controllable. The down side is high maintenance cost because of electric commutation by brushes.

The Alternating Current (AC) machines are divided into different groups, single phase and three phase, synchronous and asynchronous, and a variety of versions within the groups. Some of these machines uses brushes, but they are not considered in this thesis. In recent years, the power electronics have grown to be powerful and fast enough to be able to control position and velocity with a high degree of accuracy. These machines benefit from low maintenance cost due to lack of brushes, the commutation is provided by the sinusoidal time varying currents.

The machine under consideration in this thesis is a three phase permanent magnet synchronous machine (PMSM). Naming convention is not consistent in literature. Typically names for the same machine can be; Servo Motor, Permanent Magnet AC Machine (PMAC).

For controlling the machine a Power Processing Unit (PPU) is required, additional names used for this part is inverter or drive. A block diagram of an Electric Drive is shown in figure 4.1.

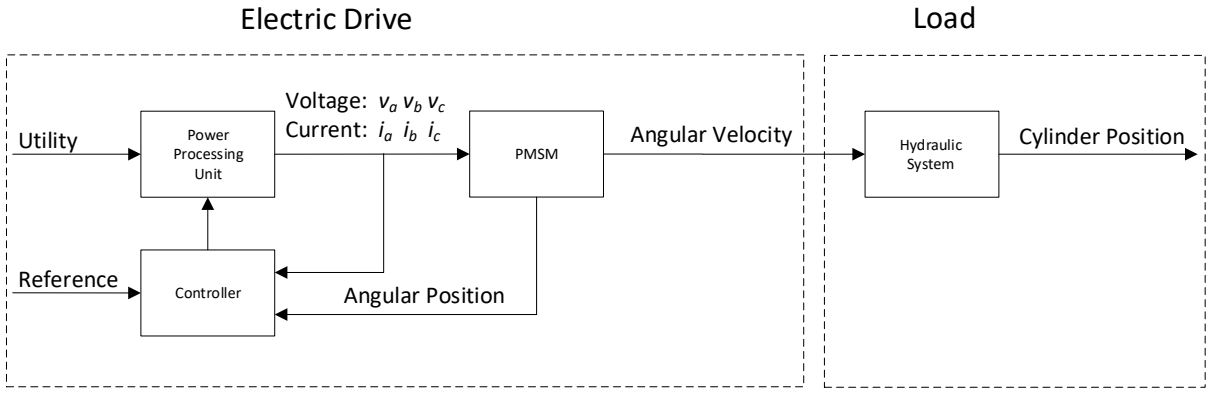

Figure 4.1: Block Diagram for Closed Loop Operation of PMSM

4.1 Basic Concept of Magnetic Circuits

To understand how electric energy is converted to mechanical energy through the rotating motor, it is necessary to be familiar with some basic concepts associated with magnetic circuits [19, Ch.5].

4.1.1 Magnetic Field

A magnetic field is produced when a current is flowing through a conductor. The direction of the magnetic field is dependant on the direction of the current. This is visualized in figure 4.2 showing the magnetic field surrounding a conductor. To the right, the current is coming out of the paper and the field has a counter clock wise direction. To the left, the current is in directed down into the paper and the field direction is clock wise.

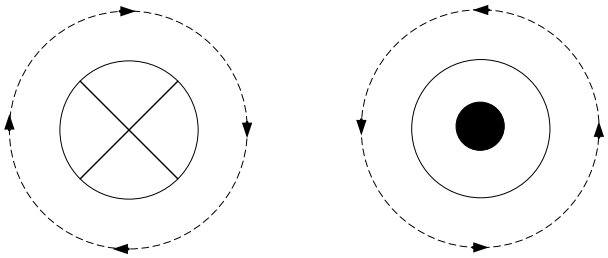

Figure 4.2: Magnetic field due to current flow in a conductor.

Where: $\times$ means current flow into paper
$\bullet$ means current flow up from paper

Ampere's Law

Several current carrying conductors are producing a magnetic field intensity according to Ampere's Law, given in equation 4.1

$$\oint H\,dl = \sum i \tag{4.1}$$

Where: $\oint$ Closed line integral
H Magnetic field intensity
$\sum i$ Total current inside the line integral
dl Differential length along the closed path

Ampere's Law can be used for calculation of the field intensity produced by the current in a given coil, or more specifically in this thesis, a stator winding in a given motor. This is shown in equation 4.2.

$$H_m = \frac{Ni}{l_m} \tag{4.2}$$

Where:	H_m	Magnetic field intensity
	N	Number of turns
	i	Current
	l_m	Mean path length surrounding currents

The term in the nominator of equation 4.2, Ni is often referred to as MagnetoMotive Force (mmf), and this produces the magnetic field.

Flux Density $\mathcal{B}$ and Flux ϕ

When a magnetic field is acting on a material, the flux density is dependant on the the magnetic permeability of this material, and for free space the following expression yields.

$$B = \mu_0 H \tag{4.3}$$

Where:	B	Flux density
	H	Magnetic field intensity
	μ_0	Permeability of air or free space

The permeability of free space is $\mu_0 = 4\pi \times 10^{-7} \left[\frac{henries}{m}\right]$

Ferromagnetic materials have high permeability and require a small current for a given number of windings to produce the desired flux density. The permeability of a material is often given in terms of a relation to the permeability of free space, shown in equation 4.4.

$$\mu_r = \frac{\mu_m}{\mu_0} \tag{4.4}$$

Where:	μ_r	Relation of permeability of the ferromagnetic material and free space
	μ_m	Permeability of the ferromagnetic material
	μ_0	Permeability of air or free space

For a given cross section, and assuming uniform flux density, the flux is determined by equation 4.5:

$$\phi_m = B_m A_m \tag{4.5}$$

Where:	ϕ_m	Magnetic flux
	B_m	Magnetic flux density
	A_m	Area of the cross section of the material

By combining equation 4.2, 4.3, 4.4 and 4.5 the following expression for the flux is given:

$$\phi_m = \frac{Ni}{\frac{l_m}{\mu_m A_m}} \tag{4.6}$$

Where:
- ϕ_m Magnetic flux
- N Number of turns
- i Current
- l_m Mean path length surrounding the currents
- A_m Area of the cross section of the material
- μ_m Permeability of the ferromagnetic material

The denominator in equation 4.6 is often referred to as Reluctance, $\Re$, and has the unit $\left[\frac{A}{Wb}\right]$. Equation 4.6 shows the relation between flux, mmf and $\Re$, and is analogous to Ohm's law, I=U/R.

Flux Linkage

The flux linkage is determined when all windings in a coil are linked by the same flux, and is shown in equation 4.7:

$$\lambda = N\phi \tag{4.7}$$

Where:
- λ Flux linkage
- N Number of turns
- ϕ Flux

Inductance

The flux linkage is related to the current by the parameter defined as the inductance, shown in equation 4.8:

$$\lambda_m = L_m i \tag{4.8}$$

Where:
- λ_m Flux linkage
- L_m Inductance
- i Current

By combining equation: 4.2, 4.3, 4.5 and 4.7 the following expression for inductance is derived, shown in equation 4.9:

$$L_m = \frac{N^2}{\Re_m} \tag{4.9}$$

Where: L_m Inductance
N Number of turns
$\Re_m$ Magnetic reluctance

Faraday's Law

Faraday's Law states that there is an induced voltage in a coil if there is a time-rate of change of the flux linkage. This is formulated in equation 4.10:

$$e(t) = \frac{d}{dt}\lambda(t) = N\frac{d}{dt}\phi(t) = L\frac{d}{dt}i(t) \tag{4.10}$$

Where: $e(t)$ Induced voltage
λ Flux linkage
N Number of turns
L Inductance
$i(t)$ Time changing current

From section 4.1 it is shown that the time varying current governs the following parameters: Magnetic field H, Flux Density B, Flux ϕ, Flux Linkage λ and the induced voltage $e(t)$ in a coil or in a stator windings.

Lentz's Law

To determine the polarity of the induced voltage Lentz's Law can be applied. It states that if a current is flowing due to an increase of flux linkage, the direction of this current will try to resist the flux change.

4.1.2 Energy Conversion

There are two fundamental concepts that govern the operation of electric machines to convert electric energy to mechanical energy and vice versa [19, Ch.6].

1. If a current carrying conductor is placed in a externally established magnetic field, a force f_{em} is produced.
2. If a conductor is moving in a magnetic field, there will be an induced emf.

In the first concept, the force is f_{em} which represents the actual force that rotates any electric motor. The direction of the force is given by the cross product shown in equation 4.11, and the magnitude is determined by the length of the vector f_{em}.

$$f_{em} = (i \times B) \cdot l \tag{4.11}$$

Where: f_{em} Force
i Current
B Flux density
l Length of conductor exposed to the flux density

In figure 4.3 it is shown that the flux lines add up on the right side of the conductor where the arrows point in the same direction, whereas it is the opposite on the left side. This gives the direction of the electro magnetic force f_{em}.

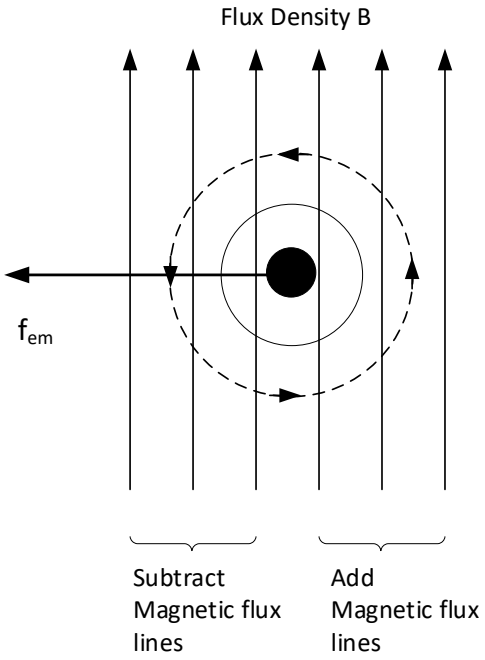

Figure 4.3: A current carrying conductor in a B field

The second concept has a moving conductor which causes an induced emf. The direction of the induced emf is determined by the cross product given in equation 4.12, and the magnitude is determined by the length of the vector e_{emf}.

$$e_{emf} = (u_{cond} \times B) \cdot l \tag{4.12}$$

Where:	e_{emf}	Induced emf
	u_{cond}	Velocity
	B	Flux density
	l	Length of conductor exposed to the flux density

In figure 4.4 it is shown how a conductor is moving in a magnetic field B with a velocity u_{cond}, and produces an induced emf. The polarity is indicated by ± signs.

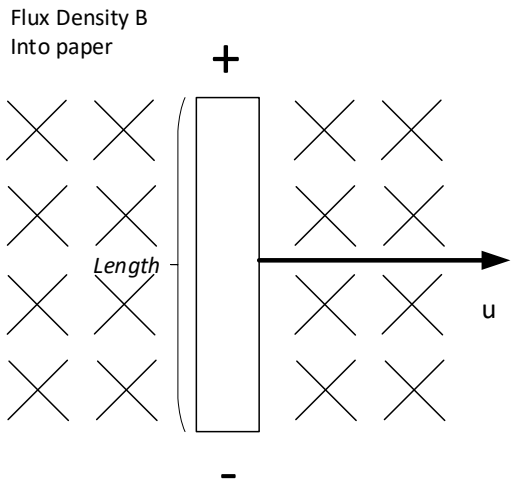

Figure 4.4: Moving conductor in a B field

4.1.3 PMSM Principle of Operation

There are mainly two types of three phase motors: Induction motors, the work horse of the industry, and the Permanent Magnet Synchronous Motors (PMSM), used for servo application. The main difference in these machines is the rotor construction, while the stators are similar [19, Ch. 9]. Only PMSM is considered in this thesis.

Stator Windings

In the stator, each of the three phase windings produce a sinusoidally field distribution. This is possible by arranging the windings in a sinusoidally pattern, visualized in figure 4.5. For visibility reasons only phase a is shown. Large circles represent high winding density, and small circles low. The • indicates that the current is coming and the × indicates that the current is leaving. The magnetic field is directed along the a-axis, as described in section 4.1. For the ease of drawing and for better understanding, a two pole machine is investigated, but the derivation is expandable for multi pole machines.

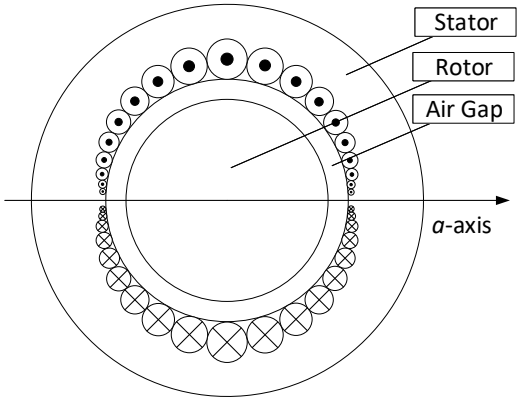

Figure 4.5: Sinusoidally distributed stator windings

The main goal is to obtain the air gap field distribution caused by the winding current. As shown in section 4.1, is it the current that is controlling: mmf, flux density and the magnetic field intensity. It is assumed that the magnetic permeability of the rotor and stator iron is infinitely large compared to the permeability of free space, and therefore the H field in the iron is regarded as zero. Further on, is it assumed that the positive field direction is away from the center of the machine.

When applying Amperes Law, equation 4.1, on phase a, the field distribution produced by this phase for an angle θ is given in equation 4.13:

$$H_a(\theta) = \frac{N_s}{2l_g} i_a \cos(\theta) \tag{4.13}$$

Where:
- H_a Magnetic field
- N_s Number of windings
- l_g Length of air gap
- i_a Current in phase a
- θ Angle with respect to magnetic axis of phase a

Then it follows that the flux density and mmf acting on the air gap as a function of the angle can be as shown in equation 4.14 and 4.15, based on equation 4.3 and 4.2.

$$B_a(\theta) = \mu_0 H_a(\theta) = \left(\frac{\mu_0 N_s}{2l_g}\right) i_a \cos(\theta) \tag{4.14}$$

Where:
- B_a Flux Density
- μ_0 Permeability of free space
- N_s Number of windings
- l_g Length of air gap
- i_a Current in phase a
- θ Angle with respect to magnetic axis of phase a

$$F_a(\theta) = l_g H_a(\theta) = \frac{N_s}{2} i_a \cos(\theta) \tag{4.15}$$

Where:
- F_a mmf
- l_g Length of air gap
- N_s Number of windings
- i_a Current in phase a
- θ Angle with respect to magnetic axis of phase a

Up until now the focus has been on phase a, but the stator consists of three equal phase windings that are displaced by 120 degrees. The magnetic axis of each phase is shown in figure 4.6:

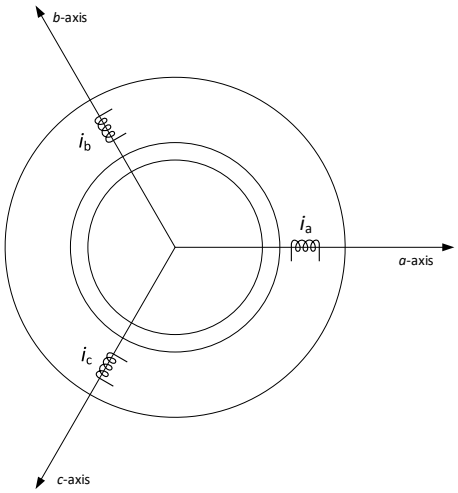

Figure 4.6: Magnetic axis of all three phases

Wye Arrangements of the Phase Windings and Kirchhoffs Law

The stator current $i_s(t)$, is the resulting current of all three phase currents, $i_a(t)$, $i_b(t)$ and $i_c(t)$. If one assume a wye-connection, then according to Kirchhoff's current law the sum must equal zero: $i_a(t) + i_b(t) + i_c(t) = 0$, shown in figure 4.7.

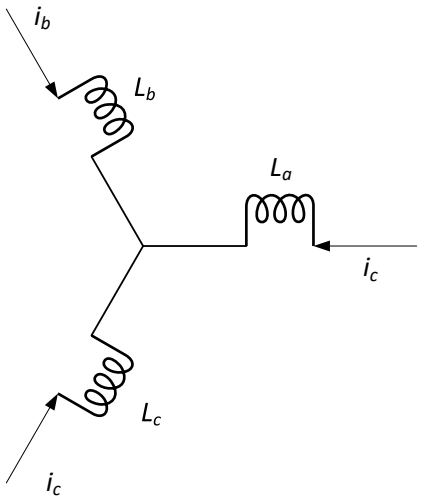

Figure 4.7: Kirchhoff's Current Law

Field Distribution in the Air Gap

The field distribution in the air gap can be expressed as space vectors, and for the three phases the mmf are as follows, shown in equation 4.16 to 4.18:

$$\vec{F_a}(t) = \frac{N_s}{2} i_a(t) \angle 0^\circ \tag{4.16}$$

$$\vec{F_b}(t) = \frac{N_s}{2} i_b(t) \angle 120^\circ \tag{4.17}$$

$$\vec{F_c}(t) = \frac{N_s}{2} i_c(t) \angle 240^\circ \tag{4.18}$$

Where:	$\vec{F}_i(t)$	mmf produced by phase i, $i \in (a, b, c)$
	N_s	Number of windings
	$i_i(t)$	Current in phase i, $i \in (a, b, c)$
	t	Time

It is now possible to obtain the resultant stator mmf distribution, by vector addition of the mmf produced by each phase individually, given in equation 4.19, and an example is shown in figure 4.8:

$$\vec{F}_s(t) = \vec{F}_a(t) + \vec{F}_b(t) + \vec{F}_c(t) = \hat{F}_s \angle \theta_{F_s} \tag{4.19}$$

Where:	$\vec{F}_s(t)$	Resultant mmf produced by phase a, b and c
	$\vec{F}_i(t)$	mmf produced by phase i, $i \in (a, b, c)$
	θ_{F_s}	Angle of resultant mmf vector with respect to the a-axis
	t	Time

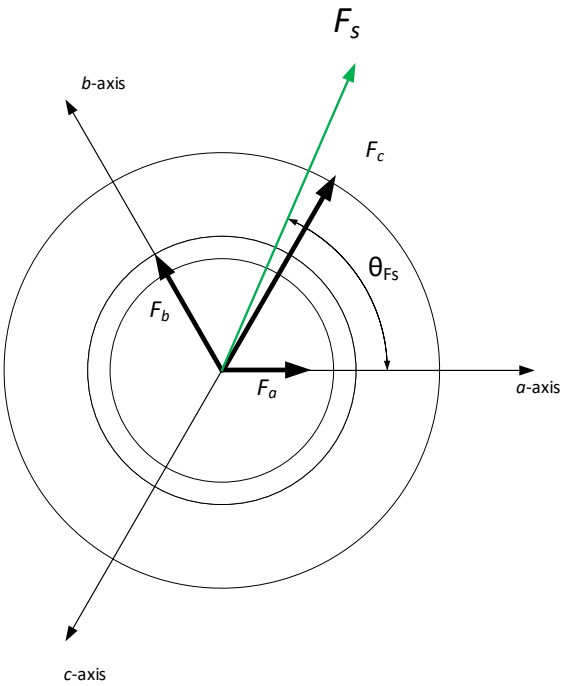

Figure 4.8: Combined Stator mmf

Expressions for the combined flux density and magnetic field can be obtained by the same strategy, shown in equation 4.20 and 4.21:

$$\vec{B}_s(t) = \vec{B}_a(t) + \vec{B}_b(t) + \vec{B}_c(t) = \hat{B}_s \angle \theta_{B_s} \tag{4.20}$$

$$\vec{H}_s(t) = \vec{H}_a(t) + \vec{H}_b(t) + \vec{H}_c(t) = \hat{H}_s \angle \theta_{H_s} \tag{4.21}$$

Where:	$\vec{B_s}(t)$	Stator flux produced by phase a, b and c
	$\vec{B_i}(t)$	Stator flux produced by phase i, $i \in (a, b, c)$
	$\hat{B_s}$	Amplitude of combined stator flux
	θ_{B_s}	Angle of combined stator flux with respect to the a-axis
	$\vec{H_s}(t)$	Field Intensity produced by phase a, b and c
	$\vec{H_i}(t)$	Field Intensity produced by phase i, $i \in (a, b, c)$
	$\hat{H_s}$	Amplitude of combined field intensity
	θ_{H_s}	Angle of combined field intensity with respect to the a-axis
	t	Time

Representation of the Combined Terminal Voltage and Current

It is possible at any time to measure the voltage and current at each phase, and the combined values are given by equation 4.22 and 4.23:

$$\vec{i_s}(t) = i_a(t)\angle 0^\circ + i_b(t)\angle 120^\circ + i_c(t)\angle 240^\circ = \hat{I_s}\angle\theta_{i_s} \tag{4.22}$$

$$\vec{v_s}(t) = v_a(t)\angle 0^\circ + v_b(t)\angle 120^\circ + v_c(t)\angle 240^\circ = \hat{V_s}\angle\theta_{v_s} \tag{4.23}$$

Where:	$\vec{i_s}(t)$	Combined stator current
	$i_i(t)\angle j$	Stator current in phase i, $i \in (a, b, c)$, $j \in (0^\circ, 120^\circ, 240^\circ)$.
	$\hat{i_s}$	Amplitude of combined stator current
	θ_{i_s}	Angle of combined stator current
	$\vec{v_s}(t)$	Combined Phase voltage
	$v_i(t)\angle j$	Phase voltage of i, $i \in (a, b, c)$, $j \in (0^\circ, 120^\circ, 240^\circ)$.
	$\hat{V_s}$	Amplitude of combined voltage
	θ_{v_s}	Angle of combined voltage
	t	Time

Reconstruct the Phase Components of $\vec{i_s}(t)$

In a wye arrangement it is possible to use Kirchhoff's current law to reconstruct the phase components on the basis of the combined stator current $\vec{i_s}(t)$, shown in equation 4.24 to 4.26:

$$i_a = \frac{2}{3}\hat{I_s}\cos\theta_{i_s} \tag{4.24}$$

$$i_b = \frac{2}{3}\hat{I_s}\cos(\theta_{i_s} - 120^\circ) \tag{4.25}$$

$$i_c = \frac{2}{3}\hat{I_s}\cos(\theta_{i_s} - 240^\circ) \tag{4.26}$$

Where: i_i Current in phase i, $i \in (a, b, c)$
$\hat{I}_s$ Amplitude of combined stator current
θ_{i_s} Angle of combined stator current with respect to the a-axis

The relation shown in equation 4.24 to 4.26 yield for all parameters as: $\vec{v_s}(t)$, $\vec{H}_s(t)$, $\vec{B}_s(t)$ and $\vec{\phi}_s(t)$.

Balanced Sinusoidal Steady State Excitation

In the normal mode of operation there is a balanced three phase sinusoidal steady state condition. Assuming sinusoidal voltages at frequency f applied to the stator, neglecting the rotor influence at this stage, results in magnetizing currents as shown in equation 4.27.

$$i_{ma} = \hat{I}_m \cos \omega t,\ i_{mb} = \hat{I}_m \cos(\omega t - 2\pi/3),\ i_{mc} = \hat{I}_m \cos(\omega t - 4\pi/3) \tag{4.27}$$

Where: $\hat{I}_m$ Peak value of magnetizing current
i_{mi} Magnetizing current in phase i, $i \in (a, b, c)$

Rotating Stator mmf Space Vector

When combining equation 4.22 and 4.27 the resultant magnetizing current is given by equation 4.28,

$$\vec{i_{ms}}(t) = \frac{3}{2}\hat{I}_m \angle \omega t = \hat{I}_{ms} \angle \omega t \tag{4.28}$$

Where : $\hat{I}_{ms} = \frac{3}{2}\hat{I}_m$

The same relation yield for mmf, $\vec{F_{ms}}(t) = \hat{F}_{ms} \angle \omega t$ and flux density, $\vec{B_{ms}}(t) = \hat{B}_{ms} \angle \omega t$. All these space vectors rotate CCW with the same speed called synchronous speed ω_{syn} for a 2 pole machine.

For a multi pole machine the relation is,

$$\omega_{syn} = \frac{\omega}{p/2},\ \text{where p is number of poles} \tag{4.29}$$

Induced Voltage in Stator Windings

By ignoring the resistance and leakage inductance in the stator windings and assuming no excitation in the rotor, the stator windings are purely inductive. The phase voltage and magnetization currents are then related as,

$$e_{ma} = L_m \frac{di_{ma}}{dt},\ e_{mb} = L_m \frac{di_{mb}}{dt},\ e_{mc} = L_m \frac{di_{mc}}{dt} \tag{4.30}$$

Where : $L_m =$ Magnetization inductance
e_{mi} Voltage in phase i, $i \in (a, b, c)$
i_{mi} Current in phase i, $i \in (a, b, c)$

Rotor Construction

In an PMSM, the B field produced by the rotor is determined by the permanent magnets, and there is no direct way of controlling this field [19, Ch.10]. The approach is then to calculate the torque exerted on the stator and transfer this torque to the motor foundation. It follows that the torque exerted on the rotor is equal in magnitude, but in the opposite direction.

Flux Density Produced by the Rotor

The permanent magnets are placed and shaped so that they produce a sinusoidally distributed flux density in the air gap. When using the a-axis as reference the presentation as space vector is shown in equation 4.31:

$$\vec{B}_r(t) = \hat{B}_r \angle \theta_m(t) \tag{4.31}$$

Where:
- $\vec{B}_r(t)$ Rotor flux density, varying with time t
- $\hat{B}_r$ Rotor flux density, constant value
- $\theta_m(t)$ Angle with respect to a-axis, varying with time t

Torque Production

The PPU are delivering controlled currents: $i_a(t)$, $i_b(t)$ and $i_c(t)$. These three stator currents are combined into the stator current space vector, $i_s(t)$, and is controlled by the PPU to lead the $\vec{B}_r(t)$ by 90 degrees, shown in equation 4.32,

$$\vec{i}_s(t) = \hat{I}_s \angle \theta_{i_s}(t) \text{ where } \theta_{i_s}(t) = \theta_{i_m}(t) + 90° \tag{4.32}$$

Where:
- $\vec{i}_s(t)$ Stator current, varying with time t
- $\hat{I}_r$ Stator current, kept constant
- $\theta_{i_s}(t)$ Angle with respect to a-axis, varying with time t

The reason for maintaining 90° between $\vec{i}_s(t)$ and $\vec{B}_r(t)$ is that all of the stator conductors will experience a force acting in the same direction from the rotor field. Even if the rotor is acting on the stator winding in CW direction, the rotor is the moving part and the direction of rotation is in the opposite direction, namely CCW. In figure 4.9 this is visualized.

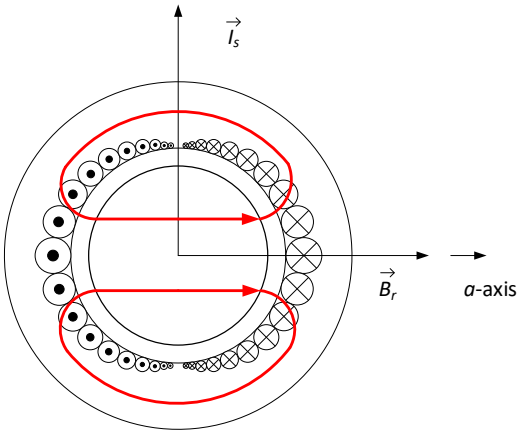

Figure 4.9: Torque Production

Rotor Position

For the PPU to be able to control the position of the $\vec{B}_r(t)$, it is necessary to know the rotor position with good accuracy. The more certain the position is, the more accurately the PPU can position the $\vec{B}_r(t)$ relative to the rotor. Encoders are used for this purpose in modern PMSM's.

Calculating the Torque

For calculating the torque produced by the motor, the equation 4.11 is used, $f_{em} = (i \times B) \cdot l$. When maintaining 90° between $\vec{i}_s(t)$ and $\vec{B}_r(t)$, and $\vec{i}_s(t)$ is ahead, then equation 4.11 becomes equation 4.33,

$$T_{em} = \Big(\pi \frac{N_s}{2} r l \hat{B}_r\Big) \hat{I}_s \tag{4.33}$$

Where:
- T_{em} Torque produced by the motor
- N_s Number of windings
- r Radius of rotor
- l Length of rotor
- $\hat{B}_r$ Flux density produced by the rotor

The parameters inside the bracket of equation 4.33 are machine parameters that do not change. The combined value is called the motor torque constant, k_T, unit is Nm/A. Equation 4.33 then simplifies to,

$$T_{em} = k_T \hat{I}_s \tag{4.34}$$

4.1.4 Mechanical System

When a mechanical system is connected to the PMSM the resulting angular speed is obtained as follows,

$$J\alpha = T_{em} - T_{load} \tag{4.35}$$

Where:
- J Combined inertia of rotor and load
- α Angular acceleration
- T_{em} Torque produced by the motor
- T_{load} Load torque included friction

4.1.5 Induced emf in Stator Windings

There is induced emf in the stator winding due to two flux distribution,

- The rotor rotates with $\omega_m(t)$ and $\vec{B}_r(t)$ rotates with the same velocity, this induces an emf according to equation 4.12, $e = (u \times B) \cdot l$
- The rotating flux density distribution due to $\vec{i}_s(t)$ induces emf in the stator windings

For the emf due to $\vec{B}_r(t)$,

$$\vec{e}_{ms,\vec{B}_r}(t) = j\omega_m \frac{3}{2}\Big(\pi r l \frac{N_s}{2}\Big) \vec{B}_r(t) \tag{4.36}$$

Where:	$\vec{e}_{ms,\vec{B}_r}(t)$	Induced emf due to rotating $\vec{B}_r(t)$
	j	Imaginary number
	ω_m	Angular velocity of rotor
	r	Radius of rotor
	l	Length of rotor
	$\vec{B}_r$	Flux density produced by the rotor

It is possible to define k_E in the same way as for k_T shown in equation 4.34, and equation 4.36 can be reformulated as,

$$\vec{e}_{ms,\vec{B}_r}(t) = \frac{3}{2} k_E \omega_m \angle\{\theta_m(t) + 90°\} \tag{4.37}$$

For the emf due to $\vec{i}_s(t)$,

$$\vec{e}_{ms,\vec{i}_s}(t) = j\omega_m L_m \vec{i}_s(t) \tag{4.38}$$

Where:	$\vec{e}_{ms,\vec{i}_s}(t)$	Induced emf due to rotating $\vec{i}_s(t)$
	j	Imaginary number
	L_m	Magnetizing inductance
	$\vec{i}_s$	Rotating current space vector

The combined induced emf is shown in equation 4.39,

$$\vec{e}_{ms}(t) = \vec{e}_{ms,\vec{B}_r}(t) + \vec{e}_{ms,\vec{i}_s}(t) \tag{4.39}$$

Equation 4.39 is graphically visualized in figure 4.10,

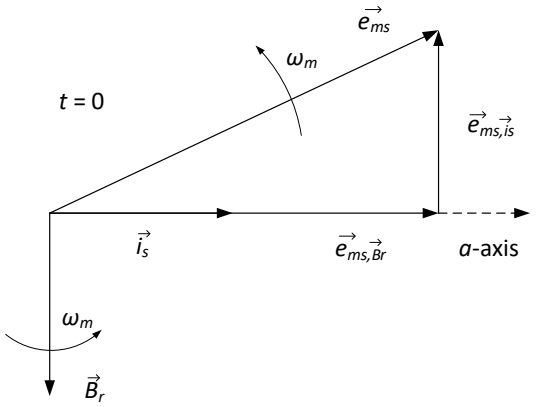

Figure 4.10: Induced emf, $\vec{e}_{ms,\vec{B}_r}(t)$ and $\vec{e}_{ms,\vec{i}_s}(t)$

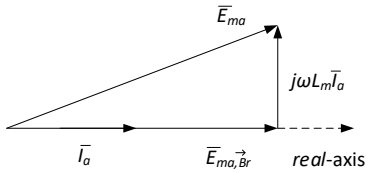

Figure 4.11: Induced emf for phase a

In figure 4.11 the space vector diagram for phase a is shown. It can be seen that it is reduced by a factor of 3/2 compared to the combined ems, and the orientation is equal as for the vector diagram in figure 4.10. This sums up the introduction to magnetic circuits and the basic understanding of conversion from electric energy to mechanical energy for a PMSM.

4.2 Four Quadrant Operation

The motor is bi-directional, meaning it can rotate CW and CCW. The motor produced torque T_{em} can be positive and negative, resulting in four different modes, shown in figure 4.12. When ω_m and T_{em} are pointing in opposite directions, the motor is in regenerative braking mode, and when they are pointing in the same direction it is called motoring mode. In this thesis only mode 1 and 4 are considered, due to the set up of the test bed. In section 2.2.5 the same four quadrants are explained for the pump, depending on aiding or resting load, shown in figure 2.6.

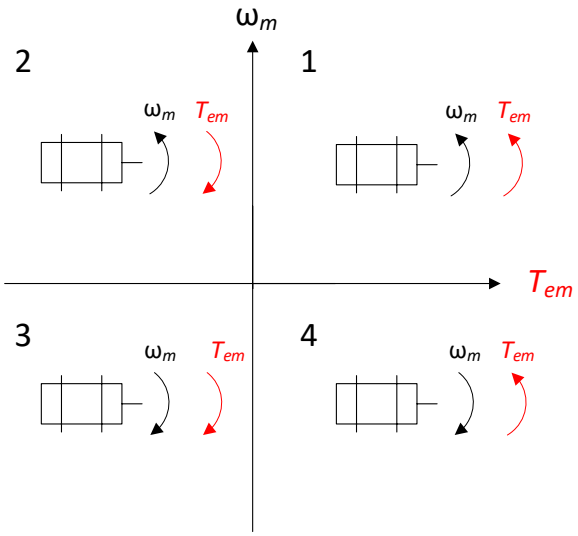

Figure 4.12: Four Quadrants of Operation

4.3 Power Processing Unit

The Power Processing Unit (PPU) is converts the utility to the desired 3-phase voltage, amplitude and phase, to enable the motor to produce the desired torque. Other names for this part can be: Voltage Source Converter (VSC), Drive or Inverter. The following section describes a method for ensuring linear modulation without any distortion of the sinusoidal voltage [20, p. 93-100] .

4.3.1 Switch Mode Converters

An example of a PPU supplying a PMSM is shown in figure 4.13 with symbols. The PPU consists of three main parts: The DC-source V_{dc}, the DC-Link with the middle selected as neutral point n, and the three legs of switches. The rectifier which converts the utility to DC-voltage is not shown. The switching device consists of transistors of the MOSFET type, and each leg consists of two MOSFET's controlled to be inverted of each other. By switching the MOSFET's in leg a, b and c on and off in a desired pattern, is it possible to produce any DC or AC voltage.

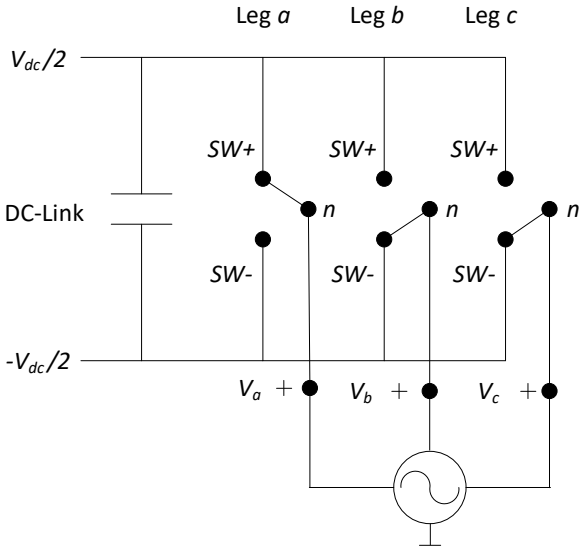

Figure 4.13: PPU with symbols

Introducing the switching vector (a, b, c) where an example vector can be: $(a, b, c) = (1, 0, 0)$ meaning leg a is on, then $v_a = V_{dc}/2$, leg b and c is off, then $v_b = v_c = -V_{dc}/2$. In figure 4.14 the six different possible combination are shown including the two zero vectors.

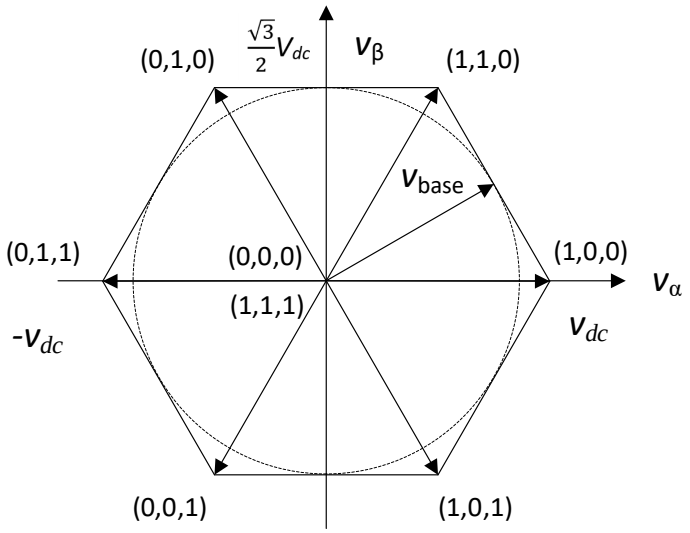

Figure 4.14: Space Vector Diagram

By combining the different switching states appropriately using Pulse Width Modulation (PWM), the total area within the hexagon in figure 4.14 is reachable, if linear modulation is desirable, the dashed circle with the radius $\frac{\sqrt{3}}{2}V_{dc}$ is then the limit. Linear modulation is obtained by combining the symmetrical sub-oscillation method and the minimum phase method.

4.3.2 Symmetrical Sub-oscillation Method

The symmetrical sub-oscillation method, also called the triangle comparison method, is used to generate the appropriate signal for the MOFSET. This compares the reference signal s'_a shown in figure 4.15 to the triangle carrier signal: When s'_a is larger than the carrier, $SW+$ is used, otherwise $SW-$ is used. Figure 4.13 shows the switching states, $SW+$ and $SW-$. Each leg has it own comparison logic.

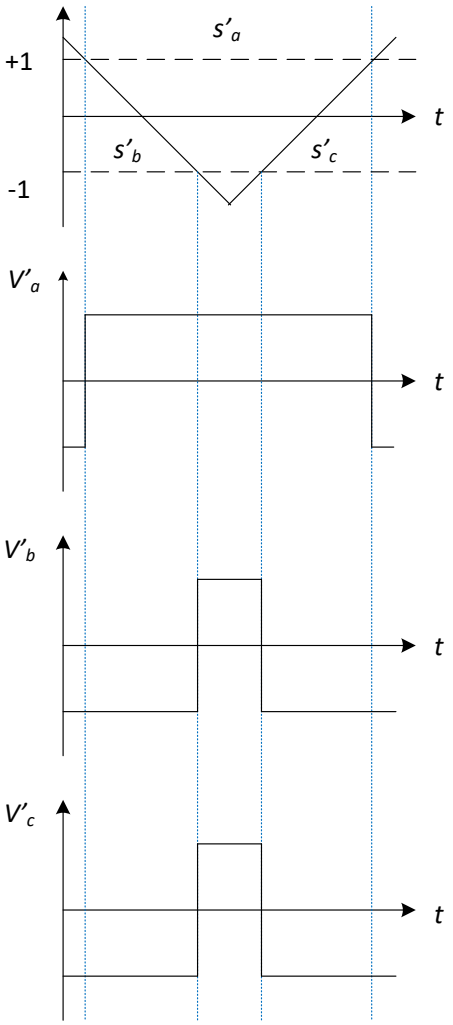

Figure 4.15: Symmetrical sub-oscillation method

First the procedure for being able to reach the total area of the hexagon is pointed out, then the procedure for ensuring linear modulation is given: Since the Y point is ungrounded, there will be no zero-sequence currents. The same deviation Δ is subtracted from all reference signals, shown in equation 4.40:

$$s'_{a,b,c} = s_{a,b,c} - \Delta \tag{4.40}$$

a zero-sequence component Δ is added but the resulting voltage space vector is not changed. To ensure that the total area of the hexagon is reachable, the condition in equation 4.41 must be met:

$$\max(s'_a, s'_b, s'_c) = -\min(s'_a, s'_b, s'_c) \tag{4.41}$$

Then Δ is, shown in equation 4.42:

$$\Delta = \frac{\max(s_a,\ s_b,\ s_c) + \min(s_a,\ s_b,\ s_c)}{2} \tag{4.42}$$

This makes the reference signal symmetric with respect to maximum and minimum values, thereby the name.

To prevent over modulation, the reference signals (s'_a, s'_b, s'_c) must not exceed the interval [-1,1], if so, the signal must be scaled such that the maximum value equals 1, shown in equation 4.43 and 4.44:

$$m = \max(s'_a, s'_b, s'_c); \text{ if } m > 1 : s'_{a,b,c} \rightarrow s'_{a,b,c}/m \tag{4.43}$$

Simplified:

$$s'_{a,b,c} \rightarrow \frac{s'_{a,b,c}}{\max(s'_a, s'_b, s'_c)} \tag{4.44}$$

The governing equations for the PPU are summarized in equations 4.45 to 4.47:

$$\begin{bmatrix} s_a(t) \\ s_b(t) \\ s_c(t) \end{bmatrix} = \frac{2}{V_{dc}} \begin{bmatrix} v_a \\ v_b \\ v_c \end{bmatrix} \tag{4.45}$$

$$s'_{a,b,c} = s_{a,b,c} - \frac{\max(s_a, s_b, s_c) + \min(s_a, s_b, s_c)}{2} \tag{4.46}$$

$$s'_{a,b,c} = \frac{s'_{a,b,c}}{\max(s'_a, s'_b, s'_c)} \tag{4.47}$$

4.3.3 Validation of the PPU

To validate the model of the PPU, the electric drive model was given a step input. There is no external load, only the PMSM moment of inertia and internal viscous friction is present. The steady state angular velocity is 1000 RPM, and only phase a is validated.

In figure 4.16 it is shown that the symmetrical sub-oscillation method is giving the expected output.

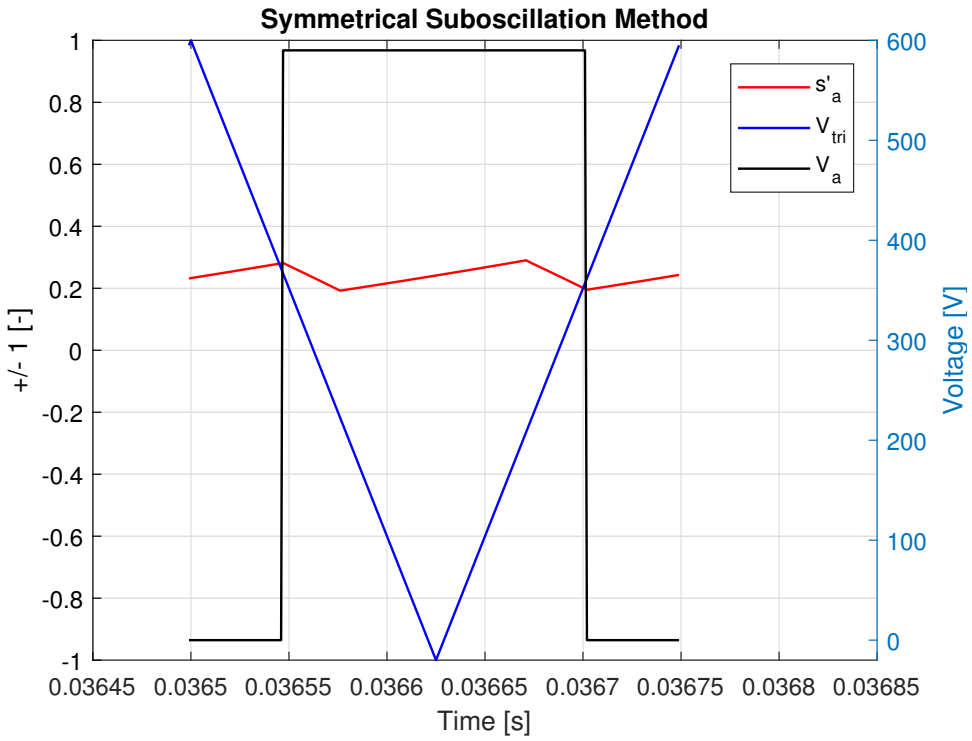

Figure 4.16: Sub-Oscillation Method validation

In figure 4.17, the PWM voltage to the PMSM is shown, as output of the PPU, and in addition the reference signal to the PPU.

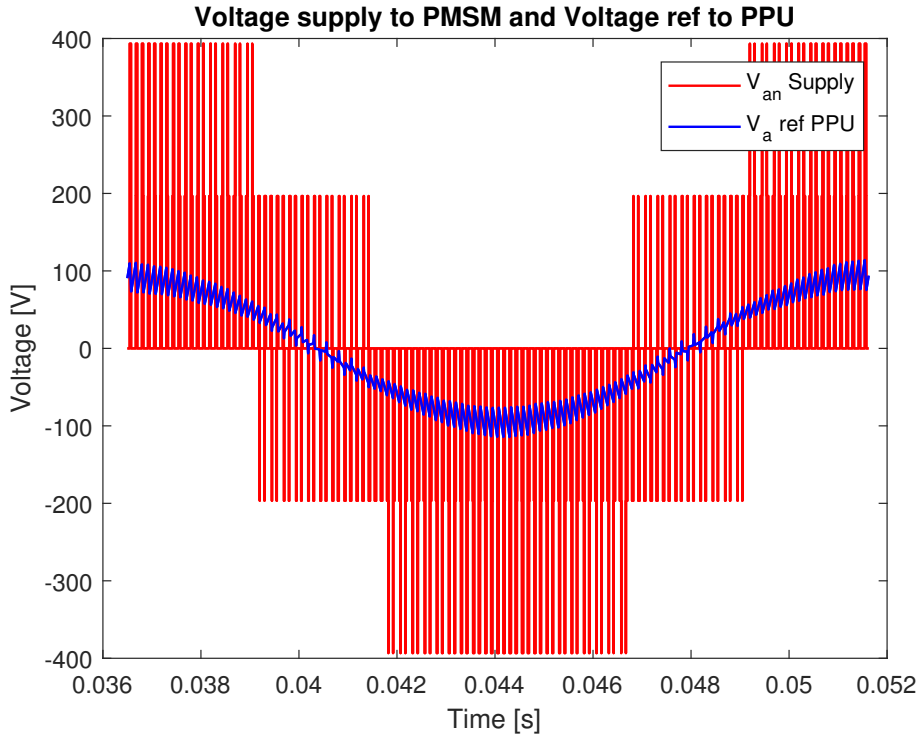

Figure 4.17: PPU validation

4.4 Modelling the PMSM

The following section introduces the governing equations needed for modelling the PMSM and explains how the Field Oriented Control (FOC) is implemented in the model. It is necessary to know the exact position of the rotor in order to control the position of the magnetic field set up by the stator currents. The position sensor in the PMSM covered in this thesis is an encoder having 128 increment per revolution. In order to control the currents in all three phases, it is beneficial to transform the currents into a two-axis rotating reference frame. This is valid due to: $i_a(t) + i_b(t) + i_c(t) = 0$. The reason for this transformation is that the current controller then sees DC-currents, making the controlling much easier. The transformation is called the Clarke-Park transform which is explained in the next section [20, ch. 2.6],

4.4.1 Clarke - Park Transformation

In figure 4.18, the stator currents are indicated by vectors: $i_a\angle 0°$, $i_b\angle 120°$ and $i_c\angle 240°$. For the reason of simplification it is possible to describe i_s by two vectors and a rotating reference frame according to the Clarke Park Transformation.

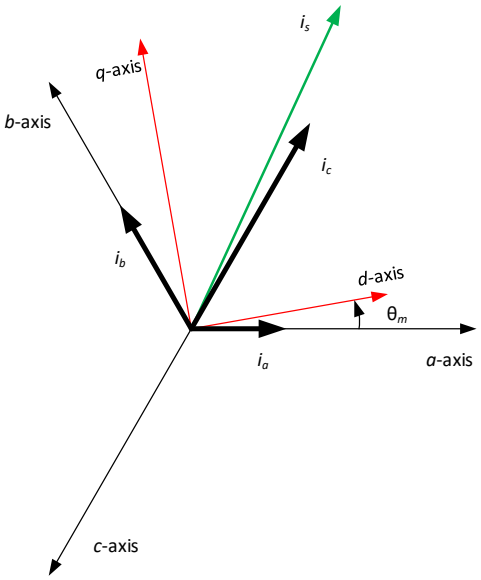

Figure 4.18: Clarke Park Transformation

The forward Clarke transform, is a three-phase-to-two-phase transformation, and the transformation matrix is shown in equation 4.48,

$$\begin{bmatrix} i_\alpha(t) \\ i_\beta(t) \end{bmatrix} = \begin{bmatrix} 1 & -\frac{1}{2} & -\frac{1}{2} \\ 0 & \frac{\sqrt{3}}{2} & -\frac{\sqrt{3}}{2} \end{bmatrix} \begin{bmatrix} i_a(t) \\ i_b(t) \\ i_c(t) \end{bmatrix} \tag{4.48}$$

The inverse transform, two-phase-to-three-phase is shown in equation 4.49,

$$\begin{bmatrix} i_a(t) \\ i_b(t) \\ i_c(t) \end{bmatrix} = \begin{bmatrix} \frac{2}{3} & 0 \\ -\frac{1}{3} & \frac{1}{\sqrt{3}} \\ -\frac{1}{3} & -\frac{1}{\sqrt{3}} \end{bmatrix} \begin{bmatrix} i_\alpha(t) \\ i_\beta(t) \end{bmatrix} \tag{4.49}$$

The forward Park transform is the transformation from a stationary reference frame to a rotating reference frame, shown in equation 4.50,

$$\begin{bmatrix} i_d(t) \\ i_q(t) \end{bmatrix} = \begin{bmatrix} \cos\theta_e & \sin\theta_e \\ -\sin\theta_e & \cos\theta_e \end{bmatrix} \begin{bmatrix} i_\alpha(t) \\ i_\alpha(t) \end{bmatrix} \tag{4.50}$$

The inverse Park transform is the transformation from the rotating reference frame to the stationary reference frame, shown in equation 4.51

$$\begin{bmatrix} i_\alpha(t) \\ i_\beta(t) \end{bmatrix} = \begin{bmatrix} \cos\theta_m & -\sin\theta_m \\ \sin\theta_m & \cos\theta_m \end{bmatrix} \begin{bmatrix} i_d(t) \\ i_q(t) \end{bmatrix} \tag{4.51}$$

The Clarke-Park transform is valid for currents and voltages. It is worth mentioning is that the names *dq* transform or *dq* axis theory are common names used for the transformation just explained.

4.4.2 Dynamic Model and Equivalent Circuit for the PMSM

In stationary frame the dynamic model for the system is given in equation 4.52 and shown in figure 4.19 [20, p.180].

$$L\frac{di^s}{dt} = v^s - Ri^s - E^s \tag{4.52}$$

The transformation to synchronous frame is shown in [20, p.180] and the result given in equation 4.53

$$L\frac{di}{dt} = v - (R + j\omega_1 L)i - j\omega_r\psi_R(\cos\tilde{\theta} + j\,\sin\tilde{\theta}),\ \text{where}\ \tilde{\theta} = \theta_r - \theta_1 \tag{4.53}$$

Where:

$\tilde{\theta}$	Difference between rotor flux angle and dq-axis angle
θ_r	Rotor flux angle
θ_1	dq-axis angle
ω_1	Fundamental frequency according to [p.24][20]
v	Synchronous frame voltage vector
i	Synchronous frame current vector
ψ_R	Rotor flux linkage
L	Inductance of stator windings
R	Resistance of stator windings

If $\theta_1 = \theta$, this is known as perfect field orientation, which means that the d-axis is located exactly equal to the rotor flux axis. From this, in steady state conditions, equation 4.53 is reduced to,

$$v = (R + j\omega_1 L)i + j\omega_r\psi_R \tag{4.54}$$

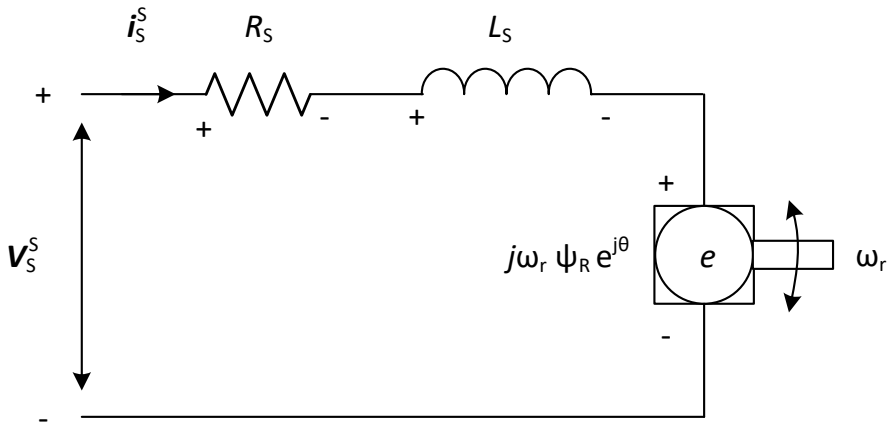

Figure 4.19: Dynamic model and equivalent circuit for the PMSM

By using, $i = i_d + ji_q$, it is possible to split equation 4.53 into one real part and one imaginary part, shown in equation 4.55 and 4.56, where the cross coupling terms are: $\omega L_s i_q$ and $\omega L_s i_q$.

$$L_S \frac{d\vec{i_d}}{dt} = \vec{v}_d - R_s i_d + \omega L_s i_q - j\omega_r \psi_R \tag{4.55}$$

$$L_S \frac{d\vec{i_q}}{dt} = \vec{v}_q - R_s i_q - \omega L_s \vec{i_d} - j\omega_r \psi_R \tag{4.56}$$

Electromagnetic Torque

From [20, p.165] the electromagnetic torque is given by equation 4.57.

$$\tau_e = \frac{3n_p}{2K^2} \psi_R i_q \tag{4.57}$$

Given that,

$$n_{po} = \frac{p}{2} \tag{4.58}$$

$$K = \frac{3}{2} \tag{4.59}$$

Substituting equation 4.58 and 4.59 into equation 4.57 it follows that,

$$\tau_e = \frac{3\frac{p}{2}}{2\left(\frac{3}{2}\right)^2} \psi_R i_q \tag{4.60}$$

$$\tau_e = \frac{p}{3} \psi_R i_q \tag{4.61}$$

Where:	τ_e	Electromagnetic torque
	n_{po}	Number of pole pairs
	K	Scaling factor
	ψ_R	Flux linkage rotor
	i_q	Current along q-axis
	p	Number of poles

This is how the electromagnetic torque is determined in the motor model.

4.5 Current and Speed Control, Harnefors

This section describes current control of AC PMSM drives. Current control is used for precise torque control and improving response time. It is also convenient for preventing the current from exceeding a certain maximum value [20, p. 120]. For ease, the first part introduces current control on DC drives. By dq-transformation of three phase AC to synchronous frame, the signals are converted to DC-signals in steady state. Hence, the DC current control principles will be built upon in the last part which concerns three phase permanent magnet synchronous machines.

Current Control for DC Motor Drives

The electrical dynamics for a DC motor are given by equation 4.62 [20, p.112].

$$v - Ri - L\frac{di}{dt} = E = \psi\omega_r \tag{4.62}$$

From equation 4.62 the transfer function $G_e(s)$ from voltage, v, to current, i, are given by equation 4.63 from [20, p.120]

$$G_e(s) = \frac{1}{sL + R} \tag{4.63}$$

A sketch of the closed loop current controller for a DC motor, where $G_e(s)$ is the electrical dynamics from equation 4.63, is shown in figure 4.20. The back emf, E, is a result of a mechanical response, which is significantly slower than the current dynamics, and hence disregarded seen from the electrical control loop. That is why E enters the control loop as a load disturbance after the current-controller [20, p.120].

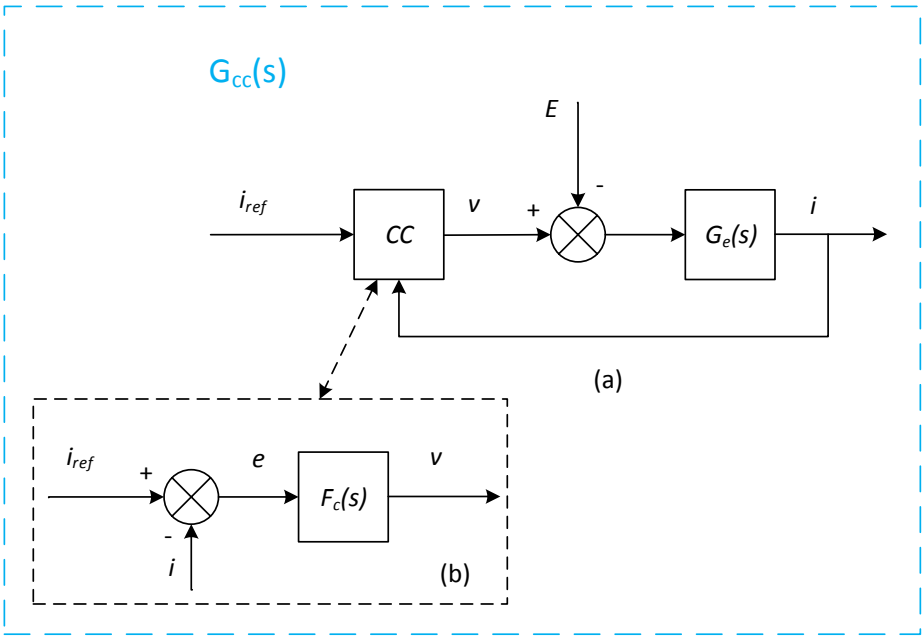

Figure 4.20: (a) Closed loop current control, (b) One-degree-of-freedom controller [20, p.120].

The error signal, e, shown in equation 4.64, is the difference between reference and actual current.

$$e = i_{ref} - i \tag{4.64}$$

One-Degree-of-Freedom Controller Design The electrical dynamics is of order one. Then it is enough with a first order controller and thus a PI-controller is appropriate. Figure 4.20 shows a "One-Degree-of-Freedom"-controller design. The name is due to the fact that the controller only has one input, in this case the error-signal, e, shown in equation 4.64. The transfer function for the PI-controller, F_c, is given in equation 4.65.

$$F_c(s) = k_p + \frac{k_i}{s} \tag{4.65}$$

The controller parameters k_p and k_i could be selected by trial and error, however, this is inconvenient. Since there are good estimates of the motor parameters that exist, a method called "direct synthesis" [20, p.121] is used. This method makes use of the relation between rise time, t_{rc}, and bandwidth , α_c, shown in equation 4.66. The rise time is typically in the millisecond range for a current controller.

$$\alpha_c t_r = ln9 \tag{4.66}$$

The calculation of the controller parameters are done by [20, p.121] and are briefly explained in equation 4.67, 4.68 and 4.69.

Considering the closed loop system from i_{ref} to i, the ideal transfer function $G_{cc}(s)$, see figure 4.20, is shown in 4.67.

$$G_{cc}(s) = \frac{\alpha_c}{s + \alpha_c} = \frac{\alpha_c/s}{1 + \alpha_c/s} \tag{4.67}$$

Where: G_{cc} Transfer function from i_{ref} to i
α_c Bandwidth of current control loop

That is, in a steady state performance there should be no control error because $G_{cc}(0) = 1$. Figure 4.20 of the current controller shows the closed loop transfer function which is shown in equation 4.68.

$$G_{cc}(s) = \frac{F_c(s)G_e(s)}{1 + F_c(s)G_e(s)} \tag{4.68}$$

So if $F_c(s)G_e(s) = \alpha_c/s$,

$$F_c(s) = \frac{\alpha_c}{s}G_e(s)^{-1} = \frac{\alpha_c}{s}(sL + R) = \alpha_c L + \frac{\alpha_c R}{s} \tag{4.69}$$

k_p and k_i are expressed in 4.70.

$$k_p = \alpha_c \hat{L} \text{ and } k_i = \alpha_c \hat{R} \tag{4.70}$$

The "hat"-values represent estimates of parameters when the exact value is not available, for instance concerning parameters that are temperature dependent such as coil resistance, R; $\hat{R}$ is an approximation of R, but normally they are considered equal.

Where:	$F_c(s)$	Current controller transfer function
	k_p	Proportional gain
	k_i	Integral gain
	t_r	10%-90% rise time
	α_c	Bandwidth
	$\hat{L}$	Approximated inductive resistance
	$\hat{R}$	Approximated coil resistance

Active Damper in a Two-Degree-of-Freedom Controller The purpose of including an active resistance in the controller is to reduce the steady state error [20, p.123]. An excessive steady state error is a typical problem when making pole cancellation, which is done in direct synthesis. Adjusting the k_i-gain in equation 4.70 could improve the accuracy at a certain degree, but at the same time it could result in an overshoot when the reference value is changing. Another way of improving performance is by adding an extra resistance, R_a, to an inner feedback loop as shown in figure 4.21. The active resistance is not a physically resistant; it's value which is proportional to the current is only an added resistance-value inside the control-system, hence it will not result in increased energy losses. The controller now has two inputs, both the error from the control signal and the actual current, i, via the active resistance, therefore the name "Two-Degree-of-Freedom"-controller. The back-emf feed forward signal, $\hat{E}$, which should a fairly good estimate of $E = \psi\omega_r$ shown in figure 4.21, is a remedy of poor load disturbance rejection.

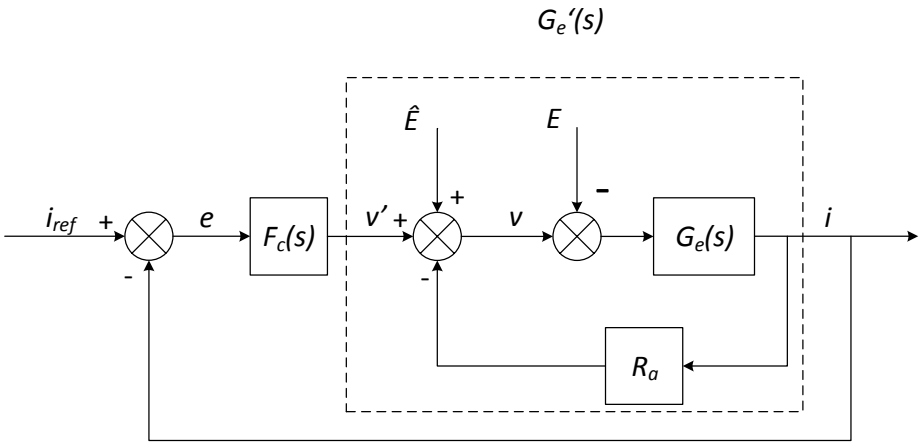

Figure 4.21: Block chart of the added active resistance to the controller [20, p.124].

By introducing the active resistance to the controller, the closed loop electric dynamics are given by equation 4.71, which has an increased resistance compared to equation 4.63.

$$G'_e(s) = \frac{1}{sL + R + R_a} \tag{4.71}$$

The new control parameters are determined by use of direct synthesis, shown in equation 4.72.

$$F_c(s) = \frac{\alpha_c}{s} G'_e(s)^{-1} = \alpha_c \frac{sL + R + R_a}{s} = k_p + \frac{k_i}{s} \tag{4.72}$$

That is,

$$k_p = \alpha_c \hat{L} \text{ and } k_i = \alpha_c(\hat{R} + R_a) \tag{4.73}$$

Selection of R_a should be done in a way that make the inner feedback loop $G'_e(s)$ as fast as the total system, and follow the relation given in equation 4.74 which give the new bandwidth of the system. Note that the active resistance speeds up the system by increasing the denominator!

$$\alpha_c = \frac{R + R_a}{L} \tag{4.74}$$

Then R_a is given by equation 4.75.

$$R_a = \alpha_c \hat{L} + \hat{R} \tag{4.75}$$

Substituting equation 4.74 into the expression for k_i in equation 4.73 result in the controller parameters for k_p and k_i,

$$k_p = \alpha_c \hat{L} \text{ and } k_i = \alpha_c^2 \hat{L} \tag{4.76}$$

Harnefors gives an example in [20, p.125] to show improved performance by implementing the active resistance in a controller; the error value is initially close to 10 %, and when adding the active damper, it is reduced to 1.3%.

(4.77)

Where:	$G'_e(s)$	Electric dynamics with active resistance
	$F_c(s)$	Current controller
	k_p	Proportional gain
	k_i	Integral gain
	α_c	Bandwidth
	$\hat{L}$	Approximated coil inductance
	$\hat{R}$	Approximated coil resistance

Anti wind-up and Voltage Saturation Until now, the current control has been considered an ideal, linear system. This is not always the case in a real world system. The armature voltages is limited by an upper and lower value, determined by the power electronic converter. For a large step in i_{ref} the limited armature voltage value may be exceeded. The true voltage then becomes a saturation of the reference voltage signal, $\bar{V}_{ref}$, shown in figure 4.22.

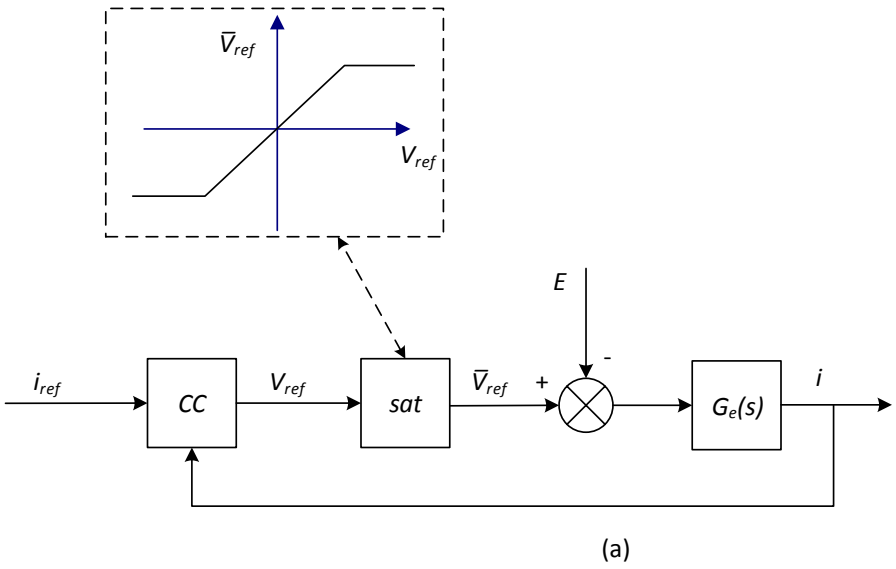

Figure 4.22: Block chart of saturation function for voltage V_{ref} [20, p.126].

Anti Wind-Up, "Back Calculation" Wind-up in the integral part of a controller results in overshoot and increased transient response time. There are several existing methods to prevent this problem. One method called "back calculation", which prevents integration when the signal saturates, is described in [20, pp.126-127] and included in figure 4.23.

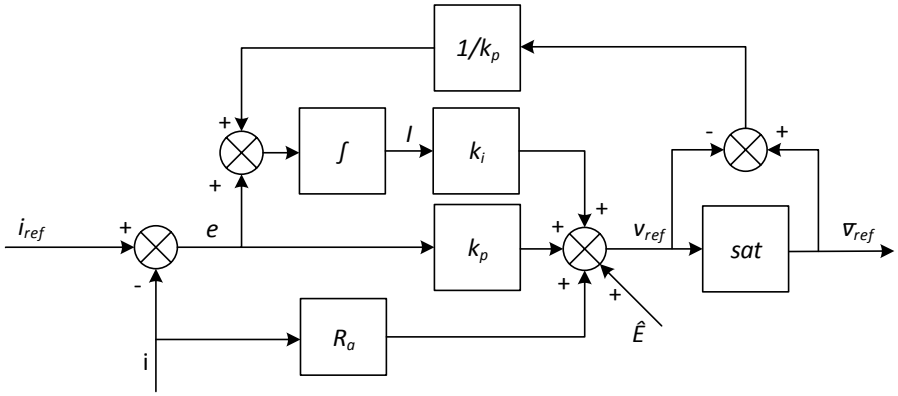

Figure 4.23: Block chart of anti-windup function[20, p.128].

The Complete Current Controller for a DC-motor Equations 4.78, 4.79 and 4.80 shows the complete controller, given mathematically, for the DC-motor.

$$\frac{dI}{dt} = e + \frac{1}{k_p}\left(\bar{v}_{ref} - v_{ref}\right) \tag{4.78}$$

$$v_{ref} = k_p e + k_i I - R_a i + \hat{E} \tag{4.79}$$

$$\bar{v}_{ref} = \text{sat}(v_{ref},\, V_{base}) \tag{4.80}$$

Where:	I	Integrator state variable
	e	Error signal for the current
	k_p	Proportional gain
	v_{ref}	Saturated voltage signal
	$\bar{v}_{ref}$	Voltage reference signal
	k_i	Integral gain
	R_a	Active damper value
	$\hat{E}$	Approximated back emf
	V_{base}	Limited armature voltage determined by the power electronic converter

This concludes the section concerning control of the DC-motor. The next section, which deals with control of the PMSM, will build upon the concepts used for DC-machine control. A speed controller in cascade with the current controller is also often convenient also for a DC-machine. This topic is discussed in the next section.

4.5.1 Design of Synchronous Frame Controllers

This section concerns the control of a three phase permanent magnet AC-machine and will build upon the basic control principles of a DC-machine introduced in section 4.5. It is convenient to start with the DC-motor due to the fact dq-transformation converts sinusoidal AC signals into DC signals in steady state. The control-method that makes use of dq-transformation was invented in the 70's [21, p.299] and is known as Field Oriented Control. In this section, PI-controllers are the selected option for controlling. They are often the most attractive choice for several reasons; they work properly, they are simple, and they perform well [20, p.184].

Current Controller Considering equations 4.55 and 4.56, which describes the dynamic model of a PMSM, they represent two cross-coupled first order subsystems. The terms $j\omega_1 i_d$ and $j\omega_1 i_q$ respectively represent the cross coupling which should be cancelled out by the method described in [20, pp. 185-186]. By adding a decoupler, $j\omega_1 \hat{L} i$, to the inner active resistance shown in figure 4.24 and in equation 4.81, the cross-coupling is removed.

$$v = v' + \left(j\omega_1 \hat{L} - R_a\right) i + \hat{E} \tag{4.81}$$

Where:	v	Input voltage to motor
	v'	Output voltage from current controller
	ω_1	Fundamental frequency according to [p.24][20]
	$\hat{L}$	Approximated inductance
	R_a	Active resistance
	i	Current
	$\hat{E}$	Approximated back-EMF

The back emf term $\hat{E}$ is an optional feed forward of the back emf to reject poor load-disturbance [20, 123]. It is expressed for PMSM in equation 4.82.

$$\hat{E} = j\omega_1 \hat{\psi}_R \tag{4.82}$$

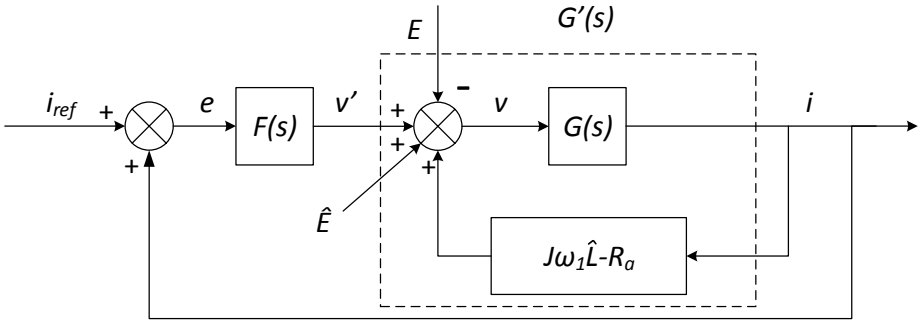

Figure 4.24: Block chart for the active damper and decoupler. The anti wind-up function is omitted in the figure but still incorporated in the controller block $F(s)$ as shown in figure 4.23

The cross coupling has been removed, shown in equation 4.83, which is equal to equation 4.71 for DC-control, containing no imaginary part. The dynamics are speeded up from $\frac{R}{L}$ to $\frac{R+R_a}{L}$ and the new electric dynamics are shown in equation 4.84

$$L\frac{di}{dt} = v' - (R + R_a)i - \tilde{E}, \text{ where } \tilde{E} = E - \hat{E} \tag{4.83}$$

$$G'(s) = \frac{1}{sL + R + R_a} \tag{4.84}$$

As it is a first order system, a PI-controller is appropriate.

$$F(s) = k_p + \frac{k_i}{s} \tag{4.85}$$

The controller parameters and active resistance are given in equation 4.86 and 4.87.

$$k_p = \alpha_c \hat{L} \text{ and } k_i = \alpha_c(\hat{R} + R_a) \tag{4.86}$$

$$\frac{R + R_a}{L} = \alpha_c \Longrightarrow R_a = \alpha_c \hat{L} - \hat{R} \tag{4.87}$$

Current Controller in dq-frame The current controller in the dq-frame are given by equations 4.88, 4.89 and 4.90.

$$e = i - i_{ref} \tag{4.88}$$

$$\frac{dI}{dt} = e \tag{4.89}$$

$$v_{ref} = k_p e + k_i I + (j\omega_1 \hat{L} - r_a)i + \hat{E}, \text{ where } I = I_d + jI_q \tag{4.90}$$

Speed Controller A speed loop is often used in combination with the position loop. This constitutes a cascade structure of control. Figure 4.25 shows the speed controller with a implemented active damper, b_a.

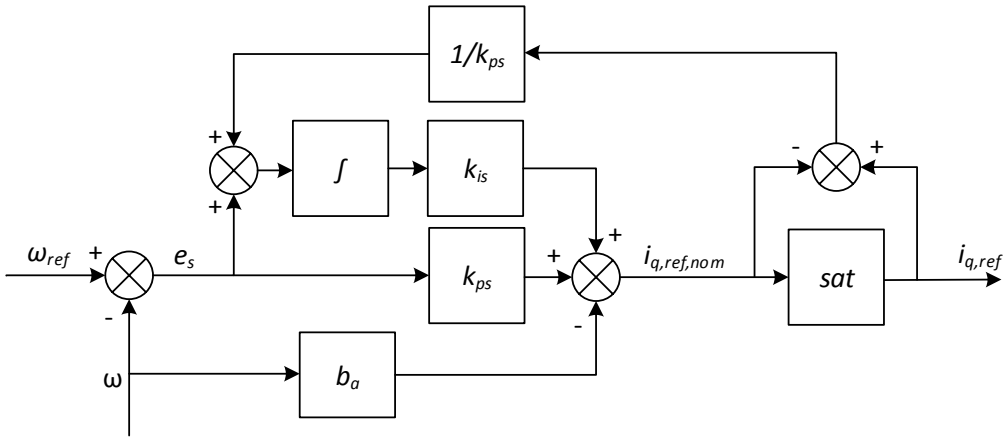

Figure 4.25: Block chart of speed controller with B_a as an active damper.

Similar to the active resistance in the current controller, adding an active viscous damper to the speed loop will increase the bandwidth. This is shown in [20, p.132] where the bandwidth of the speed loop is expressed by equation 4.91. Notice that the active viscous damper multiplied with the flux linkage is added to the viscous damping constant in the denominator of the fraction, hence the bandwidth is increased.

$$\alpha_s = \frac{b_a\psi + b}{J_m} \tag{4.91}$$

Where:
- α_s Bandwidth of the speed loop
- b_a Active viscous damper
- ψ Flux linkage
- b Viscous damping constant
- J_m Moment of inertia for the motor

The bandwidth of the speed loop, α_s, should be approximately ten times lower than the current loop [20, p.131], shown in equation 4.92. Using scaling factor $K = \frac{3}{2}$, the active damper and controller parameters are given by equation 4.93, 4.94 and 4.95 from [20, p.172].

$$\alpha_s \leq 0.1\alpha_c \tag{4.92}$$

$$b_a = \frac{2K^2(\alpha_s\hat{J}_m - \hat{b})}{3n_p^2\hat{\psi}_R}|_{k=\frac{3}{2}} = \frac{3}{2}\frac{(\alpha_s\hat{J}_m - \hat{b})}{n_p^2\hat{\psi}_R} \tag{4.93}$$

$$k_{ps} = \frac{2K^2\alpha_s\hat{J}_m}{3n_p^2\hat{\psi}_R}|_{k=\frac{3}{2}} = \frac{3}{2}\frac{\alpha_s\hat{J}_m}{n_p^2\hat{\psi}_R} \tag{4.94}$$

$$k_{is} = \frac{2K^2\alpha_s^2\hat{J}_m}{3n_p^2\hat{\psi}_R}|_{k=\frac{3}{2}} = \frac{3}{2}\frac{\alpha_s^2\hat{J}_m}{n_p^2\hat{\psi}_R} \tag{4.95}$$

Where:	α_s	Bandwidth of the inner speed-loop
	α_c	Bandwidth of the inner current loop
	b_a	Active viscous damping, speed loop
	K	Space vector scaling constant
	$\hat{J}$	Inertia of the motor
	$\hat{b}$	Approximated viscous damping factor
	n_p	Number of pole pairs
	$\hat{\psi}_R$	Estimated rotor flux

The speed controller are given mathematically by equation 4.96, 4.97, 4.98 and 4.99.

$$e_s = \omega_{ref} - \omega_r \tag{4.96}$$

$$i_{q,ref,nom} = k_{ps} e_s + k_{is} I_s - b_a \omega_r \tag{4.97}$$

$$i_{q,ref} = \text{sat}\left(i_{q,ref,nom}, \sqrt{I_{max}^2 - i_{d,ref}^2}\right) \tag{4.98}$$

$$I_s = e_s + \frac{1}{k_{ps}} \left(i_{q,ref} - i_{q,ref,nom}\right) \tag{4.99}$$

Where:	e_s	Error signal to the speed controller
	ω_{ref}	Reference speed
	ω_r	Actual rotor speed
	$i_{q,ref,nom}$	i_q reference signal from speed controller and active damper
	k_{ps}	Proportional gain, speed controller
	k_{is}	Integral gain, speed controller
	b_a	Active viscous damper
	I_s	Speed integrator state variable
	$i_{q,ref}$	Limited i_q signal out from saturation function
	I_{max}	Short term maximum allowed stator current
	$i_{d,ref}$	i_d reference signal

This concludes the section concerning the theory behind the control of a PMSM-motor. The theory has discussed both the cascade structure of a PI-controlled current loop and speed loop. The next section concerns the actual BoschRexroth controller highlighting how it is similar to the theory and how it is different.

4.5.2 Current and Speed Control, Bosch Rexroth

The controller architecture in the Bosch Rexroth drive is accessible via the user manuals. It is most likely that Bosch-Rexroth does not provide all of the information about their control system. Based on what is accessible, a rough sketch is shown in figure 4.26. PI-controllers are used for velocity and current control. For both i_q and i_d the same PI-controller is used. The active resistance and decoupler are not used in the inner current loop of the Bosch Rexroth controller. Likewise in the speed loop, there is no active damper.

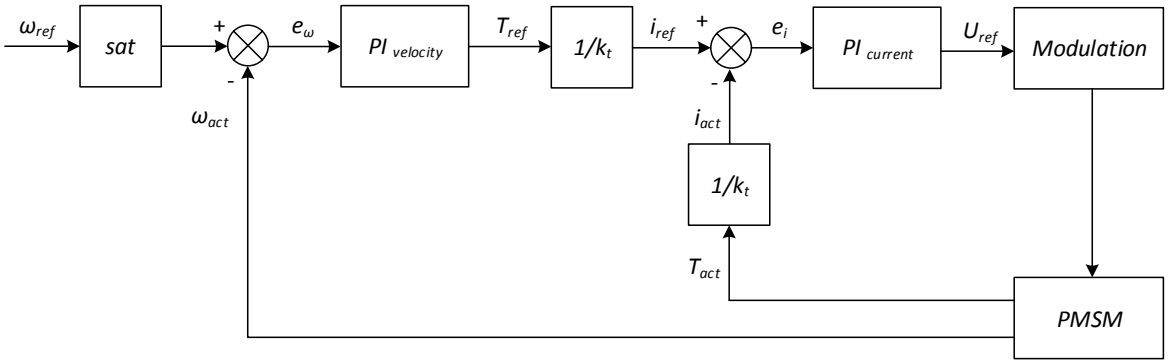

Figure 4.26: A sketch of the motor control system in the actual motor drive IndraDrive.

Auto Tune of Controllers

To ensure optimal controller setting for different use of the PMSM, an auto tune procedure can be run. This will provide the settings for the current and speed controllers.

4.5.3 Validating the PMSM

In the process of validating the total system, this section presents the results regarding the stand alone PMSM. By applying the same input to the model as to the real motor, it is possible to compare several output parameters as a measure of how accurate the model is. Testing the motor without external load will give limited results, but as an initial validation the experimental results are considered useful, being aware of the uncertainty regarding the motor friction; the data sheet do not provide any information regarding static or viscous friction. During testing, estimated parameters are used.

Step Profile

Figure 4.27 and 4.28 show the velocity and current I_q for the Simulink model and the electric motor. As seen in figure 4.27, the rise time is very similar in the model and the motor. The model has a slightly higher overshoot.

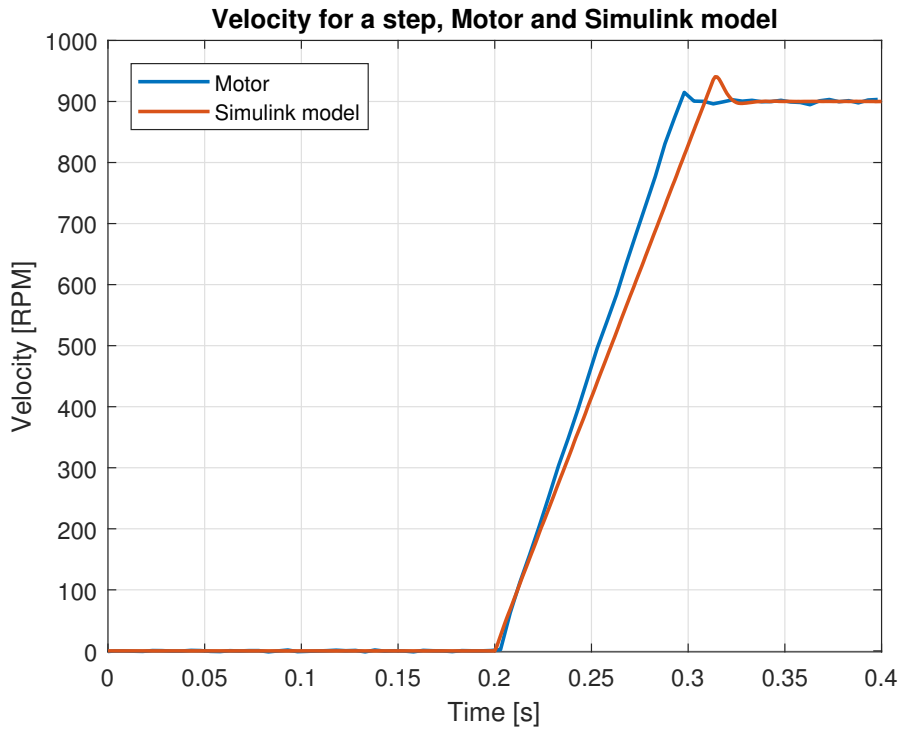

Figure 4.27: For a step, the velocity are shown for motor and Simulink model.

As seen in figure 4.28 the current I_q in the model deviates from the current in the motor. This could be explained by the uncertainty concerning the friction in the motor; including the viscous friction and stiction friction which prevent stationary surfaces from being set in motion. Bosch-Rexroth do not provide any value for this parameter hence a value is determined by trial and error.

The motor is limited to an acceleration of 1000 rad/s^2 recommended by the co-supervisor Daniel Hagen. The acceleration limit was implemented in the Simulink model as a saturation function in the velocity controller. From maximum angular acceleration a maximum current can be determined by equation 4.100. This is the torque-balance equation for the motor when neglecting the viscous damping and load torque.

$$J_m \alpha_{max} = T_{em,max} \tag{4.100}$$

From equation 4.61 the electro magnetic torque is approximated as shown in equation 4.101,

$$T_{em} \approx 0.87\, i_q \tag{4.101}$$

The maximum torque is then limited by the maximum current shown in equation .

$$J_m \alpha_{max} = 0.87\, i_{q,max} \tag{4.102}$$

$$i_{q,max} = \frac{J_m \alpha_{max}}{0.87} \tag{4.103}$$

$$= 3.33 \text{ A} \tag{4.104}$$

where:	α_{max}	Maximum acceleration of motor, PLC
	i_q	Current along q-axis
	$i_{q,max}$	Maximum allowed current, PLC
	$T_{em,max}$	Maximum electro mechanical torque, PLC
	T_{em}	Electro mechanical torque

The I_{max} value is used in the velocity-controller saturation function to limit the acceleration.

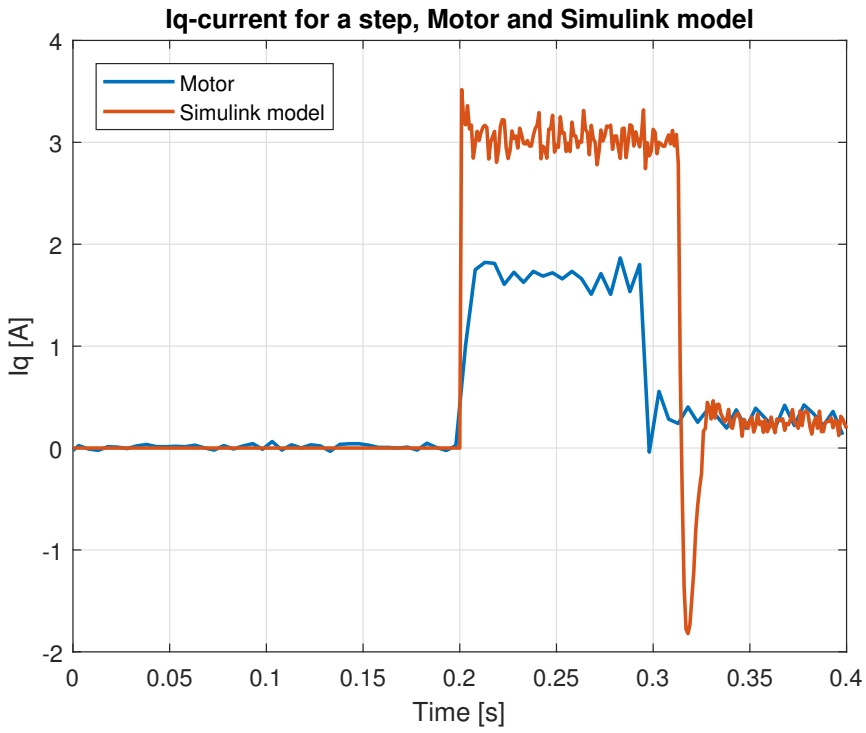

Figure 4.28: For a step, the velocity are shown for motor and Simulink model.

4.5.4 Replacing the PMSM with a Transfer Function

To simplify the Simulink model and thereby save simulation time, it is suggested to replace the PMSM with a transfer function. This is possible due to the different time constants for the PMSM and the hydraulic system, in which the PMSM is significantly faster. The suggested transfer function is shown in equation 4.105,

$$G(s) = \frac{K}{\frac{s^2}{\omega_0^2} + \frac{2\zeta s}{\omega_0} + 1} \tag{4.105}$$

Where:	$G(s)$	Transfer Function
	K	Gain
	ω_0	Natural frequency
	ζ	Damping coefficient
	s	Laplace operator

When choosing the parameters, $K = 1$, $\omega_0 = 200$ and $\zeta = 0.45$, the results are shown in figure 4.29 for the motion profile and in figure 4.30 for the step profile. The result confirms that the replacement is legitimate, and introduced errors are negligible.

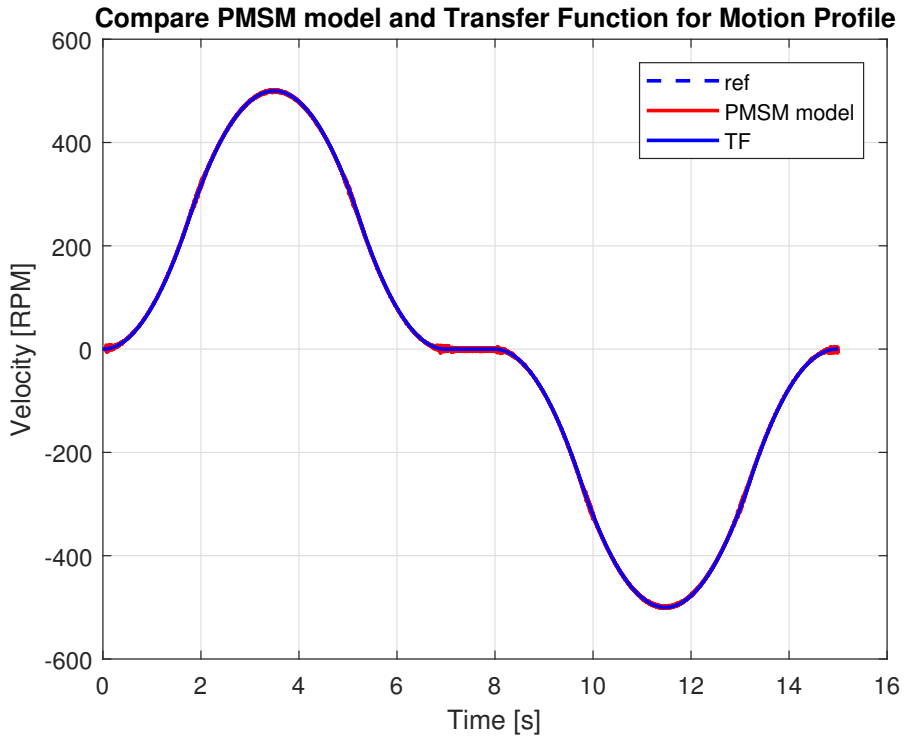

Figure 4.29: PMSM and TF, compare motion profile

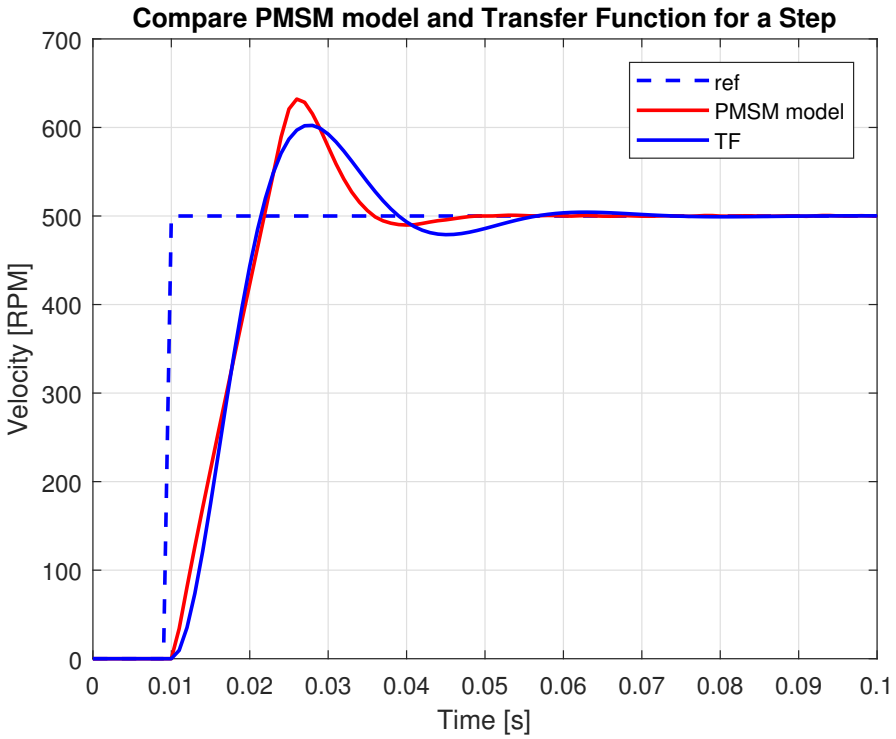

Figure 4.30: PMSM and TF, compare step profile

Chapter 5

Modelling the Mechanical System

As an introduction to the mechanical system, some steady state calculations are carried out; Inertia of the combined payload of the boom and load, reaction forces applied on the cylinder and finally the effective mass at a given boom angle.

5.1 Moment of Inertia

This section shows calculations of the moment of inertia for the arm around the rotation point, A, shown in figure 5.1. Steiner's Parallel theorem [22, p.431], shown in equation 5.1, is used for calculating the moment of inertia of the beam. The payload is considered a point load, calculated by equation 5.4. Summing up the values result in a total moment of inertia for the arm, shown in equation 5.7.

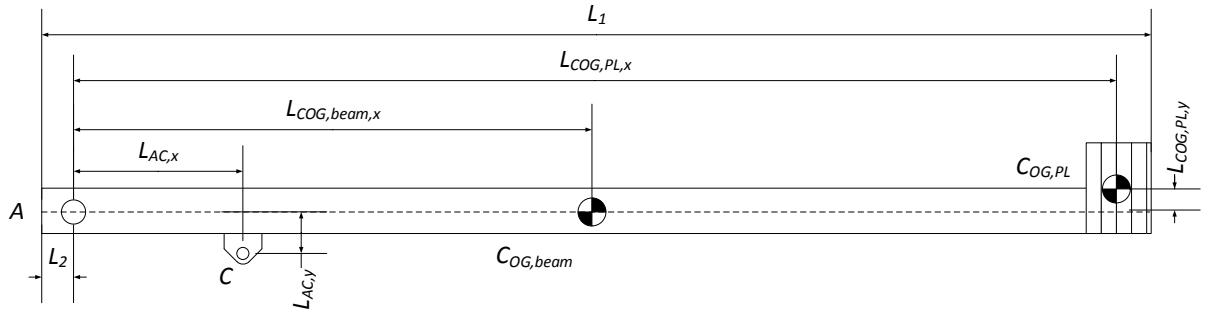

Figure 5.1: Effective force acting on the cylinder.

L_1	=	3680	mm
L_2	=	80	mm
$L_{COG,beam,x}$	=	1760	mm
$L_{AC,x}$	=	550	mm
$L_{AC,y}$	=	130	mm
$L_{COG,PL,x}$	=	3492	mm
$L_{COG,PL,y}$	=	64	mm
m_{beam}	=	82	kg
m_{pl}	=	320	kg

$$I_{beam} = I_{CG,beam} + m_{beam} \cdot L^2_{COG,beam,x} \text{ , where } I_{CG,beam} = \frac{1}{12} m_{beam} \cdot L_1^2 \tag{5.1}$$

$$= \frac{1}{12} \cdot 82\,\text{kg} \cdot (3.68\ \text{m})^2 + 82\,\text{kg} \cdot (1.76\,\text{m})^2 \tag{5.2}$$

$$= 346.54\,\text{kgm}^2 \tag{5.3}$$

$$I_{pl} = m_{pl} R_{pl}^2, \text{ where } R_{pl} = \sqrt{L^2_{COG,PL,x} + L^2_{COG,PL,y}} \tag{5.4}$$

$$= 320\,\text{kg} \cdot \left((3.492\,\text{m})^2 + (0.064\,\text{m})^2\right) \tag{5.5}$$

$$= 3903.41\,\text{kgm}^2 \tag{5.6}$$

$$I_{tot} = I_{beam} + I_{pl} \tag{5.7}$$

$$= (346.54 + 3903.41)\,\text{kgm}^2 \tag{5.8}$$

$$= 4250.0\,\text{kgm}^2 \tag{5.9}$$

Where:	I_{beam}	Moment of inertia for a beam
	$I_{CG,beam}$	Moment of inertia for a beam around centre of gravity
	m_{beam}	Mass of the beam
	$L_{COG,beam}$	Distance from centre of gravity to rotational point, equal to $L_{COG,beam,x}$ figure 5.1
	L_1	Length of beam
	I_{pl}	Moment of inertia of pay load
	m_{pl}	Mass of pay load
	R_{pl}	Length from pay load centre of gravity to rotational point A
	$L_{COG,PL,x}$	Length from A to centre of gravity for pay load in x-direction
	$L_{COG,PL,y}$	Length from A to centre of gravity for pay load in y-direction
	I_{tot}	Total moment of inertia for arm

5.2 Steady State Reaction Forces

To determine the force acting on the cylinder the steady state reaction forces are calculated. On figure 5.2 the relevant measures are given.

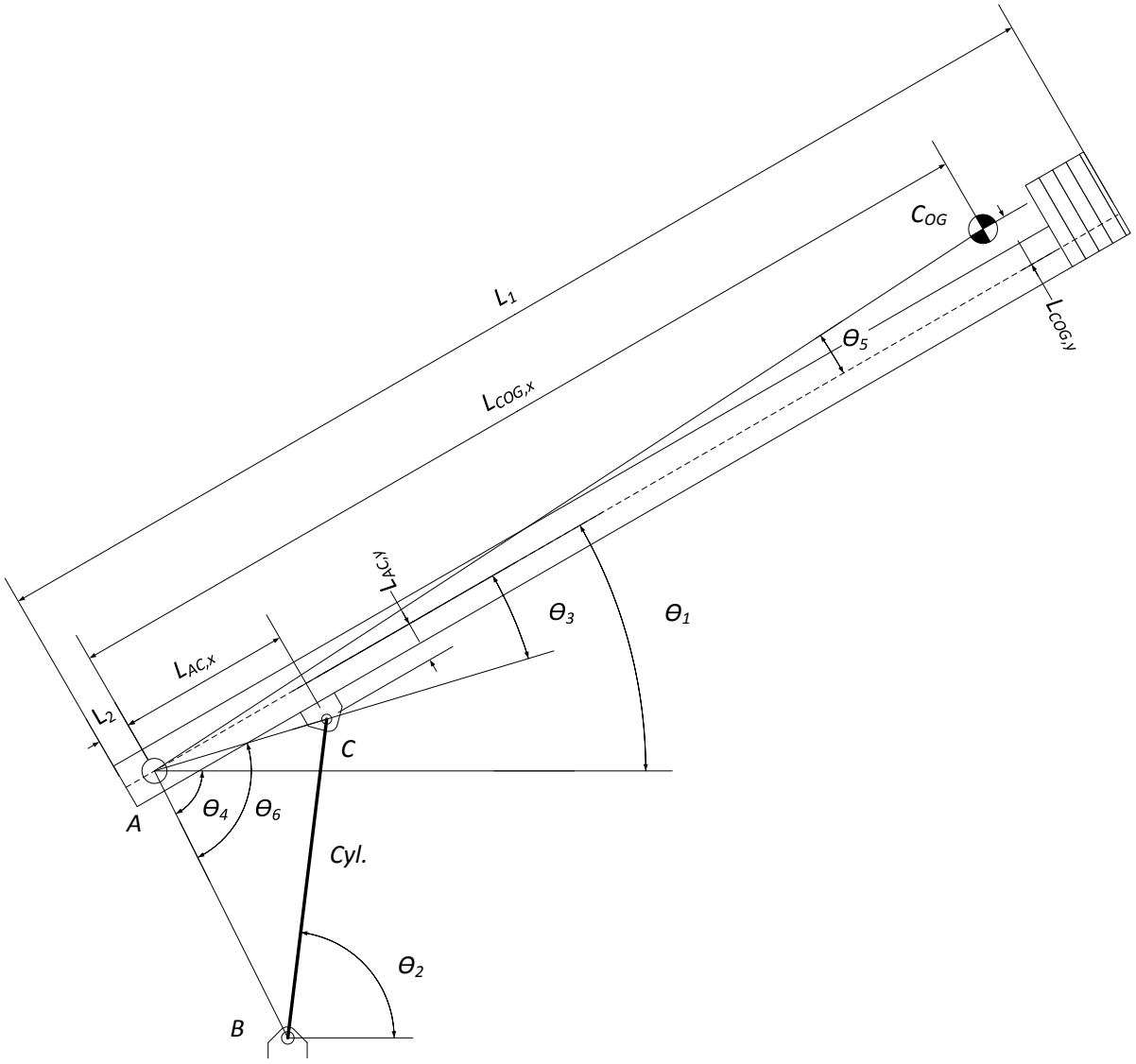

Figure 5.2: Model of the crane.

The static distances are computed as follows:

$$L_{ab} = \sqrt{{L_{abx}}^2 + {L_{aby}}^2} \tag{5.10}$$

$$L_{ac} = \sqrt{{L_{acx}}^2 + {L_{acy}}^2} \tag{5.11}$$

$$L_{ag} = \sqrt{{L_{agx}}^2 + {L_{agy}}^2} \tag{5.12}$$

The static angles are computed as follows:

$$\theta_3 = tan^{-1}\left(\frac{L_{acy}}{L_{acx}}\right) \tag{5.13}$$

$$\theta_4 = tan^{-1}\left(\frac{L_{aby}}{L_{abx}}\right) \tag{5.14}$$

$$\theta_5 = tan^{-1}\left(\frac{L_{acg}}{L_{agx}}\right) \tag{5.15}$$

The cylinder stroke is 500 mm, and is in the range: 772 mm to 1272 mm, then,

$$L_{bc} = 772 + x \tag{5.16}$$

Where x = cylinder stroke.

By applying of Law of Cosine on $\triangle_{ABC}$, θ_6 is computed as a function of the cylinder stroke,

$$\theta_6 = \cos^{-1}\left(\frac{{L_{ab}}^2 + {L_{ac}}^2 - {L_{bc}}^2}{2L_{ab}L_{ac}}\right) \tag{5.17}$$

then θ_1 is computed,

$$\theta_1 = \theta_6 - \theta_4 + \theta_3 \tag{5.18}$$

the distance BC is computed,

$$L_{bcx} = L_{ac}\cos(\theta_1 - \theta_3) - L_{abx} \tag{5.19}$$

$$L_{bcy} = L_{ac}\sin(\theta_1 - \theta_3) - L_{aby} \tag{5.20}$$

and θ_2,

$$\theta_2 = tan^{-1}\left(\frac{L_{bcy}}{L_{bcx}}\right) \tag{5.21}$$

The force acting on the cylinder is then,

$$F_{cyl} = \frac{L_{ag}\cos(\theta_1 + \theta_5)mg}{L_{ac}\sin(\theta_2)\cos(\theta_1 - \theta_3) - \cos(\theta_2)\sin(\theta_1 - \theta_3)} \tag{5.22}$$

In figure 5.3 the force acting on the cylinder is shown as a function of the cylinder stroke.

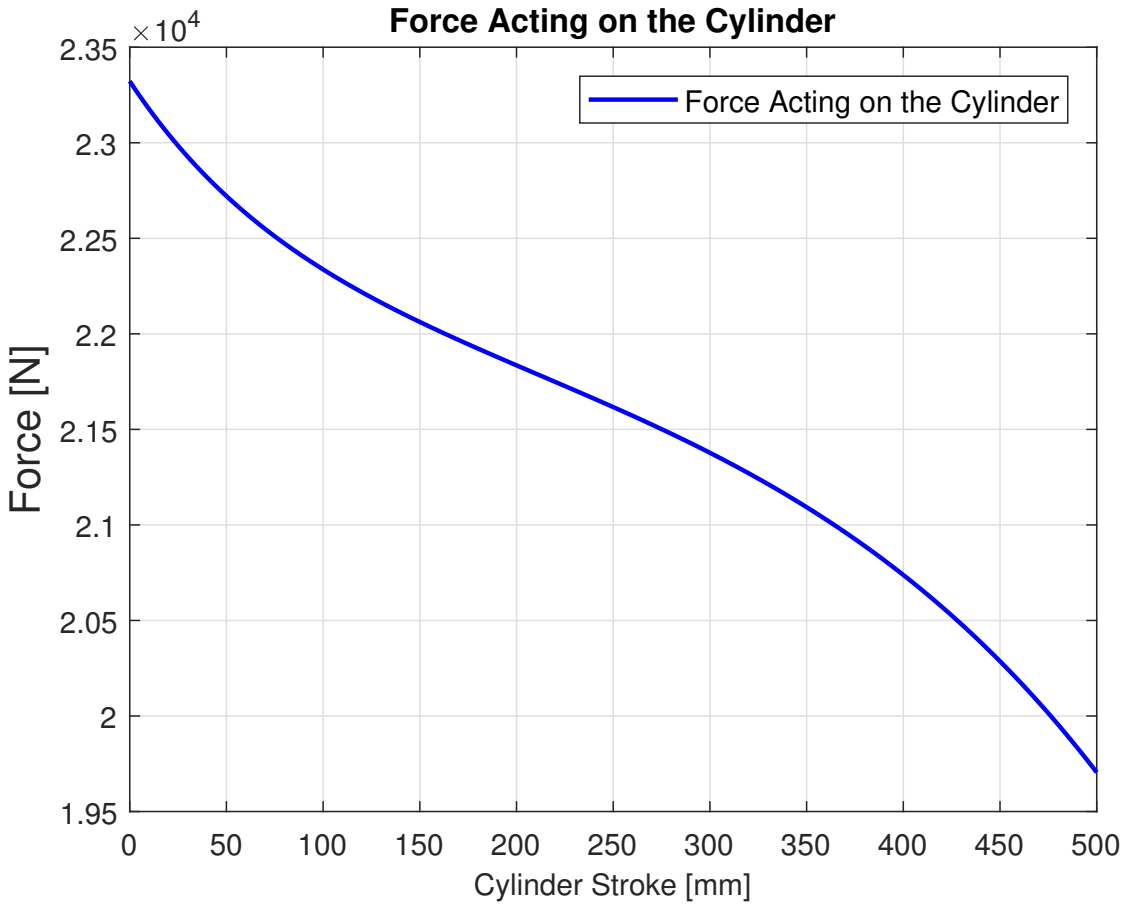

Figure 5.3: Force acting on the cylinder.

5.3 Evaluation of Equivalent Mass

For evaluation of the equivalent mass applied to the cylinder, equation 5.23 and 5.24 is used [22, p. 459-462], expressing the kinetic energy of a translational rigid body and fixed rotational body respectively. The two equations should be combined and then solved for the equivalent mass. For this task expressions for cylinder velocity and angular velocity of the beam and load are needed. This is derived in equations 5.23 and 5.23,

$$E_{kin,trans} = \frac{1}{2} m_{eq} v_e^2 \tag{5.23}$$

$$E_{kin,rot} = \frac{1}{2} I_{tot} \dot{\theta_e}^2 \tag{5.24}$$

where:	$E_{kin,trans}$	Translational kinetic energy
	$E_{kin,rot}$	Rotational kinetic energy
	m_{eq}	Equivalent mass
	I_{tot}	Total moment of inertia
	v_e	Translational velocity
	θ_e	Angular velocity

From figure 5.2 and equation 5.10 and 5.11, L_{ab} and L_{ac} respectively are given. Applying them into the law of Cosine gives an expression for L_{bc}

$$L_{bc}^2 = L_{ab}^2 + L_{ac}^2 - 2 \cdot L_{ab} \cdot L_{ac} \cdot \cos\theta_6 \tag{5.25}$$

Differentiating the expression for L_{bc} will result in an expression for cylinder velocity $\dot{L}_{ab}$ and the angular velocity for $\dot{\theta}_6$, which will then be used for expressing the equivalent mass acting on the cylinder.

$$2\, L_{bc}\, \dot{L}_{bc} = -2 \cdot L_{ab} \cdot L_{ac} \cdot \dot{\theta}_6 \cdot \sin\theta_6 \tag{5.26}$$

Then solving for $\dot{\theta}_6$,

$$\dot{\theta}_6 = \frac{L_{bc} \cdot \dot{L}_{bc}}{L_{ab} \cdot L_{ac} \cdot \sin\theta_6} \tag{5.27}$$

To solve for m_{eq}, it is necessary to use the relation for kinetic energy shown in equation 5.23 and 5.24, and the moment of inertia for the beam and pay load from equation 5.7.

$$E_{kin} = \frac{1}{2} \cdot m_{eq} \cdot \dot{L}_{bc}^2 = \frac{1}{2} I_{tot} \cdot \dot{\theta}_6^2 \tag{5.28}$$

$$\frac{1}{2} \cdot m_{eq} \cdot \dot{L}_{bc}^2 = \frac{1}{2} I_{tot} \cdot \left(\frac{L_{bc} \cdot \dot{L}_{bc}}{L_{ab} \cdot L_{ac} \cdot \sin\theta_6} \right)^2 \tag{5.29}$$

$$m_{eq} = I_{tot} \cdot \left(\frac{L_{bc}}{L_{ab} \cdot L_{ac} \cdot \sin\theta_6} \right)^2 \tag{5.30}$$

where:	E_{kin}	Kinetic energy of the beam and load
	m_{eq}	Equivalent mass which the cylinder see
	$\dot{L}_{bc}$	Cylinder velocity
	I_{tot}	Mass moment of inertia for the beam and load
	$\dot{\theta}_6$	Angular velocity of the beam and load

The equivalent mass acting on the cylinder is shown in figure 5.4.

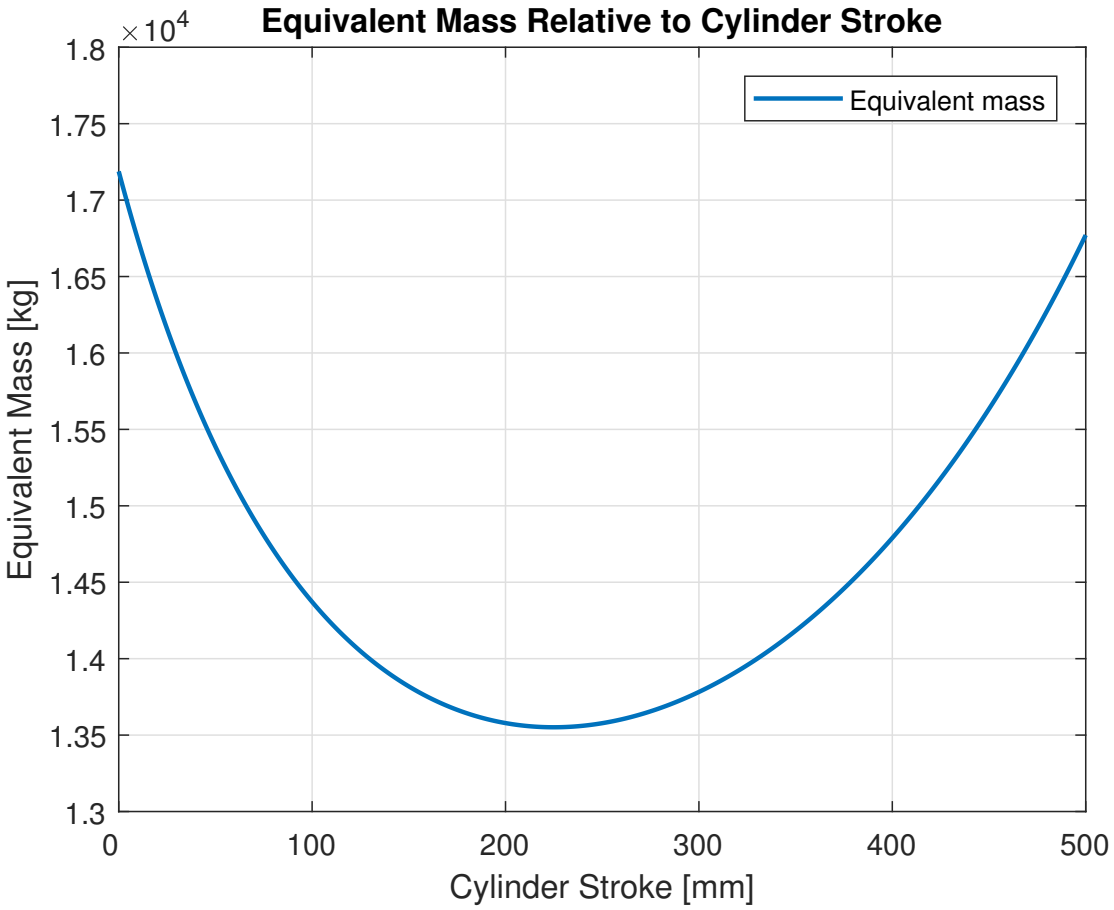

Figure 5.4: Equivalent mass acting on the cylinder.

5.4 Dynamic Model of the Mechanical system

The mechanical system is modelled by Sørensen and described in [23, pp.198-199]. The chosen method is the "Finite Segment Method" which is well tested and is a relatively simple way of modelling dynamic behaviour in flexible beam systems. The idea behind the method is to replace the beam with several smaller elements connected to each other.

5.4.1 A brief description of the model

A good desription of the oscillations was the key point of interest when carrying out this modelling. Due to this, the flexibility in longitudinal direction is neglected. The elements are connected with two torsional springs in series, a damper and a revolute joint. Spring stiffness, $k_{f,i}$, related to an element i is shown in equation 5.31, and the equivalent stiffness of the springs between two elements are given from equation 5.32. A rotational damper is used for accomodating the flexibility in the base and its value is tuned through experimental data. The payload is considered a rigid point mass.

$$k_{f,i} = \frac{2 \cdot E \cdot I_z}{L_{s,i}} \tag{5.31}$$

$$k_{eq,m,n} = \frac{k_m \cdot k_n}{k_m + k_n} \tag{5.32}$$

Where:	$k_{f,i}$	Spring stiffness
	E	The elasticy module of the material
	I_z	2^{nd} moment of inertia for the cross section of the prismatic beam
	$L_{s,i}$	Length of the element
	$k_{eq,m,n}$	Equivalent spring stiffness of two torsional springs in series
	k_m	Spring stiffness of the first spring in the series
	k_n	Spring stiffness of the second spring in the series, equal to k_m

The beam is modelled with four elements between the bearing and the cylinder, and five elements between the cylinder and the payload.

5.4.2 Experimental Validation of the Dynamic Model

Validation of the model by comparing it to experimental results is described in [23, pp.202-207]. The four parameters being evaluated are the general tendency of the curves, peak sizes, oscillation frequencies and steady-state values.

Comparing the results with regards to friction forces, there is a good correspondence between the model and the experimental results. From this, it is assumed that the modelling of the mechanical loads are a good approximation of the real system. Concerning the mechanical and hydraulic eigen frequencies, there are differences between the model and the experimental results, however, the deviation is within acceptable limits.

Chapter 6

Controlling

This chapter introduce the control strategies which will be tested experimentally on the test-bed. As basis for the controller-design, the S-curve motion profile is introduced, a frequency response analysis is carried out both on the test bed and in the mathematical model and two feed forward strategies are introduced.

6.1 Motion Profile

When the cylinder is to follow a predefined motion profile, care must be taken to ensure that velocity and acceleration are within the limits of the system. If the motion profile is chosen to be of the Sigmoid curve type it ensures that the motion profile is continuous and differentiable at all points. In figure 6.1 plots of position, velocity and acceleration is shown for a full stroke cylinder motion.

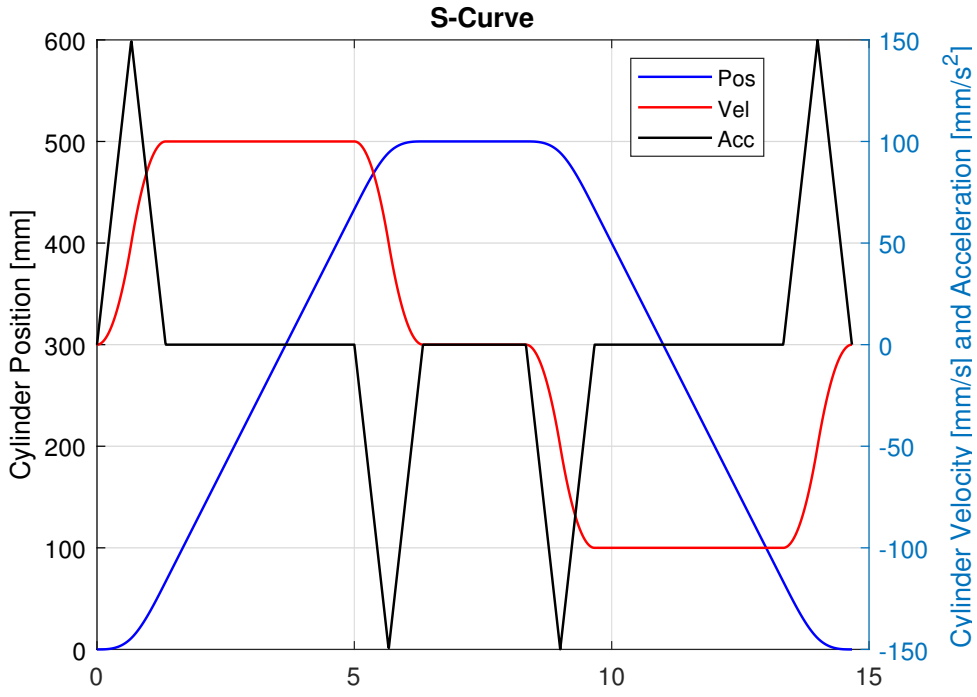

Figure 6.1: S-Curve

6.2 Frequency Response Analysis

Frequency response analysis can provide useful information about systems performance and for control design purposes [15, pp. 535-536]. This tool requires a linear system, however the electro hydraulic cylinder is non-linear because of friction in the cylinder and varying bulk modulus due to pressure and temperature changes. Nevertheless, this experiment was conducted both as a simulation and on the test bed with the assumption that non linearities would not affect the results significantly. The procedure is as follows: A stream of sine waves is generated, as input to the PMSM. The amplitude and frequency is chosen so maximum acceleration for the motor is never exceeded. Further on, care was taken to ensure that the cylinder would not reach the end stop during the low frequency range. The magnitude and phase shift are calculated according to equations 6.1 and 6.2,

$$M(\omega) = \frac{M_o(\omega)}{M_i(\omega)} \tag{6.1}$$

$$\phi(\omega) = \phi_o(\omega) - \phi_i(\omega) \tag{6.2}$$

Where:	$M(\omega)$	Magnitude frequency response
	$\phi(\omega)$	Phase frequency response
	$M_i(\omega)$	Amplitude of input
	$M_o(\omega)$	Amplitude of output
	$\phi_i(\omega)$	Phase of input
	$\phi_o(\omega)$	Phase of output
	ω	Frequency

By converting the Magnitude frequency response to decibels, where dB = 20 log M, it can be plotted versus log ω. The phase curve is plotted as phase angle versus log ω. The Bode plot for both the simulated experiment and the experiment performed on the test bed are shown in figure 6.2. The linearised model derived in section 6.3.1 is included in the Bode plot for comparison reasons.

The frequency response was one of the initial tests carried out on the test bed after the assembly. Performing this kind of test can introduce severe oscillation in the crane boom, and possible damage hydraulic parts or mechanical equipment. In the effort of not unintentionally do any harm, only a limited amount of frequencies in the area where the phase drops fast was tested.

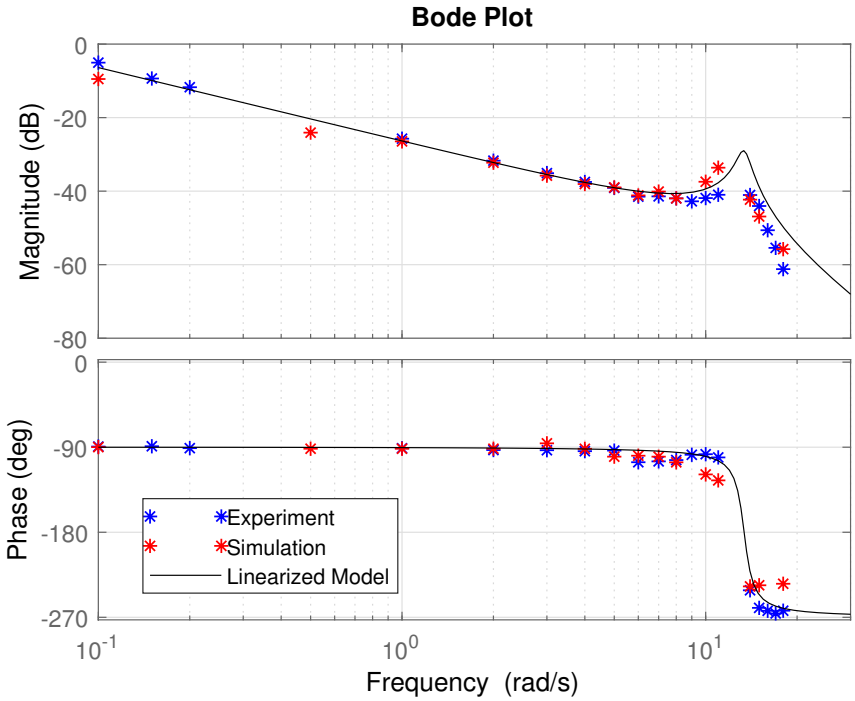

Figure 6.2: Bode Plot, frequency response test

6.3 Feed forward control

It is possible to implement known disturbances into the controller structure as a feedforward signal. For feed forward control, two strategies will be discussed; the inverse plant transfer function and the predicted angular velocity input to the motor calculated from the motion profile.

6.3.1 Inverse Plant Transfer Function

This strategy requires a good mathematical model of the plant, which is difficult to determine due to non-linearities in the hydraulic and mechanical system. To obtain a transfer function the system must be linearised which mean that several simplifications must be done. This is carried out in the next section, resulting in a linear model which is compared with the non-linear model.

The linearisation approach described in this section has been successfully used in the past by Busquets and Ivantysynova [18, pp.327-329].

Non-linear Model

The non-linear model is derived from section 3.1.7, and for the purpose of linearisation it is further simplified compared to the Simulink model also referred to as the high fidelity model.

The dynamics of the linear actuator can be described by equation 3.13 from subsection 3.1.5.

$$m_{eq}\ddot{x}_c = p_p A_p - p_r A_r - F_f - F_{ext} \tag{6.3}$$

Where:	m_{eq}	Equivalent mass
	x_c	Cylinder position
	p_p	Pressure on piston side, pressure node 1
	p_r	Pressure on rod side, pressure node 2
	A_p	Area piston side
	A_r	Area rod side
	F_f	Friction forces
	F_{ext}	External forces

Where the external forces, F_{ext}, expressed by the equivalent mass 5.30 contains the trigonometric sine term, and the friction forces, F_f, equation 3.12 contains the trigonometric tangent hyperbolic function and an exponential function. Trigonometric functions and exponential functions are non-linear.

For simplification reasons, pressure nodes 6 and 7 are neglected and p_5 is considered constant due to the large ratio between total volume of the accumulator and fluid volume. The other four pressure nodes are expressed through equations 6.4 to 6.7 and shown in figure 3.4.

$$\dot{p}_1 = \frac{\beta}{V_1}\left(-Q_{POCV1} + \omega_m D_p \eta_v\right) \tag{6.4}$$

$$\dot{p}_2 = \frac{\beta}{V_2}\left(-Q_{POCV2} + Q_{CV2} - Q_{CV1} - \omega_m D_p \eta_v\right) \tag{6.5}$$

$$\dot{p}_3 = \frac{\beta}{V_3 + V_c(x_c)}\left(Q_{POCV1} - A_p \dot{x}_c\right) \tag{6.6}$$

$$\dot{p}_4 = \frac{\beta}{V_4 + V_c(0.5 - x_c)}\left(Q_{POCV2} + A_r \dot{x}_c\right) \tag{6.7}$$

Where:	β	Bulk modulus
	V_1	Volume of chamber one including lines and cylinder volume $V(x_c)$
	ω_m	Angular motor speed
	$Q_{POCV1-2}$	Flow through the pilot operated check valve$POCV1-2$
	Q_{CV1-2}	Flow through check valve $CV1-2$
	$V_i(1 \leq i \leq 4)$	Volume of hoses and lines pressure node 1-4
	$V_c(x_c)$	Cylinder volume as function of piston position x_c
	D_p	Pump displacement
	η_v	Approximated constant volumetric efficiency of pump
	A_p	Area piston side
	A_r	Area rod side

Flow through the different valves are defined through equations 6.8 to 6.11.

$$Q_{POCV1} = \left(\alpha_D \, \pi \, d_{po} \tanh(p_1 - p_3) \sqrt{\frac{2}{\rho}|p_1 - p_3|}\right) y_1 \tag{6.8}$$

$$Q_{POCV2} = \left(\alpha_D \, \pi \, d_{po} \tanh(p_2 - p_4) \sqrt{\frac{2}{\rho}|p_2 - p_4|}\right) y_2 \tag{6.9}$$

$$Q_{CV1} = \left(\alpha_D \, \pi \, d_{cv} \tanh(p_2 - p_5) \sqrt{\frac{2}{\rho}|p_2 - p_5|}\right) y_{CV1} \tag{6.10}$$

$$Q_{CV2} = \left(\alpha_D \, \pi \, d_{cv} \tanh(p_5 - p_2) \sqrt{\frac{2}{\rho}|p_5 - p_2|}\right) y_{CV2} \tag{6.11}$$

Where:	$Q_{POCV1-2}$	Flow through the pilot operated check valve$POCV1-2$
	Q_{CV1-2}	Flow through check valve $CV1-2$
	α_D	Discharge coefficient
	d_{po}	Pilot operated check valve poppet diameter
	$p_i (1 \leq i \leq 5)$	Pressure in chamber 1-5
	ρ	Density of hydraulic fluid
	d_{cv}	Check valve poppet diameter
	$y_i (1 \leq i \leq 2)$	Pilot operated check valve poppet displacement for valve POCV1 and POCV2
	$y_{CVi} (1 \leq i \leq 2)$	Check valve poppet displacement for valve CV1 and CV2

The dynamics of the valve spools are considered fast enough to be neglected. The electric motor dynamics can for simplicity be expressed by a first order system, equation 6.12.

$$\dot{\omega}_m = \frac{1}{\tau_m}\omega_m + \frac{K_m}{\tau_m}u_m \tag{6.12}$$

Where:	ω_m	Angular motor speed
	τ_m	Time constant of the motor dynamics
	K_m	Motor dynamic gain
	u_m	The normalized unit velocity command

From these derivations the state space representation for $\mathbf{x_s} = [x_c \, , \dot{x}_c, \, p_1, \, p_2, \, p_3, \, p_4, \, \omega_m]^T$ are shown in

equation 6.13.

$$
\begin{aligned}
\dot{x}_{1,s} &= x_{2,s} \\
\dot{x}_{2,s} &= \frac{1}{m_{eq}} \left(A_p x_{5,s} - A_r x_{6,s} - F_f - m_{eq} g \right) \\
\dot{x}_{3,s} &= \frac{\beta}{V_1} \left(-Q_{POCV1} + V_p \eta_v x_{7,s} \right) \\
\dot{x}_{4,s} &= \frac{\beta}{V_2} \left(-Q_{POCV2} + Q_{CV2} - Q_{CV1} - V_p \eta_v x_{7,s} \right) \\
\dot{x}_{5,s} &= \frac{\beta}{V_3 + V_c(x_{1,s})} \left(Q_{POCV1} - A_p x_{2,s} \right) \\
\dot{x}_{6,s} &= \frac{\beta}{V_4 + V_c(0.5 - x_{1,s})} \left(Q_{POCV2} + A_r x_{2,s} \right) \\
\dot{x}_{7,s} &= \frac{1}{\tau_m} x_{7,s} + \frac{K_m}{\tau_m} u_m
\end{aligned}
\tag{6.13}
$$

Where: $x_{i,s} (1 \leq i \leq 7)$ State variables in the state space representation of the model

Linear Model

For the synthesis of a linear controller, one of the approaches in this study is from the single-input and single-output (SISO) model derived from equation 6.13. A simple linearisation of the equivalent mass term is not possible because it contains the trigonometric sine term. Likewise for the friction force term, which contain the trigonometric tangent hyperbolic function and an exponential function. In order to proceed with a linear control design, these two terms must be neglected. Then, the friction term and load term are treated as load disturbances. For the purpose of simplification, the motor dynamics have also been neglected. The dynamics of the pilot operated check valves are neglected due to simplicity and p_2 is equal to p_5 and equal to p_{lp} considered a constant, resulting in number of pressure nodes being reduced from four to one. The linearisation is made at a specific cylinder position of a stroke length equal to 0.25 meters, resulting in constant cylinder volume according to equation 6.14. Expression for the new capacitance of the pressure node are shown in equation 6.15. The remaining pressure node, shown in figure 6.3, are modelled in the linearised model. Finally, the bulk modulus are considered as constants. The parameters are shown in table 6.1.

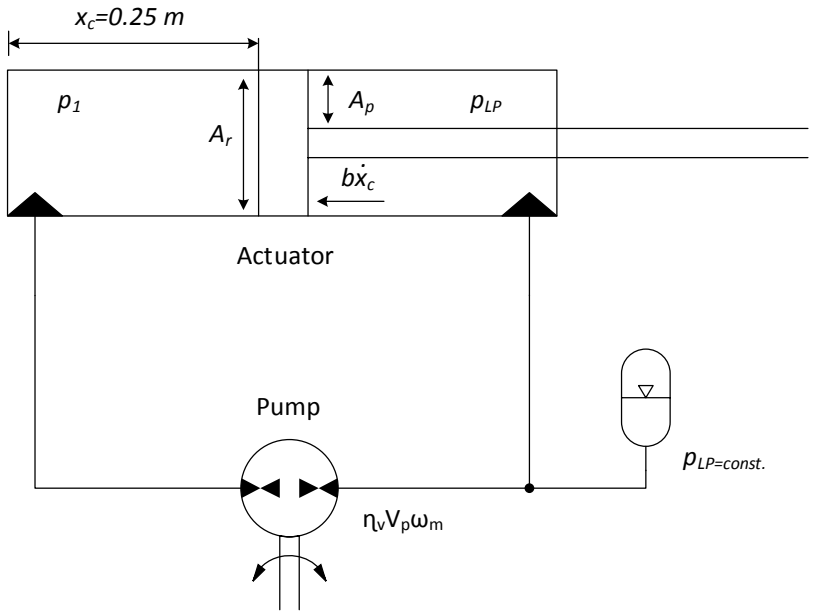

Figure 6.3: Reduced model for linearisation

Table 6.1: Constant used in the linearised model

Parameter	**Value**	**Unit**
Cylinder stroke, x_{cl}	0.25	[m]
Equivalent mass, $m_{eq,l}$	$1.48 \cdot 10^4$	[kg]
System damping, b_l	20000	[Ns/m]
Leakage coefficient due to pressure $k_{L,1}$	0	[m^3/Pa]
Leakage coefficient due to piston velocity $k_{L,2}$	0	[m^3s/m]
Volumetric efficiency of the pump η_v	0.9	[-]

The volume of pressure node 1 then becomes,

$$V_{1,l} = V_l + A_p \cdot 0.25 \text{ m} \tag{6.14}$$

Then the cylinder volume and bulk modulus are set at constant values and can be replaced by a capacitance, Ch_l, for the entire volume.

$$Ch_l = \frac{V_{1,l}}{\beta} \tag{6.15}$$

The linearised model is expressed by the state variables $\boldsymbol{x}_{sl} = [\dot{x}_c, p_1]^T$ which yields for equation 6.16 through 6.17

$$\dot{x}_{1,sl} = \frac{1}{m_{eq,l}} \left(x_{2,sl} A_p - b_l x_{1,sl} \right) \tag{6.16}$$

$$\dot{x}_{2,sl} = \frac{1}{Ch_l} \left(\omega_m D_p \eta_{vl} - A_p x_{1,sl} - K_{L1} x_{2,sl} - K_{L2} x_{1,sl} \right) \tag{6.17}$$

Where:	$\dot{x}_{1,sl}$	Cylinder velocity state variable
	$\dot{x}_{2,sl}$	Pressure one state variable
	$m_{eq,l}$	Equivalent mass, invariable
	A_p	Piston side area
	b_l	Viscous friction coefficient linearised model
	Ch_l	Capacitance of pressure build up volume one
	β	Bulk modulus oil
	ω_m	Motor angular velocity
	D_p	Pump volumetric displacement
	η_v	Volumetric efficiency pump
	K_{L1}	Leakage coefficient due to pressure
	K_{L2}	Leakage coefficient due to piston velocity
	V_l	Volume of lines linearised model
	$V_{1,l}$	Fixed volume of pressure node linearised model

For the continuous time invariant state space representation, equation 6.18 and 6.19, the matrices representing the model are shown in equation 6.20.

$$\dot{\boldsymbol{x}}(t) = A_l x(t) + B_l u(t) \tag{6.18}$$
$$\dot{\boldsymbol{y}}(t) = C_l x(t) + D_l u(t) \tag{6.19}$$

$$A_l = \begin{bmatrix} -\frac{B}{m_{eq,l}} & \frac{A_p}{m_{eq,l}} \\ -\frac{A_p}{Ch_1} & 0 \end{bmatrix},\ B_{l,hoi} = \begin{bmatrix} 0 \\ \frac{1}{Ch_l}(D_p\eta_v) \end{bmatrix},\ C_l = \begin{bmatrix} 1 & 0 \end{bmatrix},\ D_l = 0 \tag{6.20}$$

For the lowering mode, the efficiency of the pump should be divided by the input angular velocity, resulting in the output matrix B_{low} shown in equation 6.21. Hence two models should be used; one for hoisting and one for lowering.

$$B_{l,low} = \begin{bmatrix} 0 \\ \frac{D_p}{Ch_l\eta_v} \end{bmatrix} \tag{6.21}$$

Validation of Linearised Model

Validation of the model is done by a velocity step command to open loop system according to figure 6.4. From this, the position, velocity and pressure signal is shown in figure 6.5 and 6.6. The fluid pressure in the linearised model is given an initial pressure equal to the initial pressure in the high fidelity model.

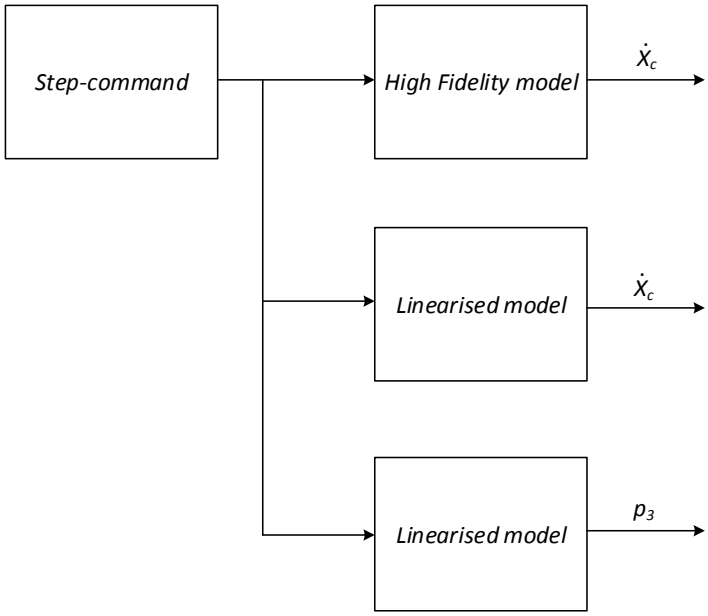

Figure 6.4: Block chart of the model validation program.

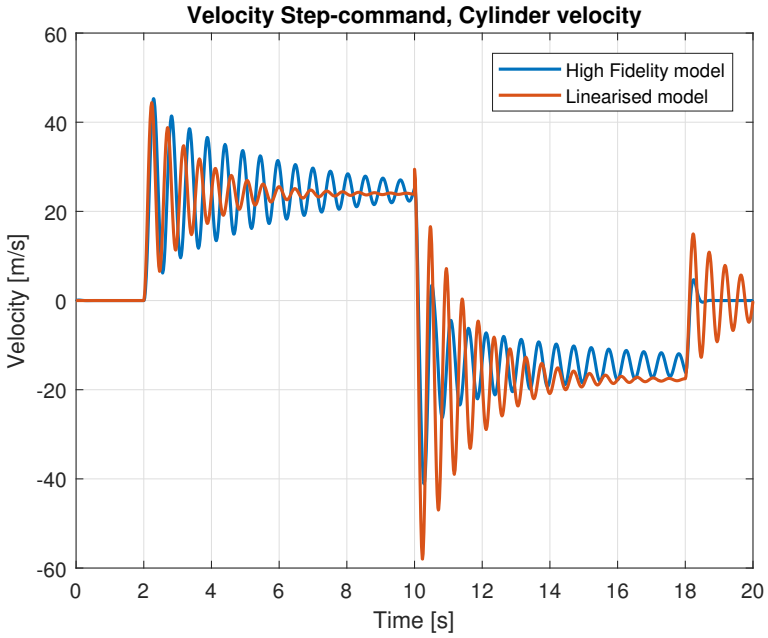

Figure 6.5: Velocity response for linearised model and high fidelity model.

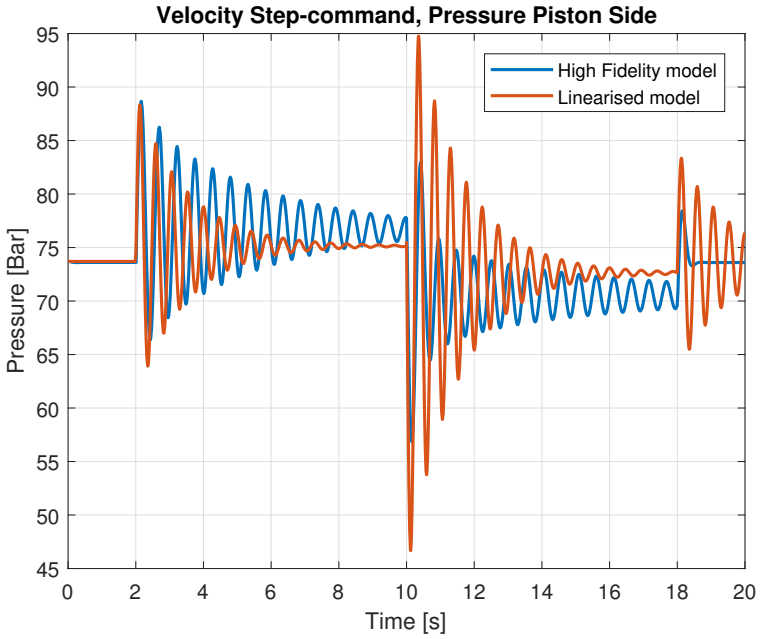

Figure 6.6: Pressure response for linearised model and high fidelity model.

The efficiency of the pump is an uncertain parameter which can influence the result as well as the uncertainty regarding the damping of the system.

Transfer Function of Linearised Model

Figure 6.7 shows the uncompensated bode plot of the system.

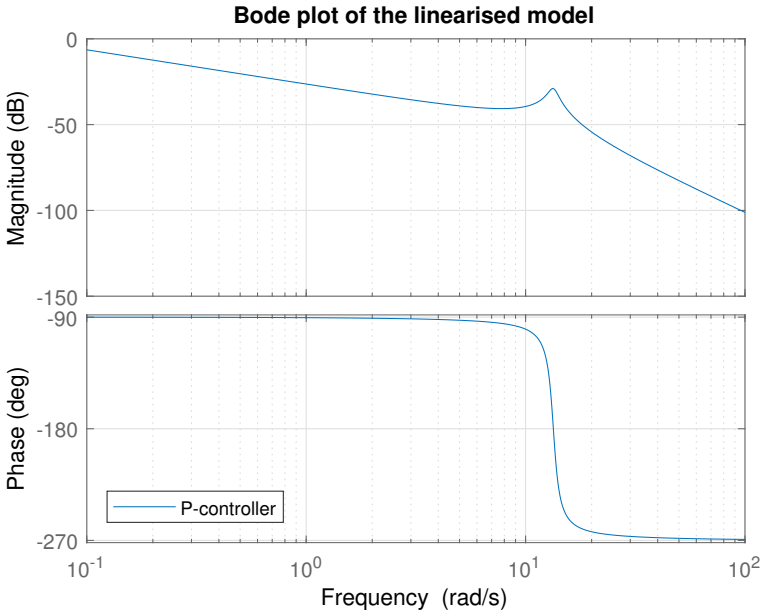

Figure 6.7: Uncompensated bode plot from input pump angular velocity to output cylinder velocity.

The transfer function of the system are shown in equation 6.22, obtained by use of MATLAB.

$$G_{plant}(s) = \frac{8.584}{s^2 + 1.351s + 179.1} \tag{6.22}$$

which has two complex poles at,

$$-0.6757 + j13.3674 \tag{6.23}$$
$$-0.6757 - j13.3674 \tag{6.24}$$

The magnitude peak and phase drop at the poles at 13.4 rad/s is dependent on the damping of the system. The height of the peak are uncertain due to the unpleasant performance of the test bed when carrying out an experimental frequency response test at this frequency.

Inverse Plant Transfer Function

To invert the plant transfer function shown in equation 6.22, zeroes must be added to make the inverse transfer function proper, i.e. higher order of numerator than denominator. If the zeroes are far from the dominant poles, their influence on the system is insignificant [16]. Three zeroes at s=-100 rad/s are added to the plant transfer function in equation 6.25

$$G_{plant}(s) = \frac{8.584 \cdot (\frac{1}{100}s + 1)^3}{s^2 + 1.351s + 179.1} \tag{6.25}$$

This results in the proper inverse plant transfer function, shown in equation 6.26, calculated with the help of MATLAB.

$$G^{-1}_{plant}(s) = \frac{s^2 + 1.351s + 179.1}{8.584 \cdot 10^{-6}s^3 + 0.002575s^2 + 0.2575s + 8.584} \tag{6.26}$$

This inverted transfer function of the plant can be used as a feed forward function. As the model of the plant is simplified, there should be an additional controller to correct for the error.

6.3.2 Alternative Solution, Predicted Motor Velocity

When there is a predefined motion profile for the cylinder, then the velocity profile is known as the derivative of the position. Selecting the appropriate gain, and feeding the gained velocity signal into the system after the controller, will improve performance as the disturbance is corrected before the controller detects the error. In this way, the feed forward compensates the long term disturbances and the controller handles the short term disturbances.

Calculating the appropriate gain: The velocity of the cylinder depends on the rotational velocity of the pump, then by equation 6.27 and 6.28 the resulting gain is as shown in equation 6.29:

$$Q_c = A_c \cdot \dot{x}_c \tag{6.27}$$
$$Q_p = D_p \cdot n \tag{6.28}$$

$$G_{ff} = \frac{60 \cdot D_p}{A_c} \tag{6.29}$$

Where:	Q_c	Flow into the cylinder
	A_c	Area of piston in cylinder
	$\dot{x}_c$	Piston velocity
	Q_p	Flow out of the pump
	D_p	Displacement of the pump
	n	Rotational velocity of the pump
	G_{ff}	Feedforward gain

The volumetric efficiency of the pump can be implemented in the feedforward for better performance. The efficiency is dependent on pressure drop over the pump, rotational speed and whether the pump acts as a pump or a motor. The latter depends on the direction of the load. In section 3.1.6 a pump loss model is described, and thereby an estimate of the volumetric efficiency available.

A more simplistic method is to estimate the volumetric efficiency as a constant parameter. There are some issues determining the value, as no information is presented in the data sheet of the pump.

In figure 6.8 there are shown three plots from simulation: the cylinder position reference, the position error with only the feedforward gain and the position error for feedforward gain including the loss model.

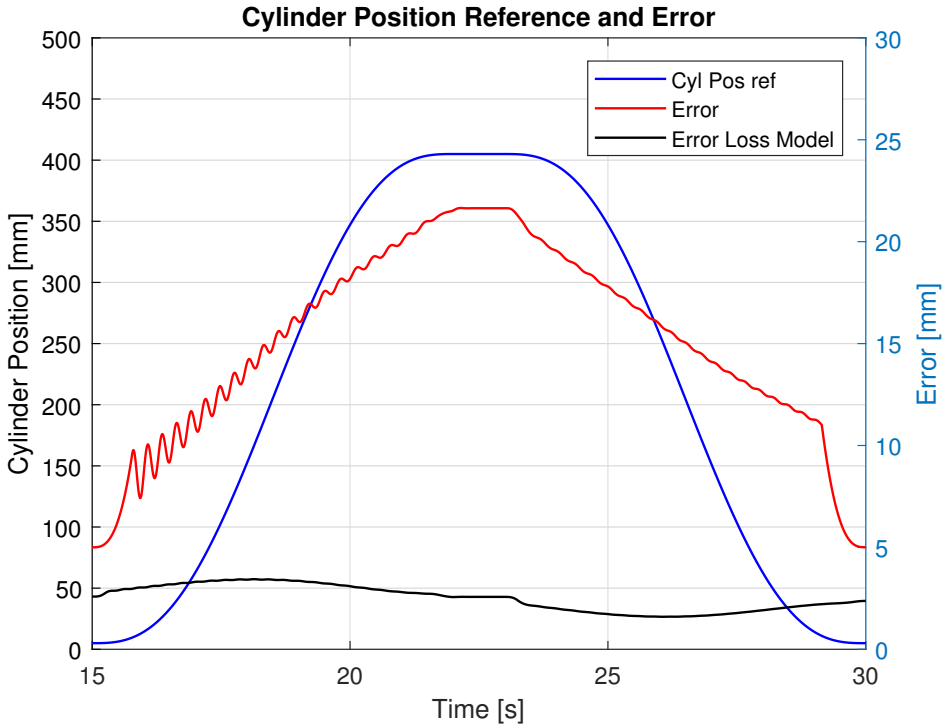

Figure 6.8: Feedforward error

6.3.3 Design of a Lag Controller for Increased Stability

Design of the lag controller is based on the dynamics of the linearised model. This due to that the frequency analysis carried out on both the test bed and the linear model coincides well, shown in figure 6.2.

Running tests on the test bed before implementing a lag controller show that a proportional gain of 10 gave stable results. Implementing a lag controller should provide increased stability. Based on a unit ramp and an

error steady state of one centimetre, the parameters listed in table 6.2 are used for the controller design. The gain margin of 20 dB is set abundantly high due to the uncertainty of the magnitude at the pole frequency.

Table 6.2: System parameters for lag design

Parameter	**Value**
System type	1
Ramp input	$v_{ramp} = 1$
Error steady state	$e_{ss} = 0.01$
Phase margin	$\phi_M = 55$
Gain margin at the poles	$G_{ma} = 20$ dB

$$e_{ss} = \frac{v_{ramp}}{k_{sys} \cdot k_{ess}} \tag{6.30}$$

From equation 6.22 the system gain, k_{sys}, is 8.584.

$$k_{ess} = \frac{v_{ramp}}{k_{sys} \cdot e_{ss}} \text{ from [24, p.23]} \tag{6.31}$$

$$= \frac{1}{8.584 \cdot 0.01} \tag{6.32}$$

$$= 11.65 \tag{6.33}$$

Where:
- e_{ss} Error steady state
- v_{ramp} Slope of the ramp
- K_{sys} System gain
- k_{ess} Proportional gain to satisfy the steady state requirement

The calculated gain is close to the experimental proportional gain results and the following lag controller calculation is based on $k_{ess} = 11.65$.

The bode plot in figure 6.9 shows a plot with a proportional controlled system for increasing bandwidth. The gain margin at the pole-frequency is -7.66 dB. For stability purposes, the gain margin should be increased especially regarding the uncertainty concerning the height of the peak. Implementing a lag-compensator will result in an increased gain margin at the poles as well as retain the gain at lower frequencies. The gain, k_{ess}, used for increasing bandwidth is given in equation 6.34 and determined by discretion.

$$k_p = 11.65 \tag{6.34}$$

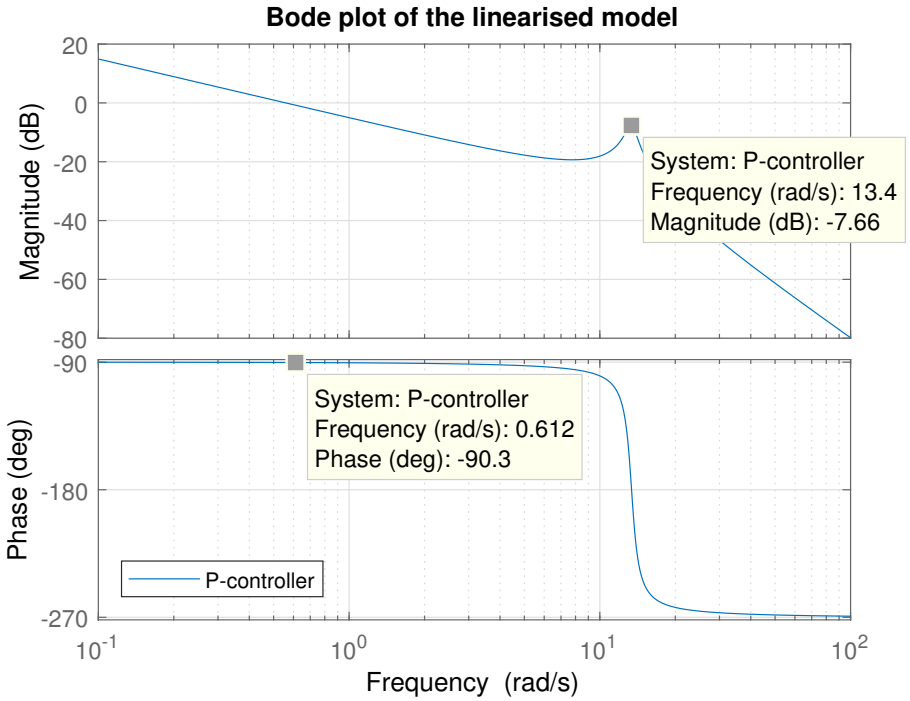

Figure 6.9: Bode plot of transfer function from motor input [RPM] to cylinder position [mm].

Design of a Lag Controller

The purpose of implementing a lag controller in this particular case is to decrease the magnitude at the complex poles. The structure of the controller is shown in equation 6.35 which is the lag-part from equation 2.16. The method used is from [16, p.L11a:97].

$$G_{c,Lag}(s) = \frac{1}{\alpha}\frac{1+\frac{1}{T_2}}{s+\frac{1}{\alpha T_2}} \tag{6.35}$$

Where,

$$\frac{1}{T_2} = \frac{\omega_{1,L}}{10} \tag{6.36}$$

$$\alpha = 10^{\frac{K_{adj}}{20}} \tag{6.37}$$

Starting by determining frequency where to reduce the gain, $\omega_{1,L}$, which in this case is at the pole-frequency. The gain margin should be decreased 12 dB according to table 6.2.

$$\omega_{1,L} = 13.4 \text{ rad/s} \tag{6.38}$$

$$K_{adj} = 12 \text{ dB} \tag{6.39}$$

Then $\frac{1}{T_2}$, according to equation 6.36, is located a decade below ω_1:

$$\frac{1}{T_2} = \frac{\omega_{1,L}}{10} \tag{6.40}$$

$$= \frac{13.4 \text{ rad/s}}{10} \tag{6.41}$$

$$= 1.34 \text{ rad/s} \tag{6.42}$$

The time constant, T_2, is given by equation 6.43,

$$T_2 = \frac{1}{1.34 \text{ rad/s}} \tag{6.43}$$

$$= 0.746 \text{ s} \tag{6.44}$$

The value of the desired gain reduction, α, from equation 6.37 is determined in equation 6.45:

$$\alpha = 10^{\frac{K_{adj}}{20}} \tag{6.45}$$

$$= 10^{\frac{12}{20}} \tag{6.46}$$

$$= 3.98 \tag{6.47}$$

The calculated Lag-controller is shown in equation 6.48.

$$G_{c,Lag}(s) = \frac{1}{3.98} \frac{s + \frac{1}{0.746}}{s + \frac{1}{2.97}} \tag{6.48}$$

Figure 6.10 shows the bode plot of the system when implementing a Lag-controller. The gain margin at the poles is increased as well as the cross frequency only slightly decreased compared to the P-controlled plant. Even though the lag controller resulted in a drop in the phase margin, the phase margin at the cross frequency is still satisfying.

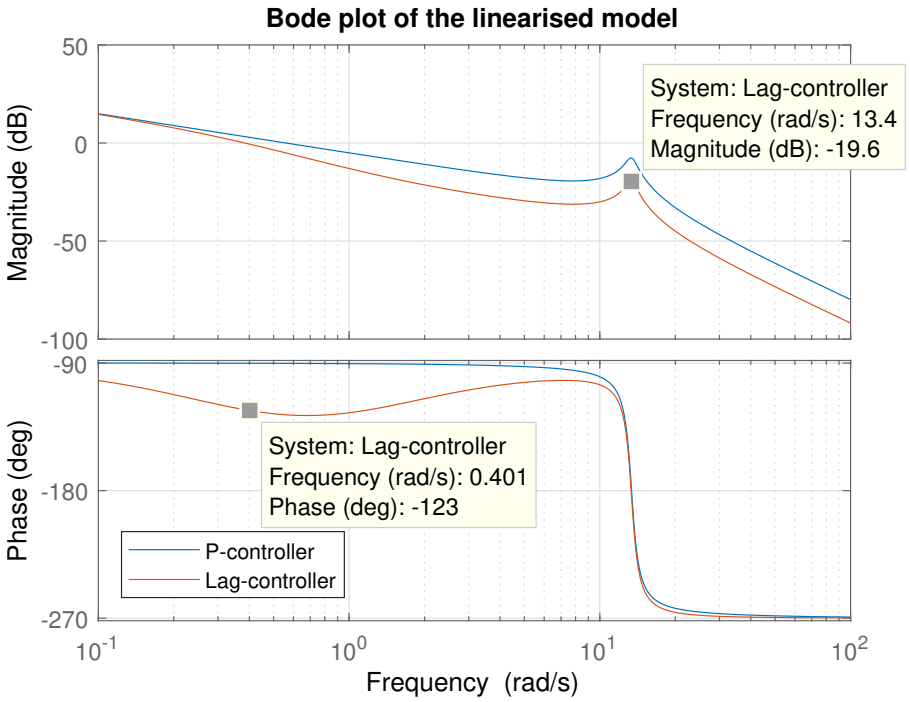

Figure 6.10: Bode plot of transfer function from motor input [RPM] to cylinder position [mm].

Where:

$G_{c,Lag}$	Transfer function of Lag controller
α	Value of the gain reduction
s	Variable in frequency domain
T_2	Time constant of the lag controller
$\omega_{1,L}$	The frequency where the gain should be decreased
K_{adj}	The gain reduction in dB

6.4 Control Algorithms for Testing

Two control algorithms will be tested, the PI-controller based on a lag-controller from the linearised model and the alternative feed forward controller based on the predicted cylinder velocity.

6.4.1 Lag Controller Converted to PI Controller

The Lag-compensator is converted to a PI-controller, given in equation 6.49, for control of the test bed.

$$\begin{aligned} k_{ess} = k_p &= 11.65 \\ k_{i,L} &= \frac{1}{T_2} \\ &= \frac{1}{0.746 \text{ s}} \\ k_{i,L} &= 1.34/ \text{ s} \end{aligned} \tag{6.49}$$

Where:

k_p	Proportional gain of the controller
$k_{i,L}$	Integral gain of the controller

6.4.2 Feed Forward

The feed forward algorithm concerning the predicted cylinder velocity from equation 6.29 will be implemented in the controller of the test bed. Unfortunately, the inverse plant feed forward model will not be tested.

Chapter 7

Results and Model Validation

In the following section results from the experimental work is presented and the simulation model is evaluated.

7.1 Motion Cycle Performance

For evaluating the performance of the system, two different motion profiles are evaluated. The first is a cycle consisting of a hold-hoist-hold-lower-hold motion. Three different combinations of velocity and acceleration were tested. The second cycle is a sinusoidal motion. Finally, results from test number 1 are compared with the performance of the high fidelity model.

All tests were conducted with the same feedback controller and feed forward gain. It is implemented a P-controller with $k_p = 10$ without any integral or derivative part, the feed forward gain is constant.

The controller is turned off when the position error for the cylinder is less than ± 2 mm, using the feed forward signal as input to the motor during this period. The reason for doing this is because of how the passive load holding functionality is implemented.

7.1.1 Test number 1

In table 7.1 the parameters for test number 1 are given, passive load holding is not activated.

Table 7.1: Test Parameters

Parameter	**Value**	**Unit**
Start position	10	[mm]
Initial hold time	10	[s]
Travel distance	400	[mm]
Velocity	50	[mm/s]
Acceleration	50	[mm/s^2]
Hold time	20	[s]
Return position	10	[mm]
k_p	10	
Controller turned off at	± 2	[mm]
Maximum flow through POCV1	± 10	[l/min]
Maximum motor velocity	± 1000	[RPM]

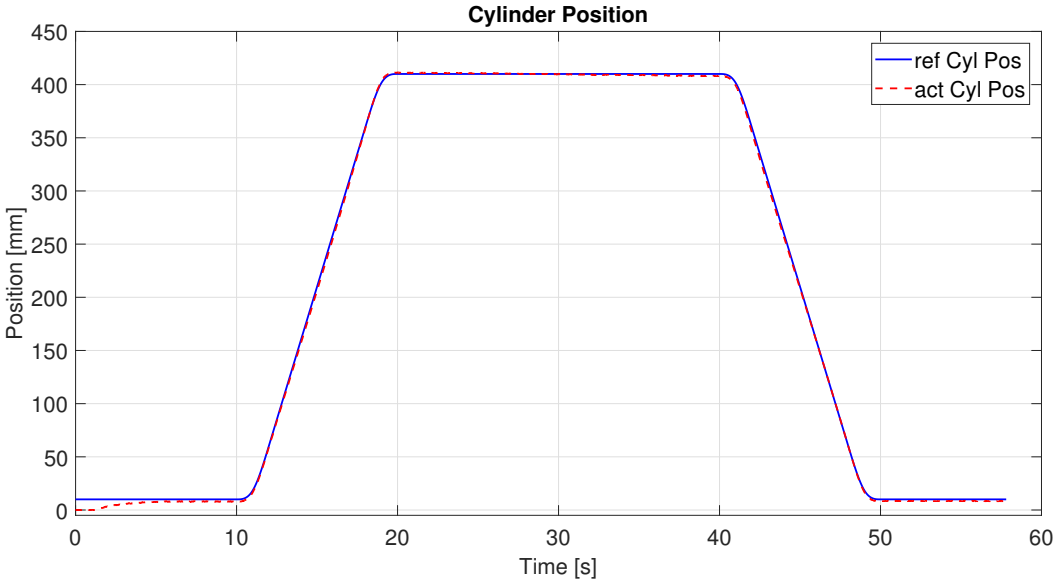

Figure 7.1: Cylinder Position

Figure 7.1 shows that the cylinder is capable of following a predefined motion profile, the accuracy is shown in figure 7.2 as the cylinder position error.

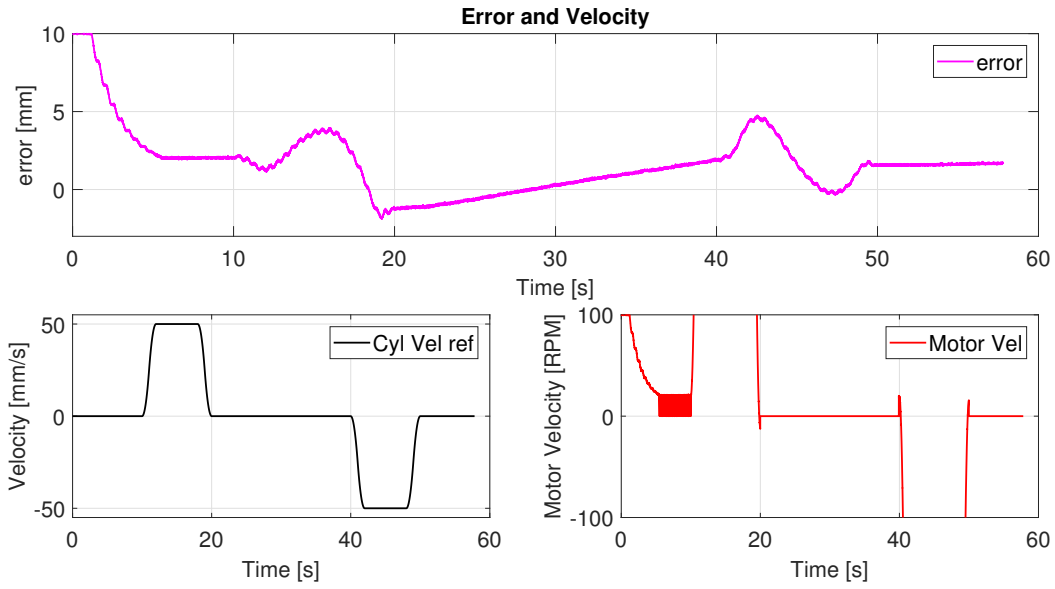

Figure 7.2: Error and Velocity

Figure 7.2 shows that due to leakage in the pump, the system is not capable of holding the load at rest, during the period from $20 - 40$ s the cylinder is contracted by approximately 3 mm with the motor shut off. Since the error is within mentioned hysteresis, the motor is shut off by the feed forward signal being zero according to the velocity reference signal.

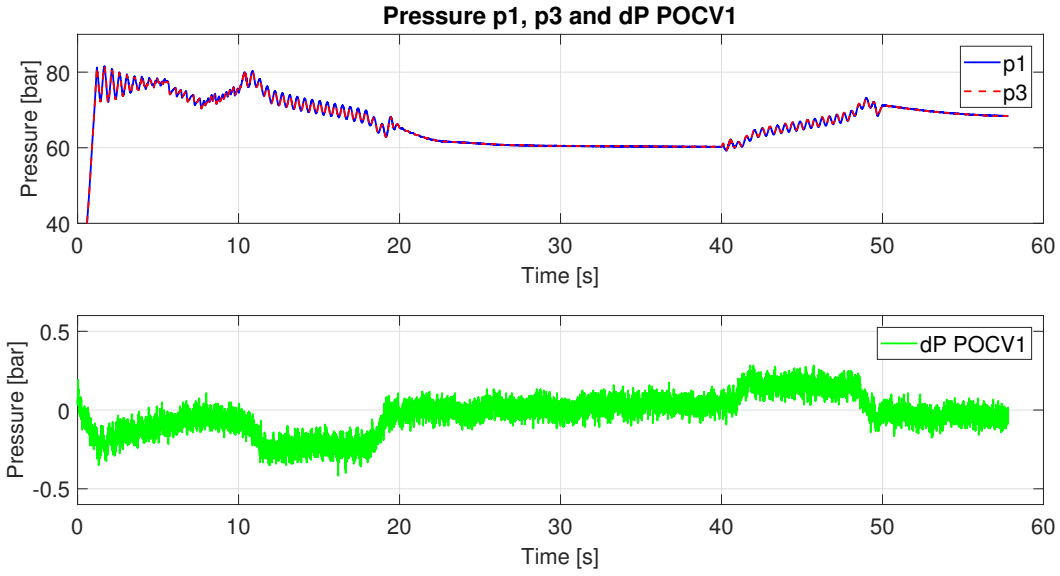

Figure 7.3: Pressure p1, p3 and dP over POCV1

Figure 7.3 shows pressure on both sides of POCV1 as p1 and p3, and then giving dP. Pressure drop over POCV1 is low, in the range of $0.1 - 0.2$ bar, this was not expected. Expected dP when hoisting the load was approximately 7 bar due to the crack pressure settings of POCV1. When lowering the load the pilot pressure should partially open the poppet. The behaviour of the poppet in the POCV is described in section 2.2.4 and 3.1.1.

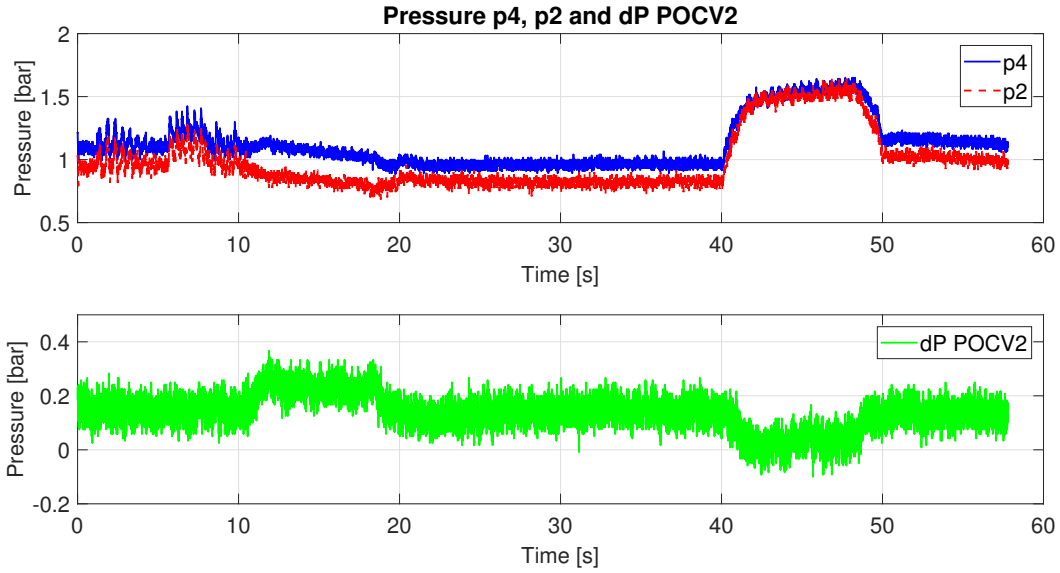

Figure 7.4: Pressure p2, p4 and dP over POCV2

Figure 7.4 show the pressures p4 and p2 and dP over POCV2. Pressure drop over POCV2 is low, in the range of $0.1 - 0.2$ bar, as expected, indicating that the poppet in the valve is opened by the pilot pressure. The plot can indicate an issue with the calibration of the pressure sensors, the expected result should vary around zero, and not 0.15 bar. The sensors in this part of the circuit have measuring range $0 - 250$ bar, so some deviation measuring this low pressures can be expected.

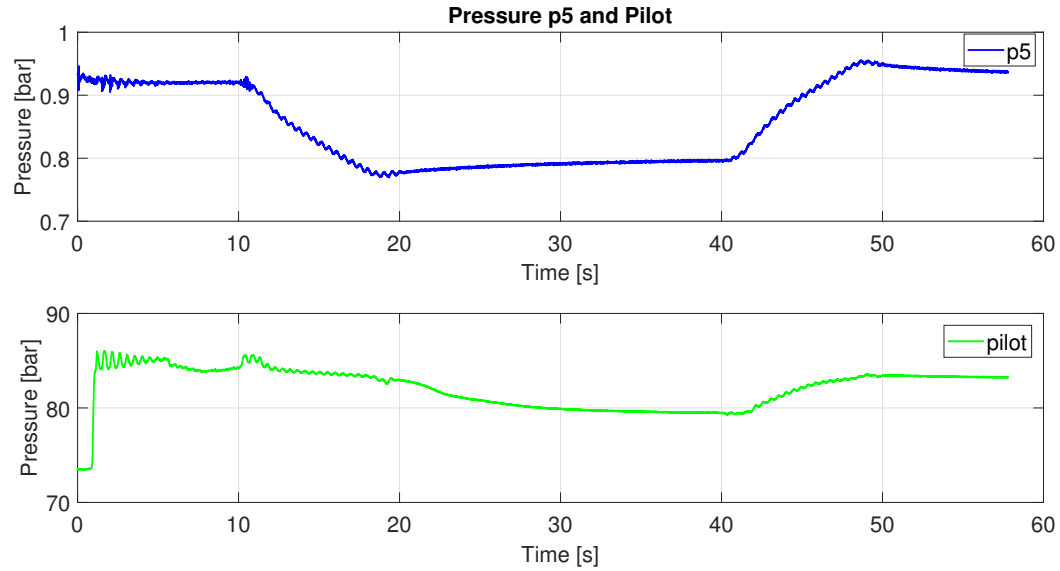

Figure 7.5: Pilot pressure and p5

Pilot pressure and p5 as the accumulator pressure, are shown in figure 7.5. Accumulator pressure is a function of cylinder stroke and is expected to be nearly constant. Pilot pressure is kept high for not activating the passive load holding functionality.

7.1.2 Test number 2

In table 7.2 the test parameters for test number 2 are given, passive load holding is not activated.

Table 7.2: Test Parameters

Parameter	**Value**	**Unit**
Start position	10	[mm]
Initial hold time	10	[s]
Travel distance	400	[mm]
Velocity	100	[mm/s]
Acceleration	100	[mm/s^2]
Hold time	20	[s]
Return position	10	[mm]
k_p	10	
Controller turned off at	± 2	[mm]
Maximum flow through POCV1	± 20	[l/min]
Maximum motor velocity	± 1950	[RPM]

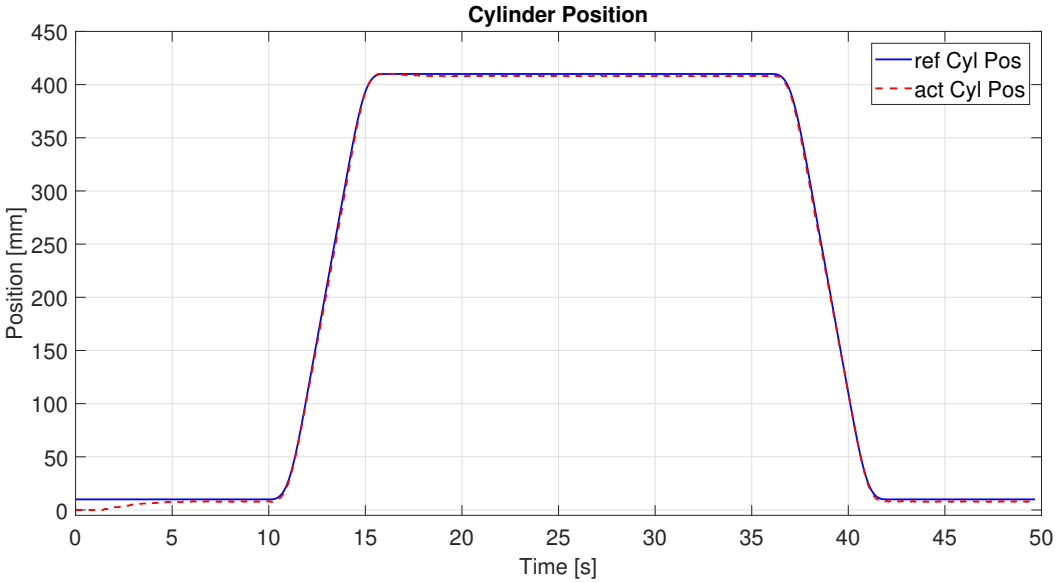

Figure 7.6: Cylinder Position

Figure 7.6 shows that with increased velocity the cylinder is still capable of following the predefined motion profile.

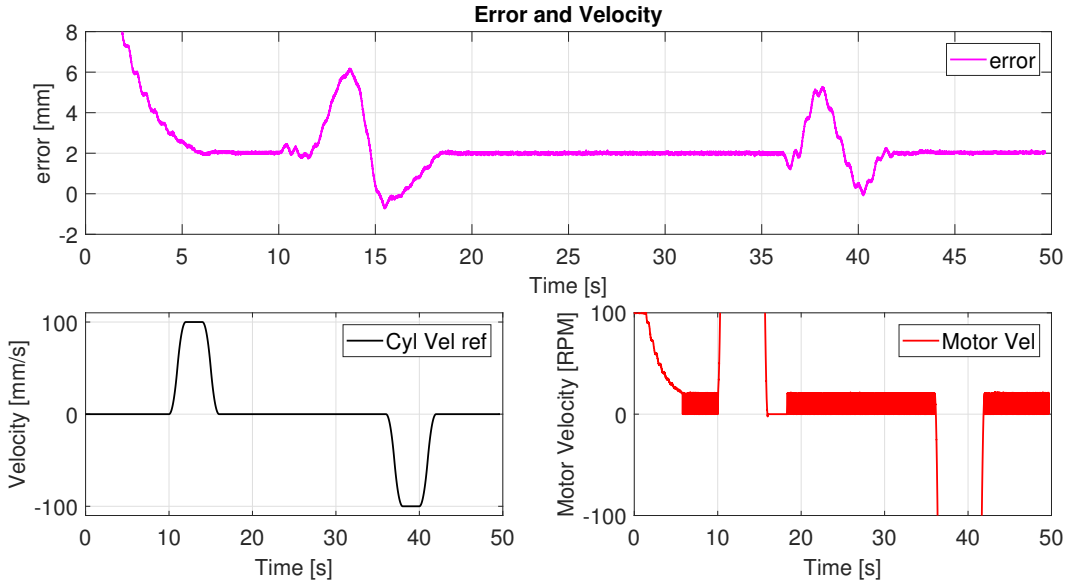

Figure 7.7: Error and Velocity

The cylinder position error is maximum 6 mm as shown in figure 7.7. During the hold period of $18 - 36$ s the position controller is preventing the error of exceeding 2 mm, and motor velocity is oscillating between $0 - 20$ RPM.

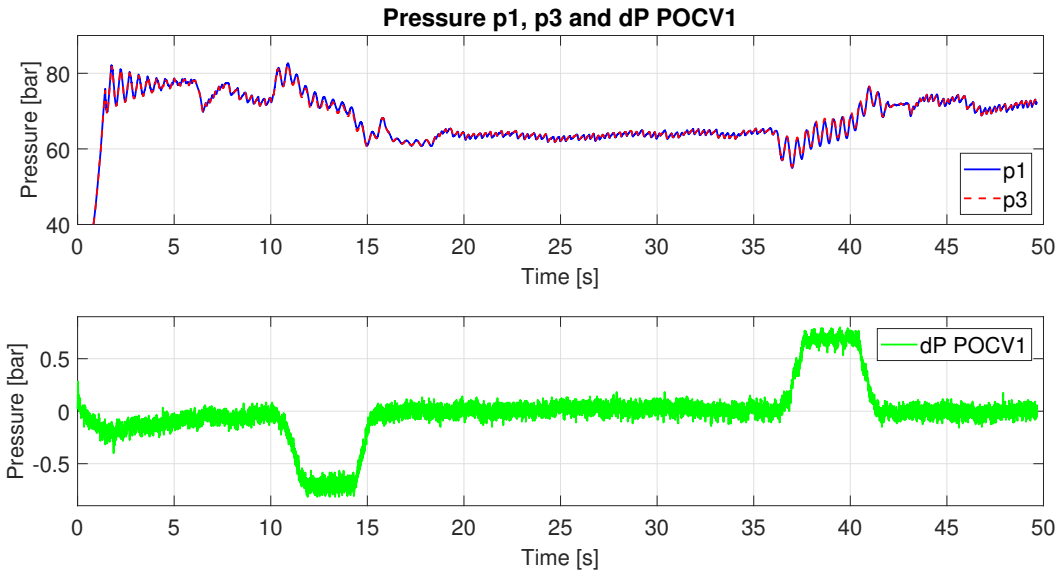

Figure 7.8: Pressure p1, p3 and dP over POCV1

Figure 7.8 shows an equal pressure drop during hoisting and lowering of approximately 0.7 bar, lower than expected, due to crack pressure specification of POCV1.

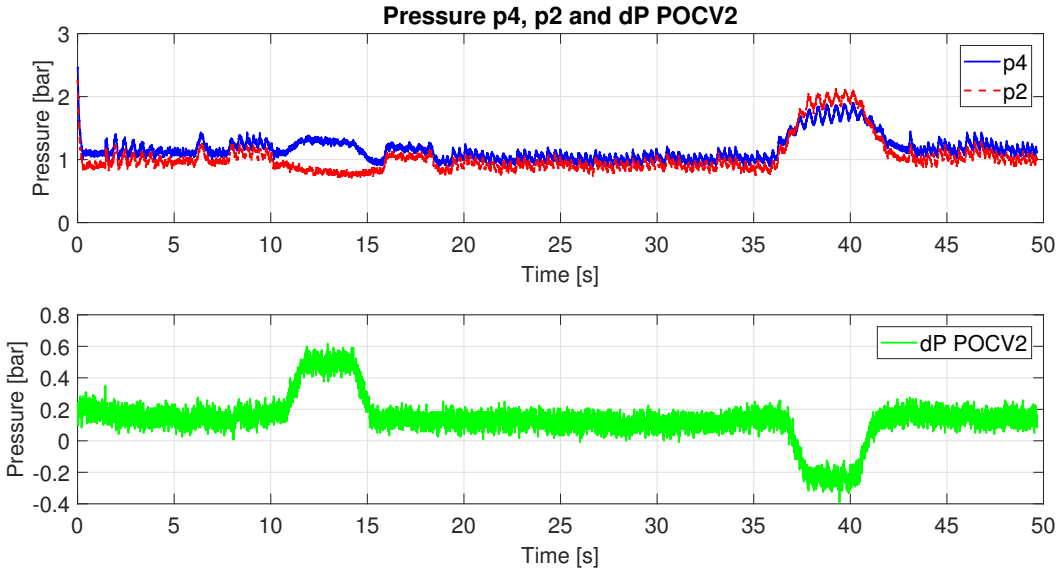

Figure 7.9: Pressure p2, p4 and dP over POCV2

Figure 7.9 shows low pressure drop during hoisting and lowering as expected, but still an unexpected variation around 0.15 bar instead of zero.

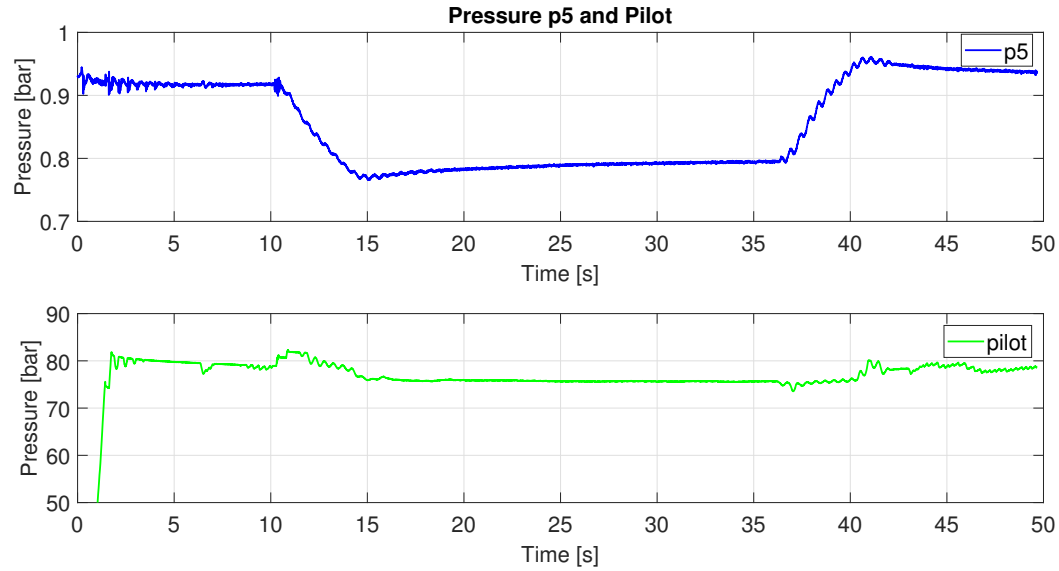

Figure 7.10: Pilot pressure and p5

Figure 7.10 shows that the pilot pressure and p5 as accumulator pressure are still as expected.

7.1.3 Test number 3

In table 7.3 the test parameters for test number 3 are given, passive load holding is not activated.

Table 7.3: Test Parameters

Parameter	**Value**	**Unit**
Start position	10	[mm]
Initial hold time	10	[s]
Travel distance	400	[mm]
Velocity	150	[mm/s]
Acceleration	150	[mm/s^2]
Hold time	20	[s]
Return position	10	[mm]
k_p	10	
Controller turned off at	±2	[mm]
Maximum flow through POCV1	±30	[l/min]
Maximum motor velocity	±2910	[RPM]

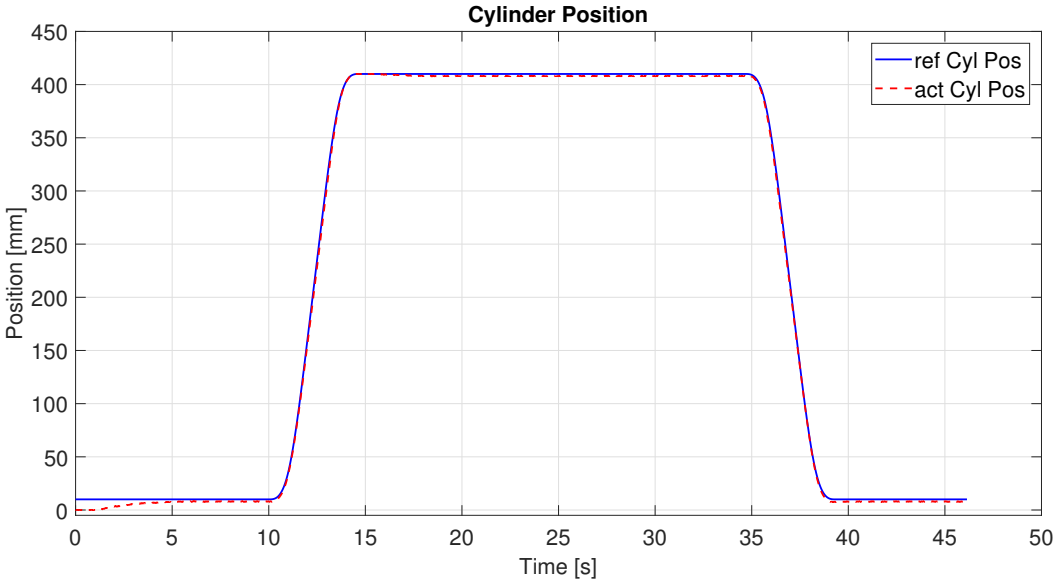

Figure 7.11: Cylinder Position

The maximum cylinder velocity of 150 mm/s as the design criteria is achieved according to figure 7.11 as the cylinder is still able to follow the motion profile.

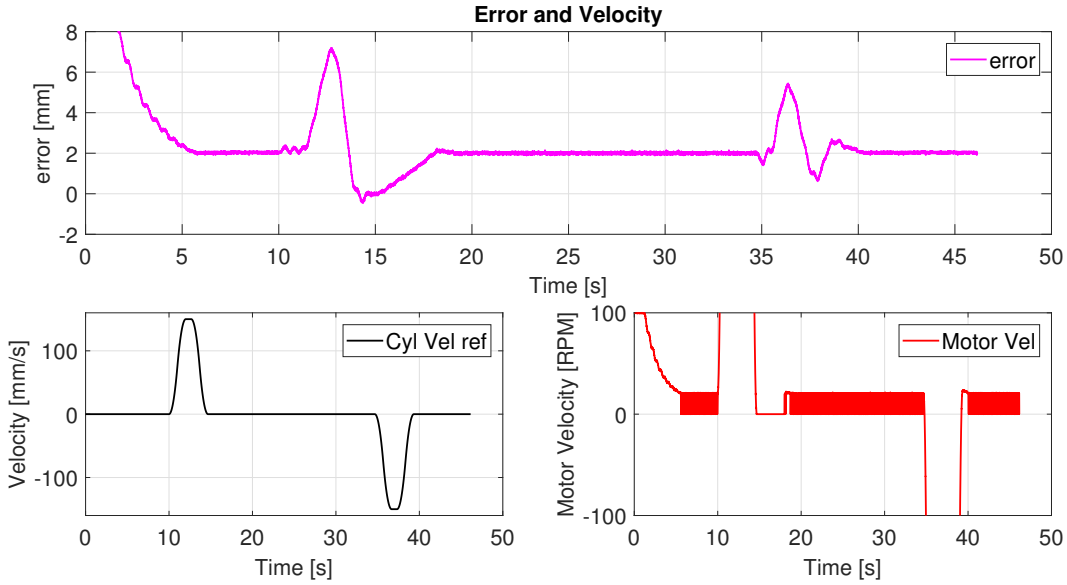

Figure 7.12: Error and Velocity

The error is maximum 7 mm, shown in figure 7.12. The motor controller is used to hold the load, due to leakage in the pump.

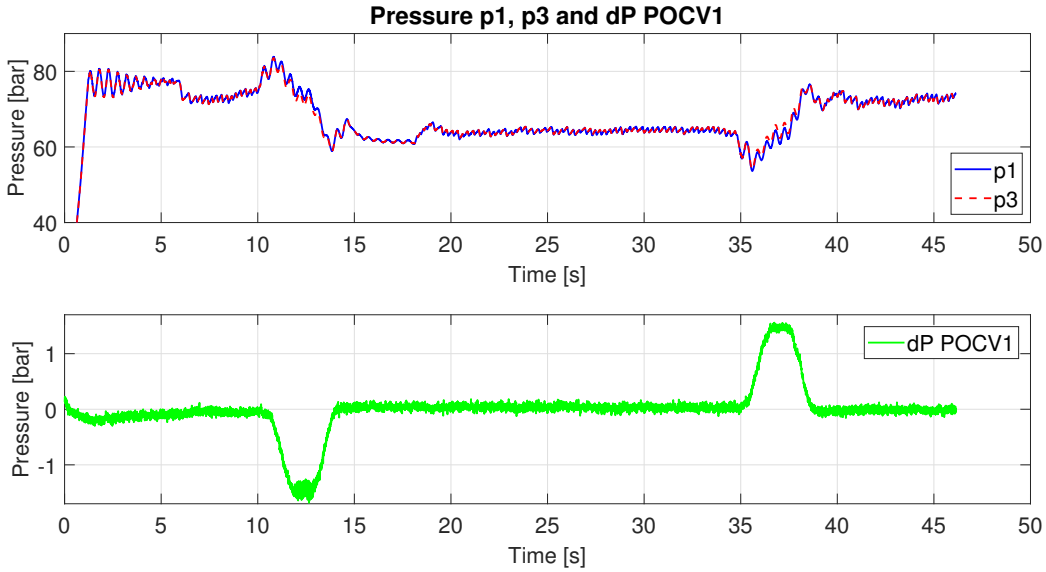

Figure 7.13: Pressure p1, p3 and dP over POCV1

Pressure drop over POCV1 is still lower than expected, shown in figure 7.13.

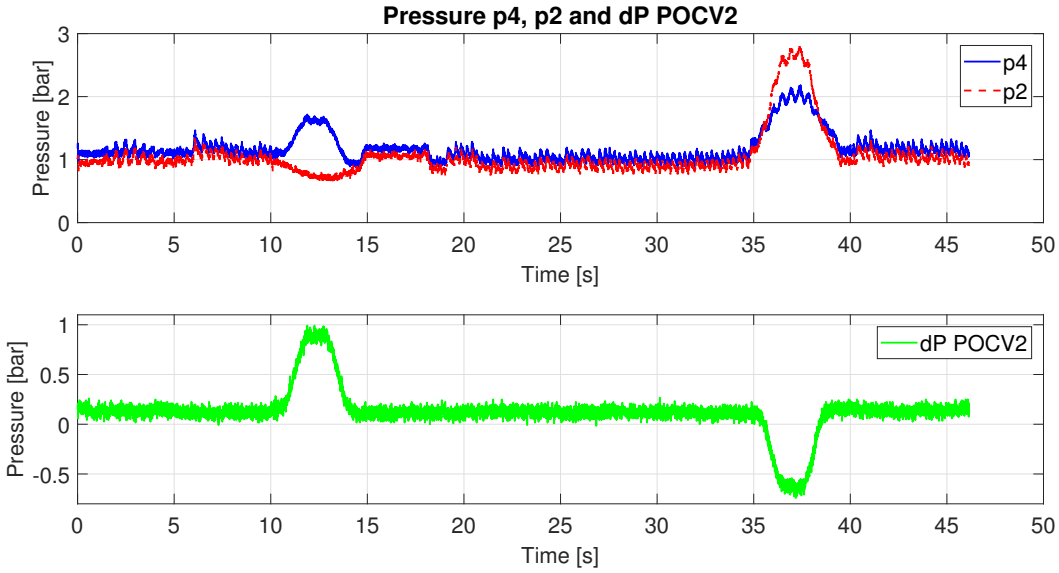

Figure 7.14: Pressure p2, p4 and dP over POCV2

Variation around 0.15 bar instead of zero is persisting, shown in figure 7.14, and there is still low pressure drop, but it is increasing due to an increased flow.

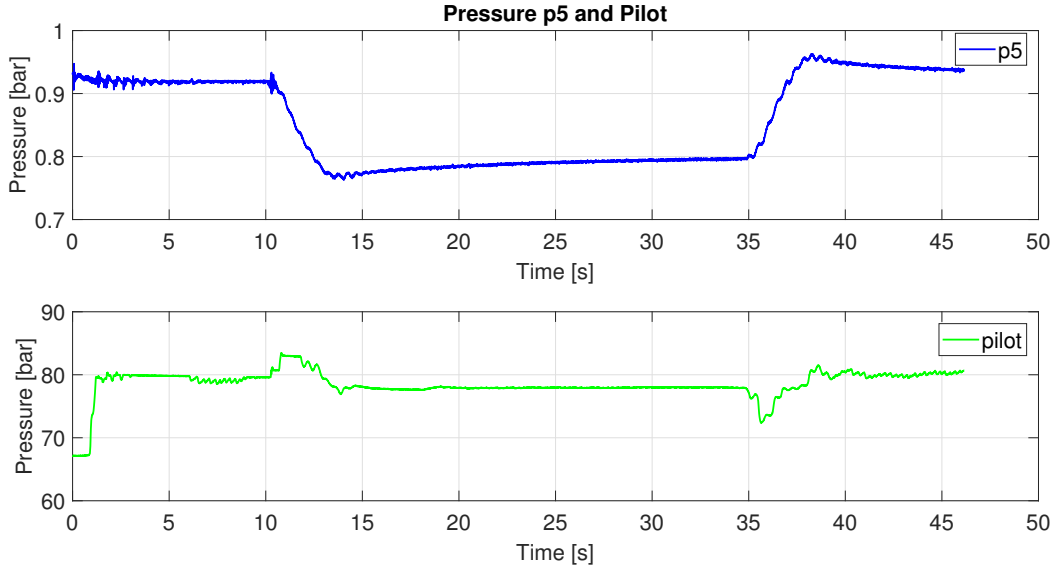

Figure 7.15: Pilot pressure and p5

Pressure p5 and pilot pressure are still behaving as expected, even at maximum velocity of the cylinder shown in figure 7.15.

7.1.4 Test number 4, Passive Load Holding Activated

In table 7.4 the test parameters for test number 4 are given, passive load holding is activated.

Table 7.4: Test Parameters

Parameter	**Value**	**Unit**
Start position	10	[mm]
Initial hold time	10	[s]
Travel distance	400	[mm]
Velocity	50	[mm/s]
Acceleration	50	[mm/s^2]
Hold time	20	[s]
Return position	10	[mm]
k_p	10	
Controller turned off at	± 2	[mm]
Maximum flow through POCV1	± 10	[l/min]
Maximum motor velocity	± 1000	[RPM]

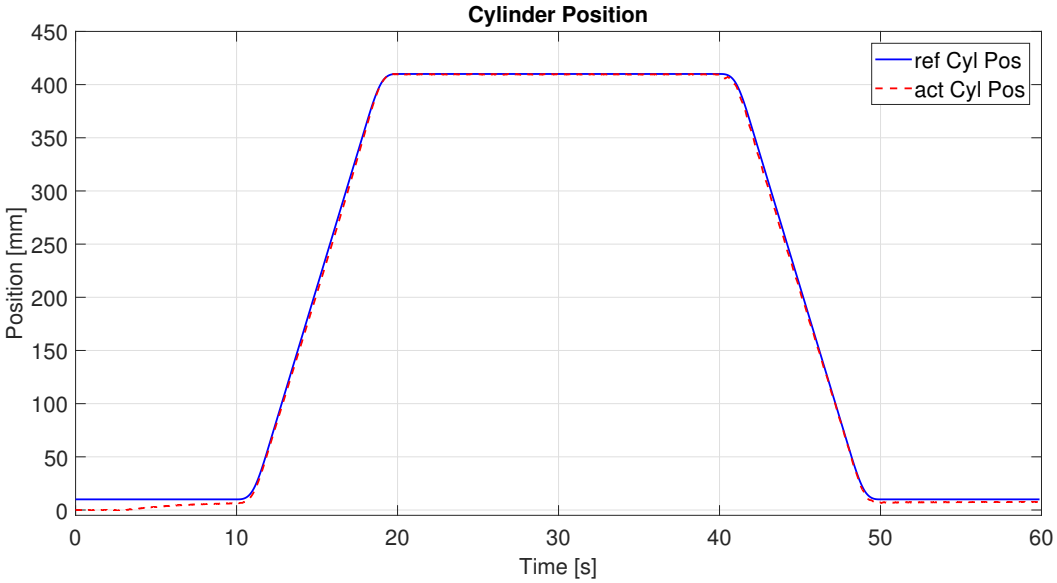

Figure 7.16: Cylinder Position

Figure 7.16 shows that the cylinder is capable of following the motion profile with the passive load holding activated.

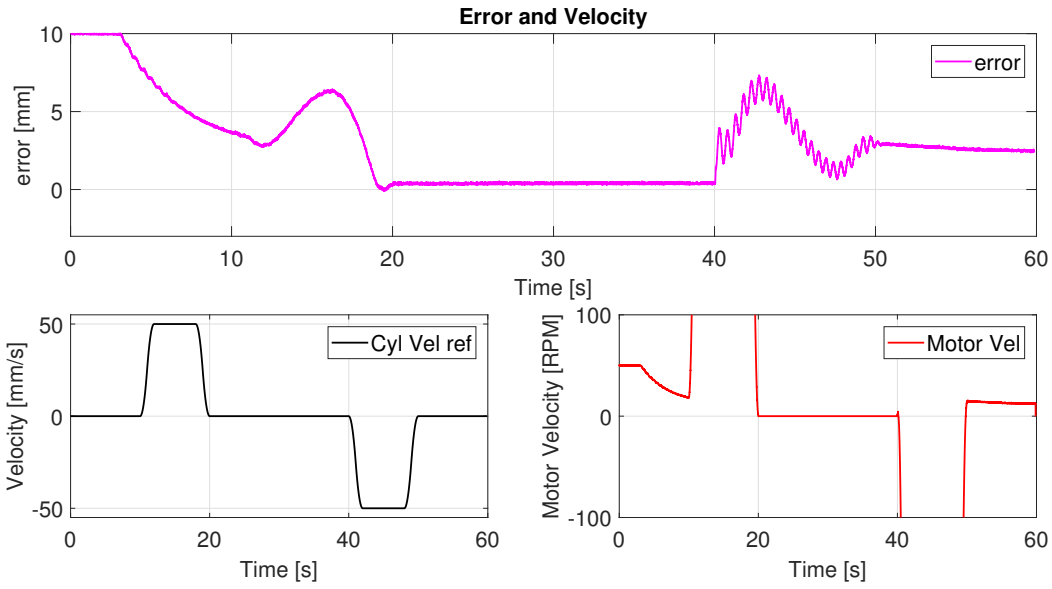

Figure 7.17: Error and Velocity

Figure 7.17 shows that as soon at the velocity command is zero and the error is within the given hysteresis, the passive load holding function is activated, and the motor is shut off. The cylinder position error is holding a steady value.

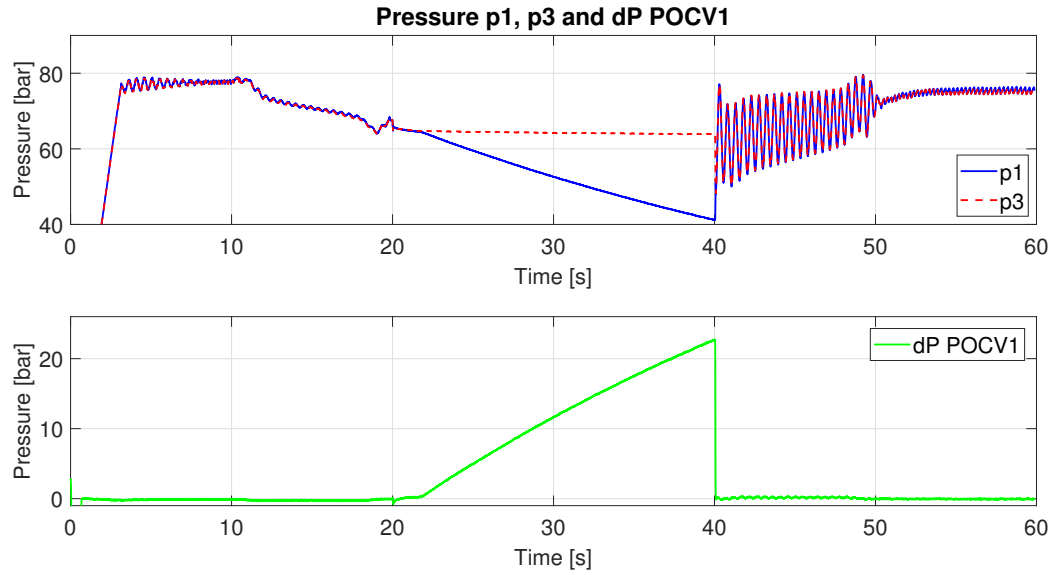

Figure 7.18: Pressure p1, p3 and dP over POCV1

As soon as the load holding is activated, pressure p1 is expected to drop. Figure 7.18 shows this behaviour. When the load holding is disengaged at proximately 40 s, a pressure oscillation is observed. This is due to the large dP over POCV1 when opening the valve. This issue is hopefully solvable by implementing a controller governing the dP before disengaging the load holding functionality.

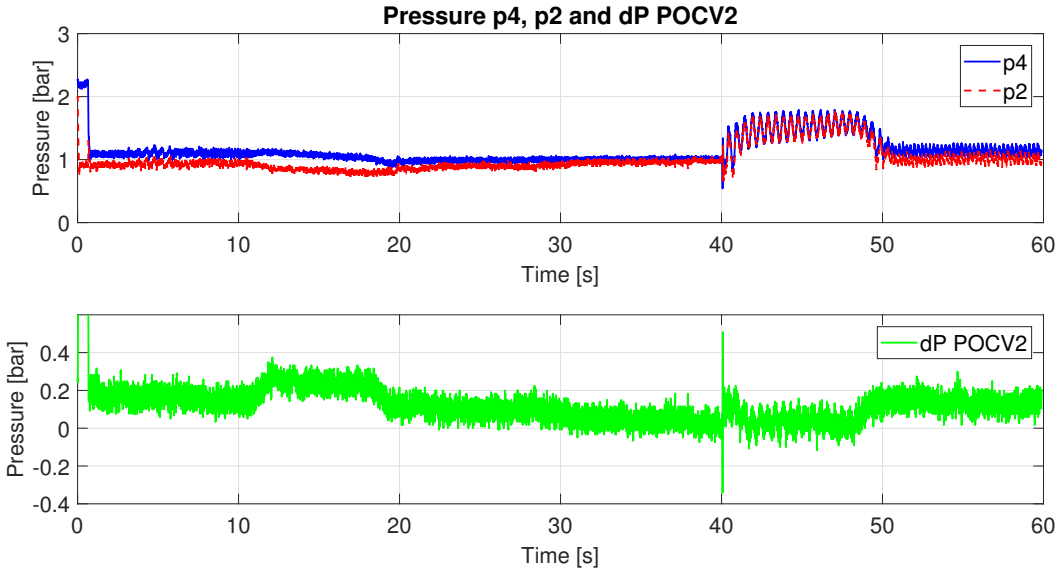

Figure 7.19: Pressure p2, p4 and dP over POCV2

The result of implementing the passive load holding is barely visible on figure 7.19 where only negligible pressure spikes are present, and dP over POCV2 is as expected.

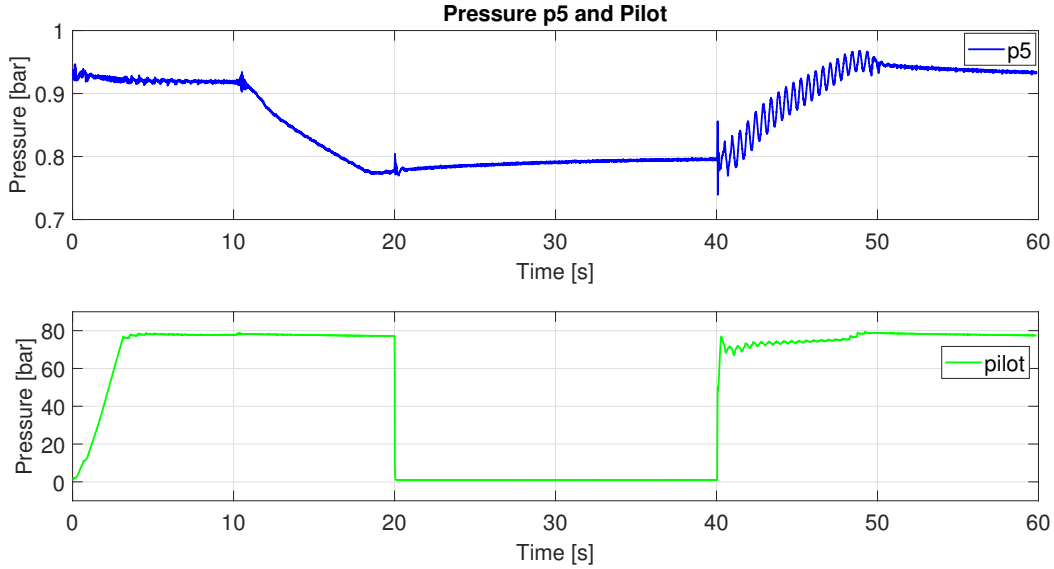

Figure 7.20: Pilot pressure and p5

Pilot pressure in figure 7.20 shows a drop in the time range of $20 - 40$ s, this pressure is the governing pressure for POCV1 and POCV2, and the behaviour is as expected. Pressure p5 is not affected by the load holding functionality.

7.1.5 Test number 5, Sine Wave

In table 7.5 the test parameters for test number 5 are given.

Table 7.5: Test Parameters

Parameter	**Value**	**Unit**
Start position	100	[mm]
Amplitude cylinder stroke	50	[mm]
Period	10	[s]
k_p	10	
Maximum flow through POCV1	±6.5	[l/min]
Maximum motor velocity	±630	[RPM]

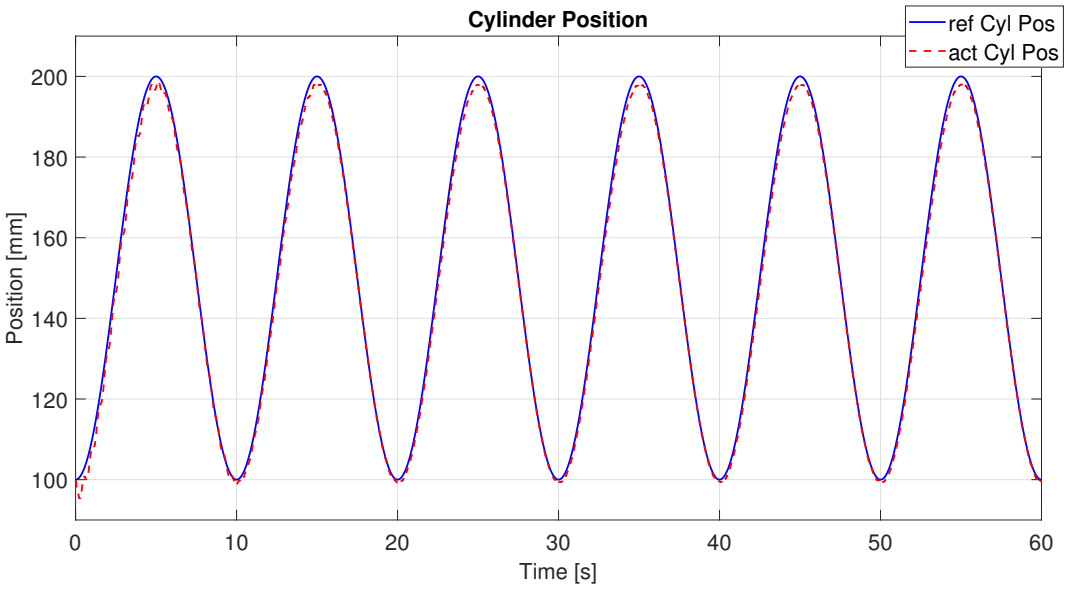

Figure 7.21: Cylinder Position

The system is capable of following a sine wave with a cylinder amplitude of 50 mm during a frequency period of 10 s as shown in figure 7.21.

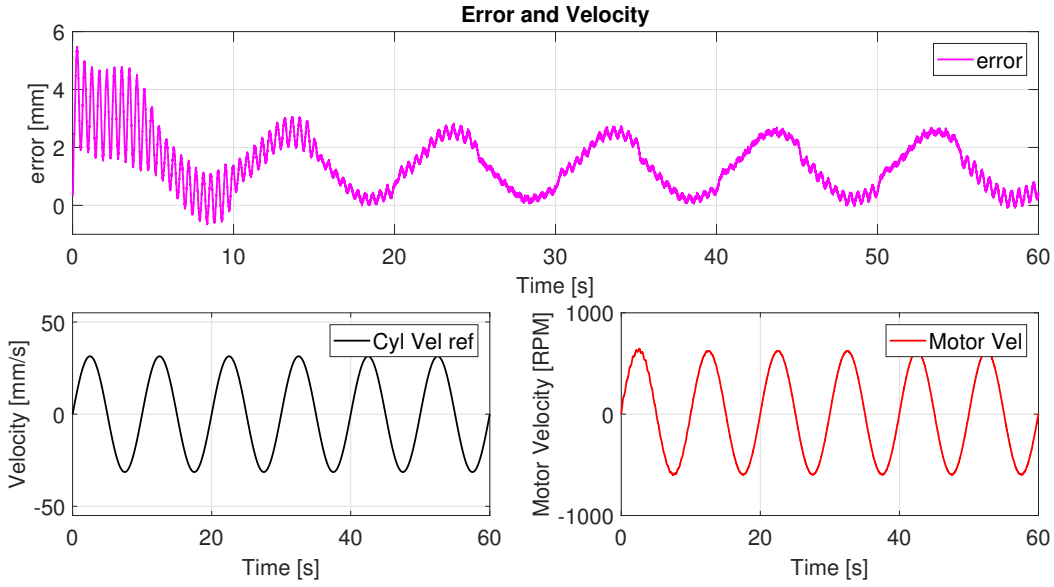

Figure 7.22: Error and Velocity

The position error is at a maximum of 3 mm and has minor oscillations as shown in figure 7.22.

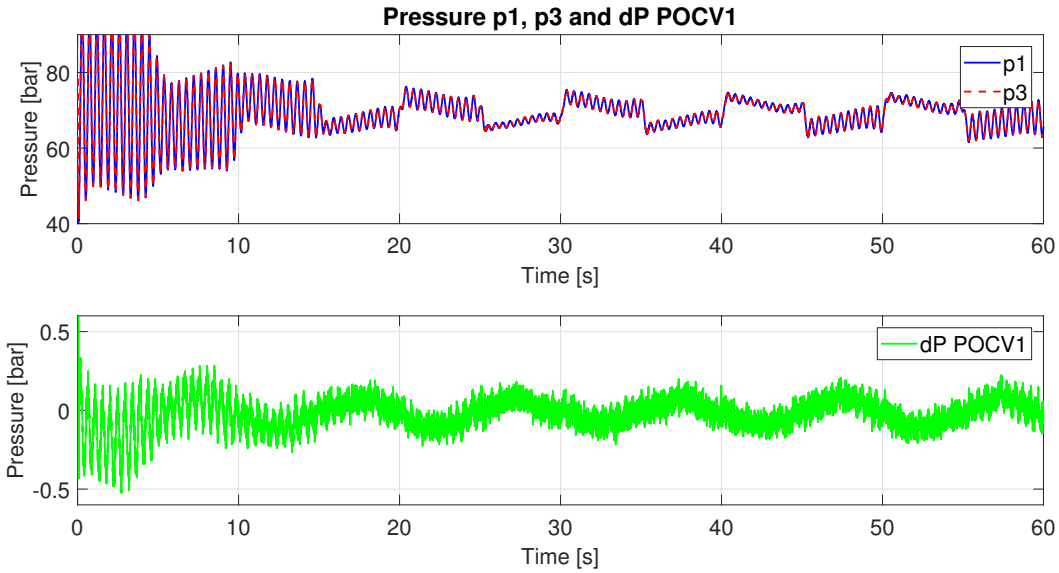

Figure 7.23: Pressure p1, p3 and dP over POCV1

The pressure drop over POCV1 is still at a low level, and has a triangular shape according to figure 7.23.

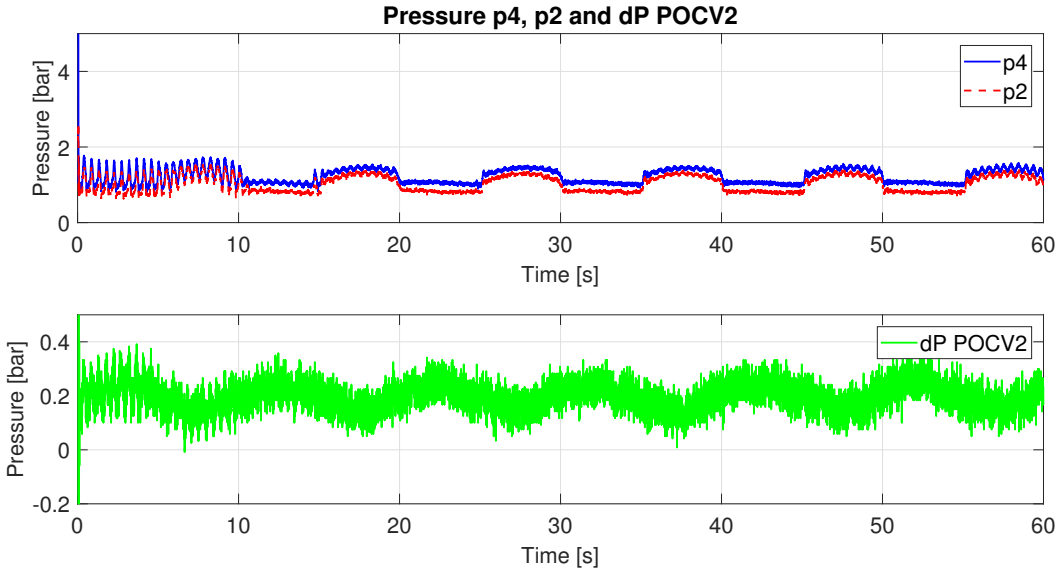

Figure 7.24: Pressure p2, p4 and dP over POCV2

Pressure drop over POCV2 is still varying around 0.15 bar, and has a sinusoidally shape as shown in figure 7.24.

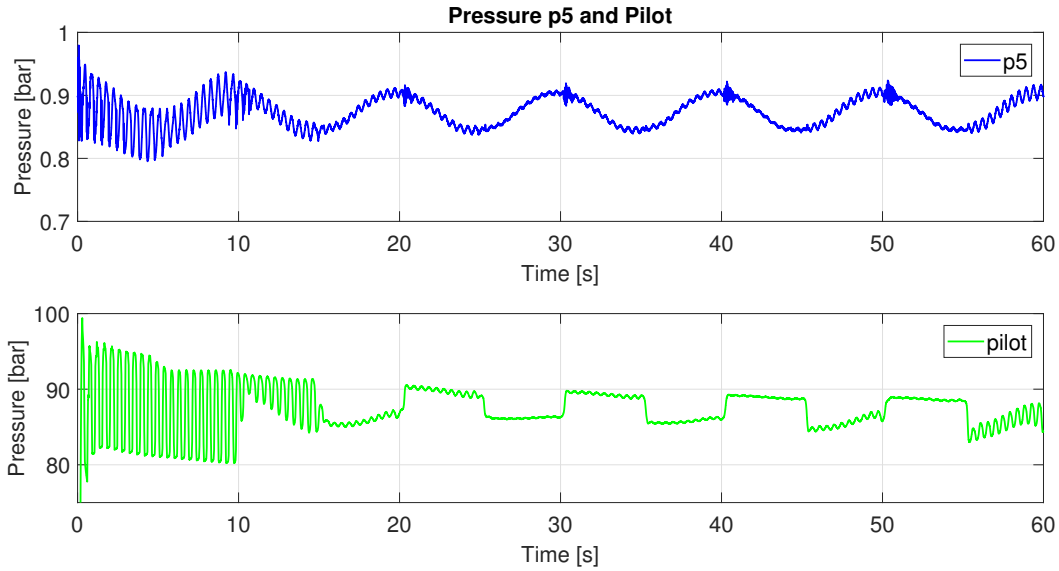

Figure 7.25: Pilot pressure and p5

Pressure p5 is as expected, as it is a function of the cylinder stroke, shown in figure 7.25.

7.1.6 Test number 6, Comparison: Test number 1 and simulation, no passive load holding

Table 7.6 shows a list of the parameters used for the comparison test.

Table 7.6: Test Parameters

Parameter	**Value**	**Unit**
Start position	10	[mm]
Initial hold time	10	[s]
Travel distance	400	[mm]
Velocity	50	[mm/s]
Acceleration	50	[mm/s^2]
Hold time	20	[s]
Return position	10	[mm]
k_p	10	
Controller turned off at	± 2	[mm]
Maximum flow through POCV1	± 10	[l/min]
Maximum motor velocity	± 1000	[RPM]

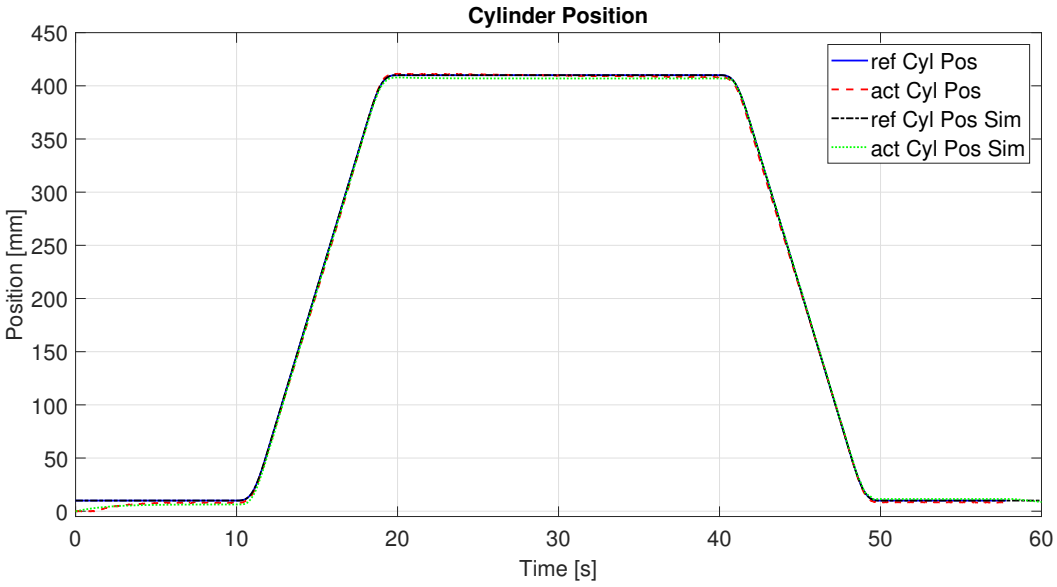

Figure 7.26: Cylinder Position

In figure 7.26 it is shown that the cylinder position is equal for both the experiment and simulation, only small variations are present.

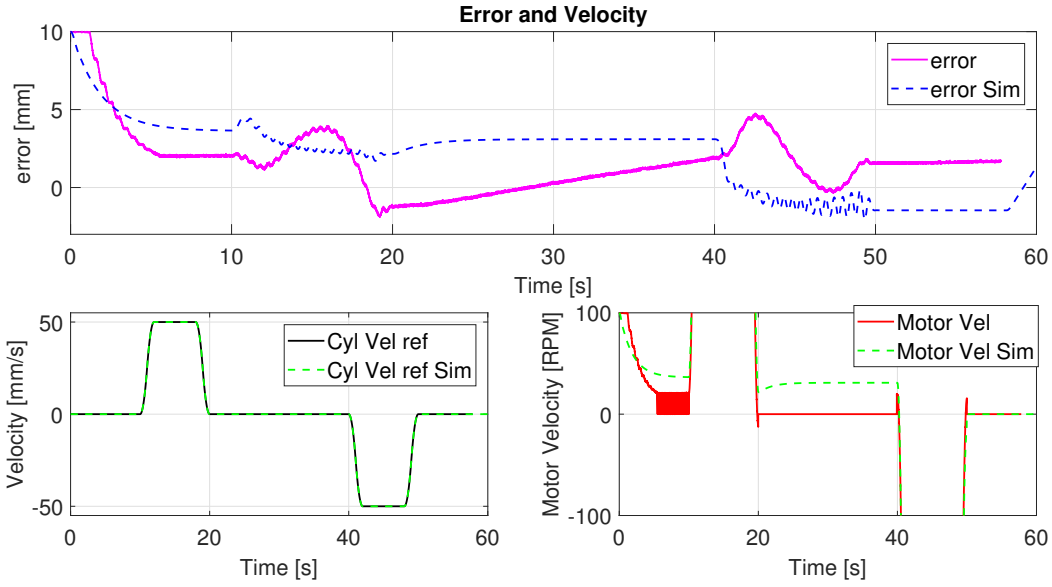

Figure 7.27: Error and Velocity

The position error is in the same range, shown in figure 7.27. For the simulation the motor is holding the load steady, but the experiment shows that the motor is shut off and cylinder is slowly contracting due to leakage in the pump.

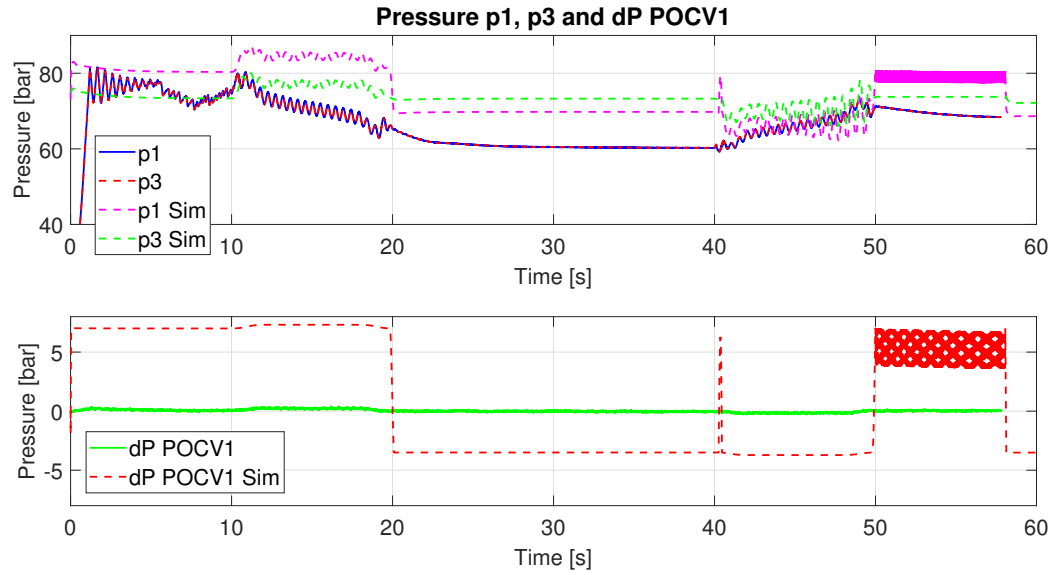

Figure 7.28: Pressure p1, p3 and dP over POCV1

Pressure drop over POCV1 has a large deviation between simulation and experiment, shown in figure 7.28. There is a possibility that there is a mismatch in the crack pressure settings for this valve. In section 2.2.4 it is shown that for the hoisting operation, the POCV is acting as a normal CV and the pilot pressure is not aiding in opening the valve.

Change of Setting for POVC1

Due to the large mismatch of the differential pressure over POCV1 between results from simulation and results from the experiment, it was chosen to change the crack pressure in the Simulink model from 7 bar to 0.3 bar, as the lowest option according to the data sheet of the component. Then as shown in figure

7.29, a more similar result is obtained. It is possible that the manufacturer of the valve manifold has used a different component than the specified one. Another possibility is that there is an error in the Simulink model, even if the same approach was used when modelling both the POCV1 and POCV2. The reason for specifying a crack pressure of seven bars is to ensure that when the low pressure system is selected to be the pilot pressure, do not open the POCV1 and POCV2.

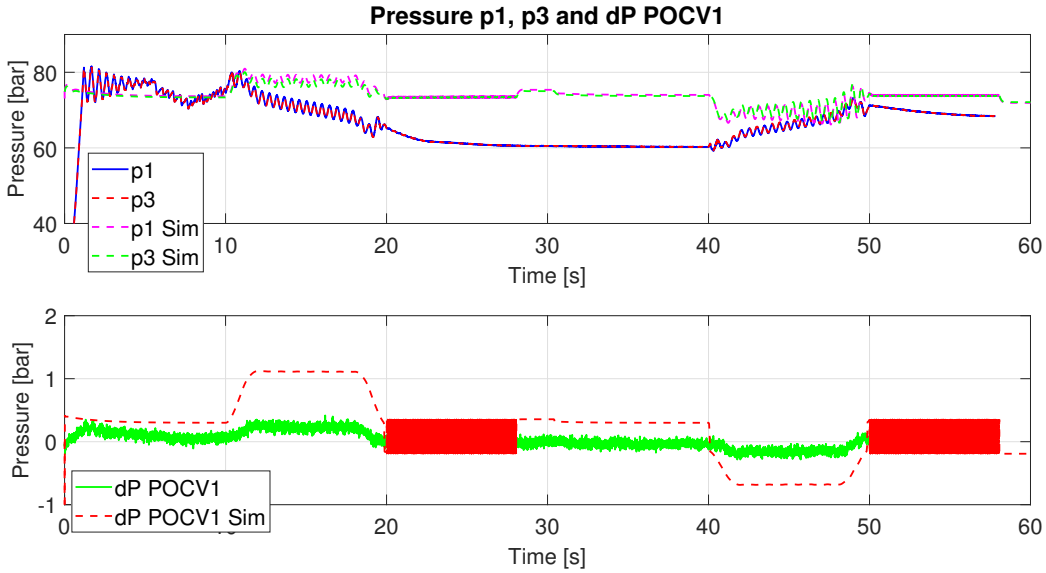

Figure 7.29: Pressure p1, p3 and dP over POCV1

For POCV2 figure 7.30 shows a good match between simulation and experiment, only the offset of 0.15 bar for the experiment dP is deviating the result.

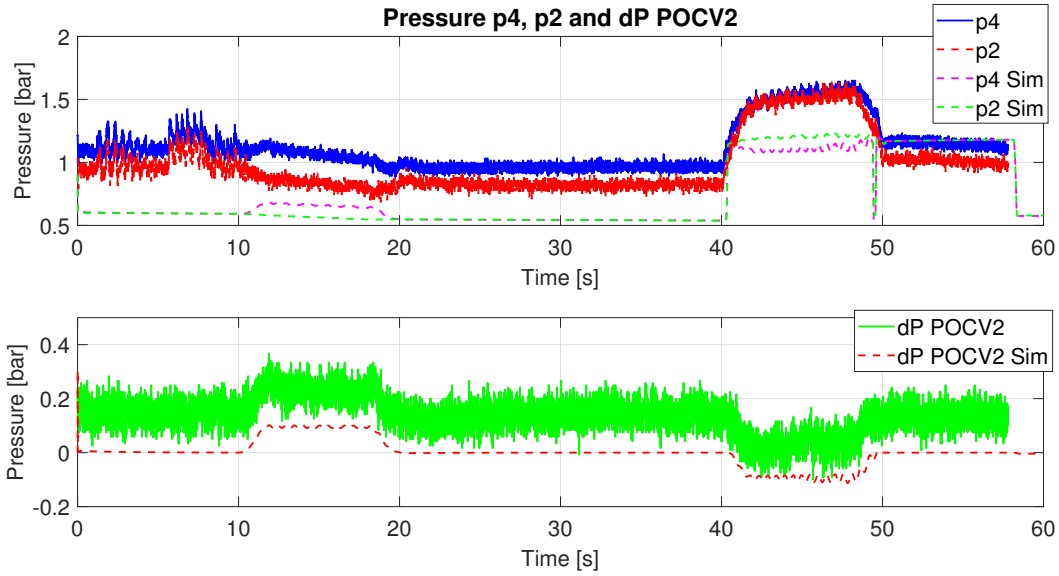

Figure 7.30: Pressure p2, p4 and dP over POCV2

Pilot pressure and p5 as accumulator pressure are in the same range and show the same trends, as seen in figure 7.31.

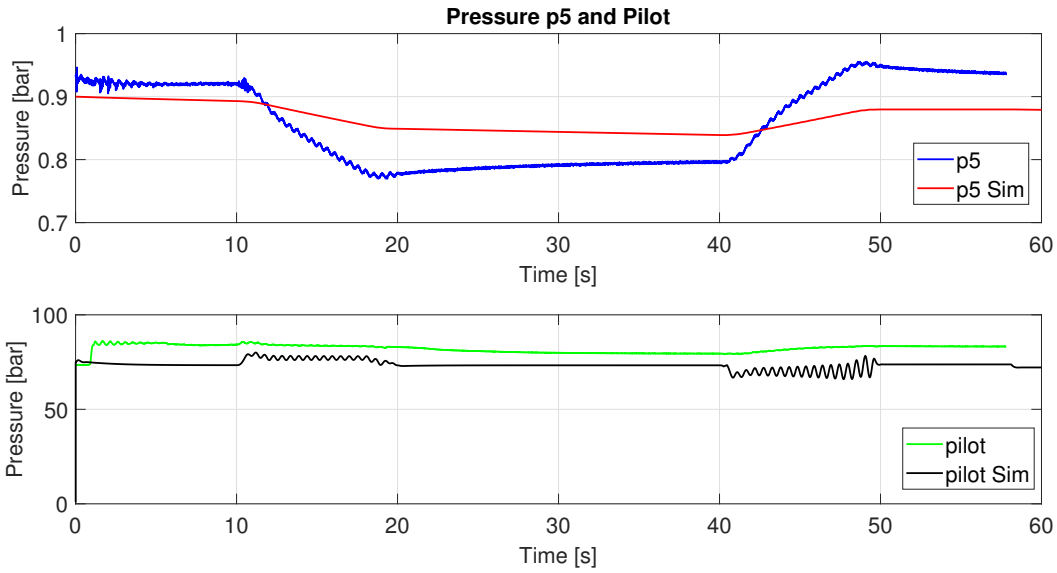

Figure 7.31: Pilot pressure and p5

7.1.7 Choice of Mechanical Model in Simulation

When running tests on the flexible crane model described in section 5.4, the results showed more instability in pressures compared to experimental results. Due to this, further work on the dynamic model was not carried out and results are not included. In the Simulink simulation the crane model derived in 5.2 and 5.3 was used.

7.1.8 Choice of Controller

Due to the limited time for experimental work the controller implemented was a P-controller and a constant feed forward gain from section 6.3.2, this combination did perform well. The designed PI-controller in section 6.4 did perform worse, but was not investigated further.

Chapter 8

Conclusion

The test bed was up and running on May 16^{th} after many weeks of waiting for the replacement pump. As soon as the staff at the machine hall had filled the system with oil and did their best in bleeding air from the system, the initial testing of the system started. A joystick was previously mounted for testing the PMSM, and now as the pump was mounted, it was possible to get flow and pressure to move the cylinder and the boom. It looked promising. As the hydraulic system is completely sealed there will be no natural air bleeding when the system is operating, so one more round of air bleeding was necessary. Pressure sensors and a cylinder position sensor was already connected to the PLC, and signals were displayed on the screen through Simulink. The 3/2 valve controlling the pilot pressure was also connected and the system was ready to get into work. A P-controller was set up and a motion profile prepared. By starting with gains below the calculated values to be on the safe side, and controlling the 3/2 value manually, it worked exactly as planned. Several cycles were tested, with different velocities and accelerations, with and without passive load holding, now implemented in the controller structure. Pilot operated check valves were tested to be suitable for load holding purposes. The PMSM was performing as expected right out of the box. Unfortunately, the deadline for handing in the report was closing in and experimental work had to be laid down in order to finalize the report.

The passive load holding capability of the self contained electro hydraulic cylinder is working as expected and experiments confirm this. Depending on the required accuracy, the controller has room for improvement, but as of today the system can follow a typical hoist-hold-and-lower motion with mm accuracy with a significant load.

Chapter 9

Nomenclature

Variable	Unit	Explanation
a_i $(1 \leq i \leq 333)$		Coefficients of curve fitting polynomial
A_l	-	Linearised model A-matrix
A_m	m^2	Area of the cross section of the material
A_p	m^2	Pressure area on piston side
A_r	m^2	Pressure area on rod side
A_{pist}	m^3	Pressure area of piston in POCV
A_{pop}	m^3	Pressure area of poppet in POCV
$A(y_c)$	m^2	Discharge area as function of poppet displacement y_c
b	Ns/m	Viscous damping constant
b_l	Ns/m	Viscous damping constant linearised model
$\hat{b}$	Ns/m	Estimated damping constant
b_a	Ns/m	Active damper in speed controller
B	T	Magnetic flux density
$B_a(\theta)$	T	Magnetic flux density as function of angle, for phase a
$B_{l,hoi}$	-	Linearised model B-matrix for hoisting
$B_{l,low}$	-	Linearised model B-matrix for lowering
B_m	T	Magnetic flux density in the material
$\vec{B}_r(t)$	T	Rotor flux density, varying with time t
$\hat{B}_r$	T	Rotor flux density, constant value
C_l	-	Linearised model C-matrix
C_d	-	Discharge coefficient
Ch_{accu}	m^3/Pa	Capacitance of the accumulator
C_{Hi} $(1 \leq i \leq 7)$	m^3/Pa	Capacitances of pressure node 1-7
Ch_l	m^3/Pa	Capacitance linearised model
d_{po}	m	Diameter of pilot operated check valve poppet diameter
d_{cv}	m	Diameter of check valve poppet diameter
D_l	-	Linearised model D-matrix
D_p	m^3/(rad)	Displacement of pump

Continues on next page

Variable	Unit	Explanation
D_{ref}	m^3	Displacement of real measured pump
D_{scaled}	m^3	Displacement of modelled pump
e	A	Error to current controller
e_{emf}	V	Induced emf
e_i	V	Induced emf in phase i, $i \in$ (a,b,c)
e_s	rad/s	Error signal to speed controller
e_{ess}	m	Error steady state for the position control
$\vec{e}_{ms,\vec{B}_r}(t)$	V	Induced emf due to rotating $\vec{B}_r(t)$
E	MPa	The elasticy module of the material
E	V	Back emf
E_{kin}	Joule	Kinetic energy of the beam and load
$\hat{E}$	V	Estimated back emf
f	-	Curve fitting function
f_c	N	Coulomb friction
f_{em}	N	Force
f_M	-	Function of mechanical losses in pump
f_Q	-	Function of flow losses in pump
f_s	N	Stribeck friction
f_v	Ns/m	Viscous friction
$F_a(\theta)$	T	mmf as function of angle for phase a
F_c	N	Force from cylinder applied on the load
$F_c(s)$	-	Transfer function for current controller
F_{CV}	N	The sum of forces on the valve poppet check valve
F_{ext}	N	External forces
F_f	N	Friction force
$F_{k,0}$	N	Force from pretension of spring in POCV
$F_{k,0RV}$	N	Force from pre-tensioning of the spring relief valve
F_{RV}	N	The sum of forces on the valve poppet relief valve
$G'(s)$	-	Transfer function of plant with implemented decoupler and active damper
$G_{cc}(s)$	-	Transfer function from i_{ref} to i
$G_c(s)$	-	Transfer function fro plant
$G'_c(s)$	-	Transfer function of plant with implemented active damper
$G_{c,Lag}$	-	Transfer function of the Lag controller
G_{ma}	dB	Gain margin at the poles in the linearised model
H	A/m	Magnetic field intensity
H_i	V	Magnetic field produced in phase i, $i \in$ (a,b,c)
H_m	A/m	Magnetic field intensity along mean path
i	A	Current
$i_{d,ref}$	A	i_d reference signal
i_i	A	Current in phase i, $i \in$ (a,b,c)
i_{max}	A	Short term maximum allowed stator current
$i_{q,max}$	A	Maximum allowed iq due to maximum acceleration

Continues on next page

Variable	Unit	Explanation
$i_{q,ref}$	A	Limited i_q signal from saturation function
$i_{q,ref,nom}$	A	$i_q$reference signal from speed controller and active damper
I		Integrator state variable
I_{beam}	kgm^2	Moment of inertia for a beam
$I_{CG,beam}$	kgm^2	Moment of inertia for a beam around centre of gravity
I_d	A	Integrator state variable for i_d
I_{pl}	kgm^2	Moment of inertia of pay load
I_q	A	Integrator state variable for i_q
I_s		Speed integrator state variable
I_{tot}	kgm^2	Mass moment of inertia for the beam and load
I_z	m^4	2^{nd} moment of inertia for the cross section of the prismatic beam
j		The complex number j
J_m	kgm^2	Moment of inertia of motor
$\hat{J_m}$	kgm^2	Estimated moment of inertia of motor
k	N/m	Stiffness of spring in POCV
k_{CV}	m^3/(Ns)	Linear flow coefficient
$k_{eq,m,n}$	N/m	Equivalent spring stiffness of two torsional springs in series
$k_{f,i}$	N/m	Spring stiffness
k_i	s^{-1}	Integral gain current loop
$k_{i,L}$	s^{-1}	Integral gain of the Lag controller
k_{is}	s^{-1}	Integral gain speed controller
$k_{L,i}$	-	Internal leakage coefficient cylinder
k_m	N/m	Spring stiffness of the first spring in the series
k_n	N/m	Spring stiffness of the second spring in the series, equal to k_m
k_p	V/A	Proportional gain current loop
k_{ps}	Nm/(rad/s)	Proportional gain speed controller
k_{RV}	m^3/(Ns)	Linear flow coefficient relief valve
K	-	Space vector scaling constant
K_{adj}	dB	The gain reduction in dB in the Lag controller
$K_{e_{ss}}$		Gain to meet steady state requirement
K_f	Pa^{-1}	Compressibility of fluid
K_m	rad/sA	Motor dynamic gain
K_{L1}	m^3/Pa	Leakage coefficient due to pressure
K_{L2}	m^{3}s/m	Leakage coefficient due to piston velocity
K_{sys}	RPM/m	System gain linearised model
l	m	Length of conductor
l_g	m	Length of air gap
l_m	m	Mean length of path enclosing the currents
l_{rod}	m	Length of cylinder rod
l_{stroke}	m	Stroke length of cylinder
L	H	Inductance
$\hat{L}$	H	Estimated inductance

Continues on next page

Variable	Unit	Explanation
L_{ab}	m	Length rotational joint beam to lower bracket cylinder
L_{ac}	m	Length rotational joint beam to upper bracket cylinder
L_{bc}	m	Cylinder length, variable
$\dot{L}_{bc}$	m/s	Cylinder velocity
$L_{COG,beam}$	m	Distance from centre of gravity to rotational point, equal to $L_{COG,beam,x}$ figure 5.1
$L_{COG,PL,x}$	m	Length from A to centre of gravity for pay load in x-direction
$L_{COG,PL,y}$	m	Length from A to centre of gravity for pay load in y-direction
L_m	H	Magnetization inductance
L_m	H	Inductance
$L_{s,i}$	m	Length of the element
L_1	m	Length of beam
m	kg	Mass of fluid
m_{beam}	kg	Mass of the beam
m_{pl}	kg	Mass of pay load
m_{eq}	kg	Equivalent mass
$m_{eq,l}$	kg	Equivalent mass linearised model
$M(\omega)$	-	Magnitude frequency response
$M_i(\omega)$	-	Amplitude of input
$M_o(\omega)$	-	Amplitude of output
M_S	Nm	Mechanical losses in pump
$M_{s,ref}$	Nm	Reference mechanical losses, pump
$M_{s,scaled}$	Nm	Scaled mechanical losses, pump
n_p	rad/s	Rotational speed of pump
n_{po}	-	Number of pole pairs
n_{ref}	RPM	Reference rotational speed pump
n_{scaled}	RPM	Scaled rotational speed, for the modelled pump
N	-	Number of windings
N_g	-	Poly tropic coefficient
N_s	-	Number of windings in stator
p	Pa	Fluid pressure
p_0	Pa	Initial fluid pressure
p_g	Pa	Gas pressure in accumulator
$p_{g,0}$	Pa	Pre loading pressure accumulator
p_{max}	Pa	Maximum accumulator pressure
p_{min}	Pa	Minimum pressure in accumulator
p_{lp}	Pa	Pressure of low pressure system
P	s^{-1}	Proportional gain of the Lag controller
P_A	Pa	Inlet pressure
P_B	Pa	Outlet pressure
$\dot{P}_i$ $(1 \leq i \leq 7)$	Pa/s	Pressure gradients in pressure node 1-7
P_{in}	W	Input power
P_{out}	W	Output power

Continues on next page

Variable	Unit	Explanation
P_p	Pa	Pressure on piston side
P_{po}	W	Power
ΔP_{pump}	Pa	Pressure drop over pump
P_r	Pa	Pressure on rod side
P_{pilot}	Pa	Pilot pressure to POCV
Q	m^3/s	Net flow into a pressure node
Q_{CV}	m^3/s	Flow through the check valve
$Q_{CVi} (1 \leq i \leq 2)$	m^3/s	Flow through check valve 1 and 2
$Q_i (1 \leq i \leq 2)$	m^3/s	Pump flow into pressure node 1 and 2
$Q_{L,i}$	m^3/s	Internal leakage cylinder
Q_{or}	m^3	Flow through orifice
$Q_{p,p}$	m^3/s	Pump flow in pump mode
$Q_{p,m}$	m^3/s	Pump flow in motor mode
Q_{POCVi} $(1 \leq i \leq 4)$	m^3/s	Flow through pilot operated check valve 1,2,3 and 4
Q_{RV}	m^3/s	Flow through the relief valve
Q_{RVi} $(1 \leq i \leq 4)$	m^3/s	Flow through relief valves 1,2,3 and 4
Q_s	m^3/s	Flow losses in pump
$Q_{s,ref}$	m^3/s	Reference flow losses,pump
$Q_{s,scaled}$	m^3/s	Scaled flow losses, pump
Q_{th}	m^3/s	Theoretical pump flow
r_{rod}	m	Radius of cylinder rod
R	Ohm	Resistance
$\hat{R}$	Ohm	Estimated resistance
R_a	Ohm	Active damper
R_{pl}	m	Length from pay load centre of gravity to rotational point A
s	rad/s	Variable in the frequency domain
t	^{o}C	Fluid temperature
t_0	^{o}C	Initial fluid temperature
t_p	s	Duration of working cycle for accumulator
t_r	s	Rise time
T_{em}	Nm	Electro mechanical torque
$T_{em,max}$	Nm	Maximum electro mechanical torque, PLC
T_p	Nm	Torque pump
T_{po}	Nm	Torque concerning power calculation
TF_{plant}	-	Transfer function of the linearised plant model
T_1	s	Time constant 1 lead-lag compensator
T_2	s	Time constant 2 lead-lag compensator
u	m/s	Velocity
u_{cond}	m/s	Velocity of conductor
u_m	-	The normalized unit velocity command
v	V	Voltage
v_e	m/s	Translational velocity

Continues on next page

Variable	Unit	Explanation
v'	V	Output voltage from current controller
v_{po}	m/s	Velocity concerning power calculation
v_{ramp}	-	Slope of the ramp
v_{ref}	V	Saturated voltage signal
$\bar{v}_{ref}$	V	Reference voltage signal
V_{base}	V	Limited armature voltage determined by the power electronic converter
V	m^3	Fluid volume
$\dot{V}$	m^3/s	Time derivative of expansion
V_0	m^3	Initial volume of a pressure node
V_{fluid}	m^3	Fluid volume in accumulator
V_g	m^3	Gas volume in accumulator
$V_{g,eff}$	m^3	Effective gas volume of accumulator
$V_{g,min}$	Pa	Minimum gas volume in accumulator
$V_{g,max}$	Pa	Maximum gas volume in accumulator
V_i $(1 \leq i \leq 2,\ 5 \leq i \leq 7)$	m^3	Volumes of pressure node 1,2,5,6 and 7
V_l	m^3	Volume of lines linearised model
$V_{1,l}$	m^3	Fixed volume of pressure node linearised model
V_p	m^3/rad	Fixed pump displacement
$\mathbf{x}$	-	State space model vector
$\mathbf{x_s}$	-	State space vector simplified model
$\mathbf{x_{sl}}$	-	State space vector linearised model
$x_{1,sl}$	m/s	Cylinder velocity state variable
$x_{2,sl}$	Pa	Pressure state variable
x_c	m	Position of cylinder extraction
$x_{c,l}$	m	Cylinder stroke linearised model
x_i $(1 \leq i \leq 3)$	-	Curve fitting variables
$x_{i,s}(1 \leq i \leq 7)$	-	State variables in the state space representation of the model
$\mathbf{y}$	-	State space model vector
y_c	m	Poppet displacement in POCV
$y_i(1 \leq i \leq 2)$	m	Pilot operated check valve poppet displacement for valve POCV1 and POCV2
$y_{CVi}(1 \leq i \leq 2)$	m	Check valve poppet displacement for valve CV1 and CV2

Greek Letters		
α		Coefficient in lead-lag compensator
α_c	rad/s	Bandwidth of current loop
α_{max}	rad/s	Maximum acceleration of motor, PLC
β_l	-	Coefficient in lead-lag compensator
β_s	-	Swash plate angle, normalised
η_v	-	Volumetric efficiency pump

Variable	Unit	Explanation
η_{sys}	-	System efficiency
γ	-	Linear scaling factor
λ_{loss}	-	Dimensionless scaling factor
μ_0	Henries/m	Permeability of air or free space
μ_m	Henries/m	Permeability of the ferromagnetic material
μ_r	Henries/m	Permeability of the ferromagnetic material relative to permeability of free space
λ	W_b	Flux linkage
ω	rad/s	Frequency
ω_p	rad/s	Angular velocity pump
ω_{po}	rad/s	Angular velocity concerning power calculation
ω_r	rad/s	Rotor angular velocity
ω_{ref}	rad/s	Reference rotor velocity
ω_1	Hz	Angular frequency of input voltage
$\omega_{1,L}$	rad/s	Frequency where the gain should be decreased in the lag controller
ψ	Wb-t	Flux linkage
$\hat{\psi}_R$	Wb-t	Approximated flux linkage of rotor
$\Re_m$	H^{-1}	Magnetic reluctance
ρ_{oil}	kg/m^3	Density of fluid
ϕ_m	W_b	Magnetic flux
ϕ_M	^{o}	Phase margin at cross frequency
$\phi(\omega)$	^{o}	Phase frequency response
$\phi_i(\omega)$	^{o}	Phase of input
$\phi_o(\omega)$	^{o}	Phase of output
τ_m	s	Time constant of the motor dynamics
τ_s	s/m	Time-constant Stribeck friction
θ	rad	Angle with respect to a-axis
θ_e	rad/s	Angular velocity
$\theta_m(t)$	rad	Angle with respect to a-axis, varying with time t
$\theta_i(1 \leq i \leq 6)$	^{o}	Angles in figure 5.2
$\dot{\theta}_6$	rad/s	Angular velocity of the beam and load

Chapter 10

Acronyms

Acronym	Explanation
AC	Alternating Current
BLDC	Brushless Direct Current motor
CV	Check Valve
CW	Clock Wise
CCW	Counter Clock Wise
DAQ	Data Acquisition
DQ	Direct Axis and Quadrature axis
DC(el)	Direct Current
DC(hyd)	Differential Cylinder
dP	Differential Pressure
EHA	Electro Hydraulic Actuator
EHC	Electro Hydraulic Cylinder
EMF	Electromotive Force
FOC	Field Oriented Control
FPVM	Fixed displacement Pump and Variable Motor speed
HVDC	High Voltage Direct Current
HPU	Hydraulic Power Unit
ISO	International Standard Organization
MOSFET	Metal Oxide Semiconductors Field Effect Transistors
MMF	Magneto Motive Force
OR	Orifice
PBW	Power By Wire
PLC	Programmable Logic Controller
PMAC	Permanent Magnet Alternating Current Motor
PMSM	Permanent Magnet Synchronous Motor
POVC	Pilot Operated Check Valve
PPU	Power Processing Unit
PWM	Pulse Width Modulation
RMS	Root Mean Square

Acronym	Explanation
RPM	Revolution Per Minute
RV	Relief Valve
SCHC	Self Contained Hydraulic Cylinder
SVM	Space Vector Modulation
UDP	User Datagram Protocol
VDC	Voltage Direct Current
VPFM	Variable displacement Pump and Fixed Motor speed
VPVM	Variable displacement Pump and Variable Motor speed
VSC	Voltage Source Converter

Bibliography

[1] L. Kun L. Kai, L. Zhong and Y. Ping. "Thermal-hydraulic Modeling and Simulation of the Hydraulic System Based on the Electro-Hydrostatic Actuator" *J.Procedia Engineering 80*, vol.80, pp.272 – 281, 2014. Available: https://www.sciencedirect.com/science/article/pii/S1877705814011795 Accessed on: 03-04-2018.

[2] R. Alden. "C-141 AND C-130 POWER-BY-WIRE FLIGHT CONTROL SYSTEMS", 1991. Available: http://ieeexplore.ieee.org/stamp/stamp.jsp?tp=&arnumber=165802 Accessed on: 13-03-2018.

[3] M.A. El Sayed and S. Habibi. "A Combined Multiple Inner Loop Control Strategy for an Electro-Hydraulic Actuator" in symp *Centre for Power Transmission and Motion Control*, Univeristy of Bath, UK, 2012. Available: http://opus.bath.ac.uk/40760/1/2012_FPMC_proceedings.pdf Accessed on: 10-03-2018.

[4] M. Rygaard-Hansen and T.O. Andersen. *Hydraulic Components and Systems*. unpublished.

[5] H.C. Pedersen L. Schmidt, M. Groenkjaer and T.O. Andersen. "Position Control of an Over-Actuated Direct Hydraulic Cylinder Drive" *Elsevier, Control Engineering Practice*,Vol. 64, pp. 1-14, 2017.

[6] T.O.ANDERSEN H.C. PEDERSEN, L. SCHMIDT and M.H.BRASK. "Investigation of New Servo Drive Concept Utilizing Two Fixed Displacement Units" presented at *The 9tn JFPS Int.Symp.on Fluid Power*Matsue, Japan, 2014.

[7] N. Alle S.S. Hiremath S. Makaram K. Subramaniam and A. Talukdar. "Review on electro hydrostatic actuator for flight control" *International Journal of Fluid Power*, vol.17, no.2,pp.125-145,Apr 2016, 2016. Available: https://www.tandfonline.com/doi/pdf/10.1080/14399776.2016.1169743?needAccess=true Accessed on: 10-03-2018.

[8] A. Navathaa K. Bellada S. S. Hirematha and S. Karunanidhib. "Dynamic Analysis of Electro Hydrostatic Actuation System" presented in *1st Global Colloquium in Recent Advancement and Effectual Researches in Engineering, Science and Technology*, vol.25,pp.1289-1296, Apr 2016, 2016. Available: https://ac.els-cdn.com/S2212017316305771/1-s2.0-S2212017316305771-main.pdf?_tid=b12d3c42-94f6-49a0-a027-24eaab353db2&acdnat=1520878588_6163073dee13eb138dba11468adcd2d9 Accessed on: 12-03-2018.

[9] G. Bo S. Young-ling and P. Zhong-cai. "Research of the Servo Pump's Electrically Driven Variable Displacement Mechanism" presented at International Conference on Mechatronics & Automation Niagara Falls, Canada, 2005. Available: https://http://ieeexplore.ieee.org/stamp/stamp.jsp?tp=&arnumber=1626892 Accessed on: 12-03-2018.

[10] S. Karunanidhi. "Emerging Hydraulic Actuation Technologies for Aerospace Application," *Modeling, Identification and Control*, Research Centre Imarat, DRDO, Hyderabad - 500069, INDIA. Available: http://fpsindia.net/images/fpts/session1/DrKarunanidhi.pdf Accessed on: 07-04-2018.

[11] K.E. Rydberg. "Energy Efficient Hydraulics – System solutions for loss minimization" presented at *National Conference on Fluid Power*Linkøping, Sweden, 2015. Available: https://www.diva-portal.org/smash/get/diva2:916150/FULLTEXT01.pdf Accessed on: 03-04-2018.

[12] G. Altare and A. Vacca. "A design solution for efficient and compact electro-hydraulic actuators" *J.Procedia Engineering 106 (2015)* , vol.106,pp.8 – 16, Febr, 2015. Available: https://ac.els-cdn.com/S1877705815009285/1-s2.0-S1877705815009285-main.pdf?_tid=156fc366-2ed4-4d37-86e5-88041c373fa2&acdnat=1522770433_ed6f37a4c25c23c7278662eadb724f97 Accessed on: 03-04-2018.

[13] K. McCullough. "Design and Characterization of a Dual Electro-Hydrostatic Actuator" M.S.thesis, Dept. of Mech. Eng. McMaster Univ., Hamilton, Canada, 2011. Available: https://pdfs.semanticscholar.org/717b/7018303bfea7cf6f3d1197afc4a427a90b4b.pdf Accessed on: 03-04-2018.

[14] D. Hagen and D. Padovani. "Study of a Self-Contained Electro- Hydraulic Cylinder Drive " 2018. Accepted for publication.

[15] N.S. Nise. *Control Systems Engineering.* Wiley & Sons, 2011.

[16] M. Choux. *MAS107, Feedback Control Systems 1, Lecture Notes*, 2014.

[17] J. D. Zimmermann. "Toward optimal multi-actuator displacement controlled mobile hydraulic systems" Ph.D Thesis, Purdue Univ., 2012.

[18] E.BUSQUETS* and M.IVANTYSYNOVA. "THE WORLD'S FIRST DISPLACEMENT-CONTROLLED EXCAVATOR PROTOTYPE WITH PUMP SWITCHING – A STUDY OF THE ARCHITECTURE AND CONTROL" presented at *The 9tn JFPS Int.Symp.on Fluid Power*Matsue, Japan, 2014. Available: http://www.jfps.jp/Proceedings2014/proceedings/pdf/1D3-2.pdf Accessed on: 10-05-2018.

[19] N. Mohan. *Electric machines and drives: a first course.* Wiley & Sons, 2012.

[20] O. Wallmark L. Harnefors, M. Hinkkanen and A.G. Yepes. "Control of Voltage-Source Converters and Variable-Speed Drives". Unpublished.

[21] M.S. Merzoug and F. Naceri. "Comparison of Field-Oriented Control and Direct Torque Control for Permanent Magnet Synchronous Motor (PMSM)," *World Academy of Science, Engineering and Technology*,Vol. 45, pp. 299–304, 2008. Available: https://pdfs.semanticscholar.org/03ac/d707ef3e7473c02de97360f35834aab72b90.pdf Accessed on: 16-04-2018.

[22] J.L. Meriam and L.G. Kraige. *Engineering Mechanics, Dynamics.* Wiley & Sons, 2013.

[23] M. Rygaard-Hansen J.K. Sørensen and M.K. Ebbesen. "Numerical and Experimental Study of a Novel Concept for Hydraulically Controlled Negative Loads," *Modeling, Identification and Control*, Vol. 37, No. 4, , pp. 195–211, 2016.

[24] T.O.Andersen. "Feedback Control Systems and Properties of Matter" , Dept. of Energy. Tech. Aalborg Univ., 2017.

List of Figures

Appendix A

Appendix

A.1 User Manual

A.1.1 Start up procedure:

1. Power ON the PLC inside the control cabinet.
2. Power ON the PC and login with a password.
3. Start the PLC software "IndraWorks" and start a new project or open an existing program for control of the PLC.
4. The crane can be controlled manually by the joystick or by programmed motion profiles. Enable the desired working mode by turning on or off the boolean variables associated with the working mode function blocks. Chose the variable state by clicking in the window two columns to the right of the variable name an and press "Ctrl"+F7 to update the state.
5. Control blocks from Simulink can be converted to function blocks in IndraWorks by use of structured text.

A.1.2 Shut down procedure:

1. Before shut down, make sure the crane are completely lowered. If necessary, use the joy stick-mode for lowering.
2. Turn OFF the PLC and PC.

A.2 Data Sheet for Pump and Electric Motor

Technical data A10FZG size 3 to 63

Superordinate size		**NG**		**10**				**18**							**28**
Available intermediate sizes		**NG**		**3**	**6**	**8**	**10**	**12**	**14**	**16**	**18**	**21**	**22**	**23**	**25**
Displacement, geometric, per revolution		$V_{g\,max}$	cm^3	3	6	8.1	10.6	12	14	16	18	21	22	23	25
Rotational speed maximum[1]	at $V_{g\,max}$														
Suction speed operation as a pump[1]		n_{nom}	rpm	3600				3300				3000			
Max. speed decompression operation[2]		n_{nom}	rpm	3600				3300				3000			
Flow	at n_{nom} and $V_{g\,max}$	q_v	l/min	10.8	21.6	29	38.2	39.6	46.2	52.8	59.4	63	66	69	75
Power pump operation	at n_{nom}, $V_{g\,max}$ and Δp = 315 bar	P	kW	5.6	11.3	15.3	20	21	24.2	27.7	31.2	33	34	36.3	39
Torque	at $V_{g\,max}$ and Δp = 315 bar	T	Nm	15	30	40.5	53	60.2	70.2	80.2	90.3	105	110	116	125
	at $V_{g\,max}$ and Δp = 100 bar	T	Nm	5	9.5	12.7	16.8	19.1	22.3	25.5	28.7	33.4	35	36.6	40
Rotary stiffness of drive shaft	S	c	Nm/rad	9200				–				–			
	R	c	Nm/rad	–				14800				26300			
Moment of inertia for rotary group		J_{TW}	kgm^2	0.0006				0.0009				0.0017			
Maximum angular acceleration[2][3]		α	rad/s^2	14000				12600				11200			
Case volume		V	l	0.11				0.19				0.6			
Weight (approx.)		m	kg	9				10				15.5			

Determining the characteristics					
Flow	q_v	=	$\frac{V_g \times n \times \eta_v}{1000}$		[l/min]
Torque	T	=	$\frac{V_g \times \Delta p}{20 \times \pi \times \eta_{hm}}$		[Nm]
Power	P	=	$\frac{2 \pi \times T \times n}{60000}$	= $\frac{q_v \times \Delta p}{600 \times \eta_t}$	[kW]

Key

V_g Displacement per revolution [cm^3]
Δp Differential pressure [bar]
n Rotational speed [rpm]
η_v Volumetric efficiency
η_{hm} Hydraulic-mechanical efficiency
η_t Total efficiency ($\eta_t = \eta_v \times \eta_{hm}$)

Notice

- Theoretical values, without efficiency and tolerances; values rounded
- Operation above the maximum values or below the minimum values may result in a loss of function, a reduced service life or in the destruction of the axial piston unit. We recommend testing the loads by means of experiment or calculation / simulation and comparison with the permissible values.

1) The values are applicable:
– At absolute pressure $p_{abs} \geqq$ 1 bar on the low-pressure side (input)
– For the optimal viscosity range of ν_{opt} = 36 to 16 mm^2/s
– For hydraulic fluid based on mineral oils
2) Higher values on request
3) The limit value is only valid for a single pump, multiple pump version available on request. The load capacity of the connecting parts must be considered.

4.11.3 MSK071E - Technical Data

Designation	Symbol	Unit	MSK071E -0200-FN	MSK071E -0200-NN	MSK071E -0300-FN	MSK071E -0300-NN	MSK071E -0450-FN	MSK071E -0450-NN
Continuous torque at standstill 60 K	M_{0_60}	Nm	23.0					
Continuous current at standstill 60 K	$I_{0\_60(rms)}$	A	10.1		12.5		20.0	
Continuous torque at standstill 100 K	M_{0_100}	Nm	28.0					
Continuous current at standstill 100 K	$I_{0\_100(rms)}$	A	12.6		15.2		24.4	
Continuous torque at standstill. surface	M_{0_S}	Nm	---	34.5	---	34.5	---	34.5
Continuous current at standstill. surface	$I_{0\_S(rms)}$	A	---	15.2	---	18.8	---	30.0
Standstill continuous torque liquid	M_{0_L}	Nm	43.7	---	43.7	---	43.7	---
Continuous standstill current liquid	$I_{0\_L(rms)}$	A	19.0	---	24.9	---	38.0	---
Maximum torque	M_{max}	Nm	84.0					
Maximum current	$I_{max(rms)}$	A	45.5		56.3		90.1	
Torque constant at 20 °C	K_{M_N}	Nm/A	2.51		2.05		1.29	
Voltage constant at 20 °C[1)]	K_{EMK_1000}	V/1,000 min-1	154.6		126.4		82.7	
Winding resistance at 20 °C	R_{12}	Ohm	1.16		0.79		0.32	
Winding inductivity	L_{12}	mH	9.15		5.9		2.6	
Discharge capacity of the component	C_{dis}	nF	8.9		9.3		9.5	
Number of pole pairs	o	-	4					
Moment of inertia of the rotor	J_{rot}	kg*m²	0.00290					
Thermal time constant	T_{th_nom}	min	8.0	55.0	8.0	55.0	8.0	55.0
Maximum velocity	n_{max}	min-1	3400		4200		6000	
Sound pressure level	L_P	dB[A]	< 75					
Weight [2)]	m	kg	23.5 (25.1)					
Surrounding air temperature during operation	T_{amb}	°C	0 ... 40					
Protection class acc. to EN 60034-5	-	-	IP65					
Thermal class acc. to EN 60034-1	T.CL.	-	155					
Data liquid cooling								
Power loss to be dissipated	P_V	kW	1.00	---	1.00	---	1.00	---
Coolant inlet temperature	T_{in}	°C	10 ... 40	---	10 ... 40	---	10 ... 40	---
Allowed coolant temperature rise at P_V	ΔT_{max}	K	10	---	10	---	10	---
Necessary coolant flow at P_V	Q_{min}	l/min	1.5	---	1.5	---	1.5	---
Pressure loss at Q_{min}	Δp	bar	0.5	---	0.5	---	0.5	---
Maximum allowed inlet pressure	p_{max}	bar	6.0	---	6.0	---	6.0	---
Volume of coolant duct	V_{cool}	u	0.06	---	0.06	---	0.06	---
Material coolant duct			Aluminum pressure casting					
Latest amendment: 2014-01-21								

1) Manufacturing tolerance ±5 %
2) (...) Motors with holding brakes 1, 2, ...

Tab. 4-20: MSK - Technical data

Technical Data

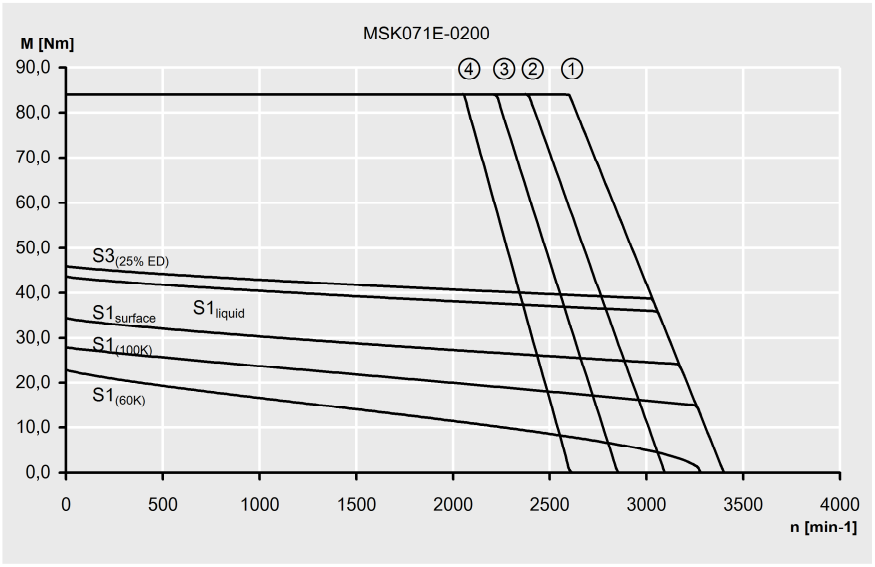

Fig. 4-39: Characteristic curves of an MSK071E-0200 motor

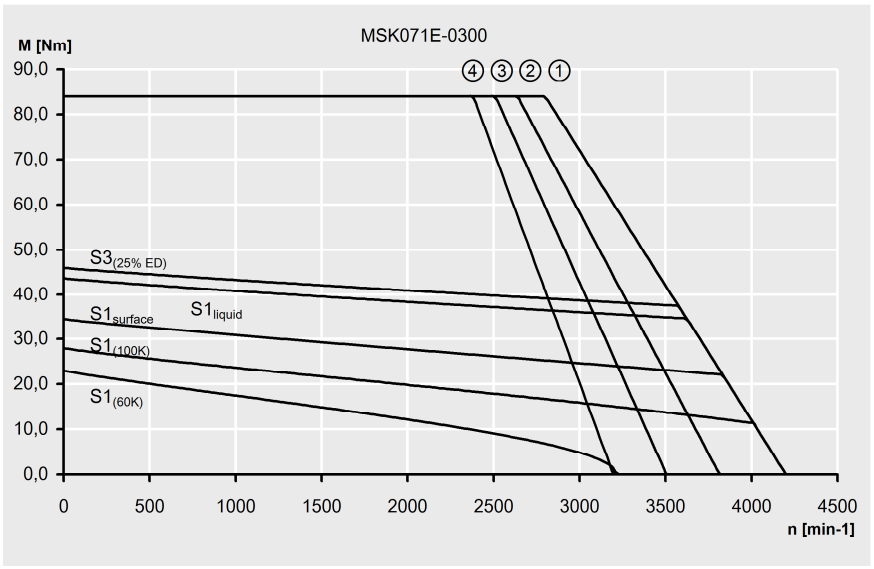

Fig. 4-40: Characteristic curves of an MSK071E-0300 motor